UNIVERSITÀ DEGLI STUDI DI PADOVA

UNIVERSITA' DEGLI STUDI DI PADOVA

Dipartimento di Ingegneria Industriale DII

Corso di Laurea in Ingegneria dell'Energia Elettrica

Application of Modular Multilevel Converter technology to HV power supplies of Neutral Beam Injectors

Relatore: Prof. Paolo Bettini

Correlatore: Ing. Alberto Ferro

Daniele Ratti

Matricola 1177855

Anno Accademico 2018/2019

Ai miei genitori e mio fratello..

E a Te, a cui tutto devo..

1 Contents

Abstract

The Neutral Beam Injectors (NBIs) foreseen for the largest thermonuclear fusion reactors based on magnetic confinement operate with acceleration voltages of about some hundreds of kV. The related power supply system (Acceleration Grid Power Supply, AGPS) must provide these voltages, often subdivided into intermediate steps, and currents of few tens of Amperes. In addition, it must limit the energy transferred during the frequent electrical breakdowns between the acceleration grids and then, once the isolation is restored, to restart in some milliseconds.

The design of AGPS evolved from early NB systems based on thyristor converters, with comparatively slow response, acceleration voltages up to 160 kV and tetrode switches placed in series to protect against the grid breakdown. Breakdowns correspond to load short-circuit during full power operation and, rather than exceptional faults, are expected common events, complicating the design. The higher acceleration voltages requested in larger tokamaks make very difficult the DC current interruption in case of grid breakdown. Currently, new schemes are adopted, based on modular configurations that comprise solid state inverters feeding step-up transformers connected to high-voltage diode rectifiers; in these schemes the protection against grid breakdowns relies on fast switch-off of the solid-state inverters.

The MITICA experiment is the full-scale prototype of the ITER NBI, operated in Padua by Consorzio RFX. The ITER NBI is designed to deliver up to 16.5 MW of additional heating to the plasma, accelerating negative ions up to -1 MV with a beam current as high as 40 A (deuterium operation) and 46 A (hydrogen operation), for as long as 3600 s. The beam is created and accelerated by means of two main power supplies: the Ion Source and Extraction Power Supplies (ISEPS), devoted to supply the ion source components and the extraction grid, and the AGPS, providing power to the acceleration grids. The ion source is based on 8 radio-frequency-driven antennae and the 1 MeV accelerator, named MAMuG (Multi Aperture Multi Grid), is composed of five acceleration gaps, of -200 kV each.

The main requirements of the MITICA NBI experiment are high voltage acceleration (1 MV) to deliver the required power to the plasma, capability of handling repetitive grid breakdowns (BD), and sufficiently high dynamic response and precision. These requirements addressed the design of the ITER NBI AGPS towards a solution which is near the limit of modern available technologies in the area of high-power static conversion systems and of the very high DC voltage equipment; indeed, the current AGPS design present some critical points that lead at exploring and evaluating alternative solutions which could mitigate them.

The thesis presents the studies, carried out by the author in collaboration with the research group of Consorzio RFX, aiming at evaluating the possible utilization of Modular Multilevel Converters (MMC) for future NBI AGPS. The interest in this topology comes from its intrinsic properties of modularity, efficiency and controllability. In section 1, a brief introduction to the energy problem and the principles of thermonuclear fusion are given. In section 2 the tokamak magnetic configuration is presented, which is the most promising for a fusion reactor. Section 3 describes the basic operating principles of a NBI for plasma heating and current-drive and its main components as well. In section 4 the current AGPS design for the ITER NBI is presented, trying to outline the criticalities and how to possible overcome them; the main operating requirements, regarding steady state and dynamic performances, are discussed. In section 5 the Modular Multilevel Converter technology is presented, with the following order. First an introduction on the MMC topology is given, considering its basic working principles and the main submodule configurations and strings. Then, the main circuit relations are addressed, comprising dynamic and steady state conditions; after that the DC short circuit handling strategies are described. Finally, the control logic of a MMC is studied, thanks to the introduction of an averaged model of the converter; the modulation and voltage balancing techniques are analysed too. In section 6 it is addressed a MMC preliminary design intended for NBI AGPS application. In section 7 it is presented a scaled numerical model of the MMC-based for AGPS previously outlined and the

steady-state and dynamic performances are evaluated, trying to compare the results with the actual AGPS system.

Sommario

Gli iniettori di fasci neutri (Neutral Beam Injectors, NBI) previsti per i più grandi esperimenti di fusione termonucleare basata su confinamento magnetico operano con tensioni di accelerazione di qualche centinaio di kV. I relativi sistemi di alimentazione (Acceleration Grid Power Supply, AGPS) devono fornire queste tensioni, spesso suddivise in step intermedi, e correnti di qualche decina di Ampere. In aggiunta, essi devono limitare l'energia trasferita durante le frequenti scariche elettriche fra le griglie di accelerazione a poi, una volta che l'isolamento è ripristinato, ripartire in qualche millisecondo.

Il progetto di questi sistemi di alimentazione (AGPS) si è evoluto a partire da primi sistemi basati su convertitori a tiristori, con tempi di risposta relativamente lenti, tensioni di accelerazione fino a 160 kV e tetrodi posti in serie per la protezione da scariche elettriche tra le griglie (breakdowns). Queste scariche corrispondono a cortocircuiti durante il funzionamento a piena potenza e, piuttosto che eventi eccezionali, sono da considerarsi eventi comuni, complicando il progetto di queste alimentazioni. Le maggiori tensioni di accelerazione richieste in tokamak più grandi, rendono molto difficile l'interruzione della corrente DC in caso di breakdown. Al momento sono utilizzati nuovi schemi, basati su configurazioni modulari comprendenti inverter allo stato solido che alimentano trasformatori elevatori connessi a raddrizzatori a diodi in alta tensione; in questi schemi la protezione contro le scariche tra le griglie fa affidamento al veloce spegnimento degli inverter allo stato solido.

L'esperimento MITICA è il prototipo a piena scala dell'iniettore di neutri di ITER ed è in operazione a Padova, al Consorzio RFX. L'iniettore di neutri di ITER è progettato per fornire fino a 16.5 MW di potenza di riscaldamento addizionale al plasma, accelerando ioni negativi fino a -1 MV con una corrente del fascio pari a 40 A (nel funzionamento con deuterio) a 46 A (nel funzionamento con idrogeno), per un tempo di 3600 s. Il fascio è creato e accelerato per mezza di due principali sistemi di alimentazione: gli alimentatori della sorgente ionica e della griglia di accelerazione (ISEPS) e quelli che forniscono potenza alle griglie di accelerazione (AGPS). La sorgente ionica è composta da 8 antenne azionate a frequenza radio mentre l'acceleratore ad 1 MeV, è formato da cinque stadi di accelerazione, ciascuno di -200 kV. La struttura dell'acceleratore, inoltre, comprende diverse griglie ciascuna delle quali con diverse aperture (configurazione MAMuG).

I principali requisiti dell'iniettore di neutri MITICA comprendono un'elevata tensione di accelerazione (1 MV) per fornire la potenza richiesta al plasma, la capacità di gestire breakdown ripetitivi e una sufficientemente alta precisione e risposta dinamica. Questi requisiti conducono il progetto dei sistemi di alimentazione per le griglie di accelerazione (AGPS) dell'iniettore di neutri di ITER verso una soluzione che è vicina agli attuali limiti tecnologici nell'area della conversione statica di elevata potenza e dell'altissima tensione continua per dispositivi elettrici. Per questi motivi, l'attuale sistema di alimentazione (AGPS) presenta alcuni aspetti critici che portano ad esplorare e valutare soluzioni alternative che potrebbero mitigarli.

La tesi presenta gli studi, condotti dall'autore in collaborazione con il gruppo di ricerca del Consorzio RFX, volti a valutare l'utilizzo di Convertitori Modulari Multilivello (Modular Multilevel Converters, MMCs) per l'alimentazione delle griglie di accelerazione di futuri iniettori di neutri. L'interesse per questa topologia deriva dalle sue intrinseche proprietà di modularità, efficienza e controllabilità. Nella Sezione 1 viene data una breve introduzione al problema energetico e ai principi della fusione termonucleare. Nella Sezione 2 la configurazione magnetica tokamak è presentata, essendo la più promettente per un reattore da fusione. La Sezione 3 descrive i principi di base di funzionamento di un iniettore di neutri per il riscaldamento e l'induzione della corrente di plasma. Nella Sezione 4 l'attuale sistema di alimentazione (AGPS) per l'iniettore di ITER è presentato, provando cercando di delineare le criticità e possibilmente come superarle; i principali requisiti operativi, riguardanti prestazioni a regime stazionario e dinamico, sono discussi. Nella Sezione 5 la tecnologia MMC è presentata, con il seguente ordine. Dapprima si introduce la topologia MMC, considerando i principi base di funzionamento e le principali configurazioni di sub-moduli e stringhe. Poi, le principali

relazioni circuitali sono analizzate, comprendendo condizioni dinamiche e stazionarie; dopo di ciò le strategie di gestione dei cortocircuiti lato DC sono descritte. Alla fine, la logica di controllo di un convertitore MMC è studiata, grazie all'introduzione di un modello medio del convertitore; anche le strategie di modulazione e di bilanciamento della tensione sono analizzate. Nella Sezione 6 viene eseguito un progetto preliminare di convertitore MMC per i sistemi di alimentazione delle griglie di accelerazione (AGPS). Nella Sezione 7 è presentato un modello numerico in scala rispetto al convertitore MMC per applicazione AGPS precedentemente progettato e le prestazioni a regime stazionario e dinamiche sono valutate, provando a confrontare i risultati con l'attuale sistema AGPS.

Acronyms

HNBI Heating Neutral Beam Injector

PS Power Supply

AGPS Acceleration Grid Power Supply

ISEPS Ion Source and Extraction grid Power Supply

NBI Neutral Beam Injector

MMC Modular Multilevel Converter

HVDC High Voltage Direct Current

BD Breakdown

TL Transmission Line

F4E Fusion for Energy (European domestic agency)

JADA Japanese Domestic Agency

SM SubModule

HB Half Bridge

FB Full Bridge

1. Introduction to nuclear fusion

1.1 Fusion as a source of energy

The quest for fusion power is driven by the need for large scale, sustainable and predictable low-carbon energy generation, in a future society where the global electricity demand is increasing. The world's population is expected to rise from seven to nine billion by 2040; this together with better living conditions in the emerging countries drives the foreseen global electricity consumption up by 28% from 2015 to 2040 as can be seen in Fig. 1.1 [1]. The OECD countries are members of the Organization for Economic Cooperation and Development and account mainly for stabilized industrial regions, non-OECD countries comprise big growing economics like India and China. Most of the increase in energy demand is expected to come from non-OECD countries, where strong economic growth, increased access to marketed energy, and quickly growing populations lead to rising demand for energy.

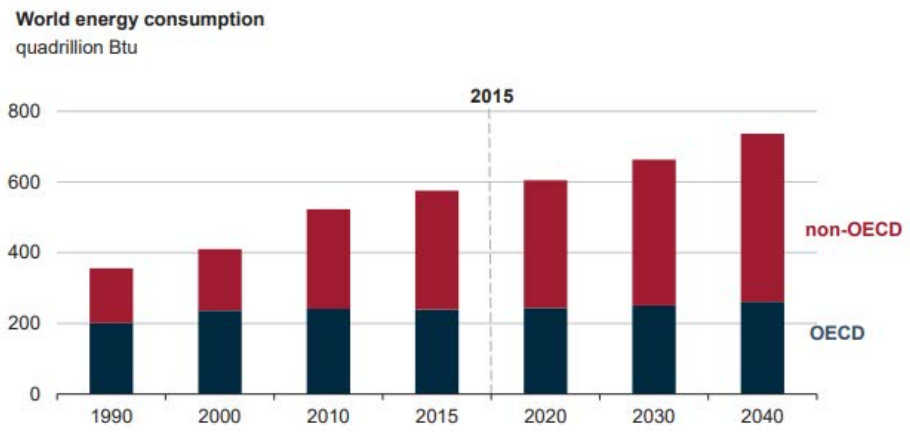

Fig. 1.1 World energy consumption future trend [1]

Meeting this demand with technologies currently available would require fossil fuels remaining a primary source of electricity generation. Actually, the intensive use of fossil fuels to cover the base-load demand is not a viable solution because of its negative impacts on the environment and human health. Moreover, the diminishing fuel reservoirs imply that reliance on coal, oil and gas for the energy supply will be gradually limited in the future.

The development of renewables energies of the last decades, such as solar and wind power, have greatly contributed to the road towards a more sustainable and green energy generation but these sources have several drawbacks, inherently due to their nature. The renewables sources are intermittent, making them reliant on environmental conditions, and show low-density power production, which means wider occupied area for the same rated power plant. For these reasons the renewables are not suited to fully replace the fossil fuels as the base-load supply and other non-varying and high-density energy sources are needed.

The outlined need of reliable power supply and the substitution of fossil-fuel power plants in favour to low-carbon energy scenarios have refocused attention on the nuclear energy exploitation. An energy strategy based on fission power plants for baseload supply meets the large-scale power generation requirement but has to cope with considerable issues, like the safe handling of the unavoidable radioactive waste and the social acceptation of the risks correlated with these nuclear plants.

Fusion energy could offer a secure, long-term source of supply with remarkable advantages. These comprise: no greenhouse gases emission, no long-lived radioactive waste (all waste recyclable within 100 years), inherently safe working conditions and possible unlimited fuel supplies. Despite all these promising benefits

the feasibility of fusion is still to be demonstrated, and the path toward it comprises several targets to be fulfilled.

Briefly, the feasibility and suitability of nuclear fusion as energy source involves the following areas:

Scientific feasibility:

Confining plasma at thermonuclear temperatures for enough time and that a sufficiently high energy production can be obtained to enable net power to be produced by the fusion reactions. The practical threshold of scientific feasibility is a gain factor Q>10 where:

$$Q = \frac{P_{fusion}}{P_{input}} \quad (1.1)$$

The existing experiments obtained a gain factor of about 1, meaning that the system is producing the same amount of thermal power of the input heating power required for working.

Engineering feasibility:

The development of magnetic fusion as a source of energy requires the development of two types of engineering technology: plasma support technologies and nuclear technologies. The first one comprise, among the others, plasma heating systems and power supply systems which are of major interest in this thesis and will be addressed in Section 2 and 3.

Practical suitability:

The realization of a fusion power plant operating reliably in an electrical grid require to achieve a continuous or quasi-continuous operational mode; at present the conventional tokamak concept is inherently pulsed, as explained in Section 2, and the implementation of non-inductive scenarios are required in the future.

Economic Feasibility and Fuel Resources

Today the estimated price of fusion electricity is more costly than other sources but considering the prevention of carbon emission the cost can be rescaled in favour of fusion electricity [2]. The fusion fuel reservoir (lithium) is estimated to last much more than other fossil and fission fuels.

To progress in the road towards fusion energy, the research community has scheduled gradual steps, which mainly involve the ITER tokamak realization. On ITER project are working together 25 nations and its main goal is to produce large-scale fusion power, that is 500 MW for 400 s. The ITER's First Plasma is scheduled for December 2025. After that, in the second part of this century a DEMO (demonstration) power plant will be put in operation to test the grid integration of a fusion plant delivering hundreds of MW for several hours. The main characteristics of ITER and DEMO tokamaks will be described in Section 2.

1.2 Nuclear Reactions

Nuclear reactions involve only the nuclei of the atoms by the interaction of nucleons due to strong nuclear attraction forces. These reactions do not conserve the mass, and according to the famous Einstein's relation $E = mc^2$ a certain amount of energy is released. Indeed, in a primary chemical element (mass number A, N neutrons and Z protons) the total mass of the isolated individual nucleons exceeds the actual mass (m_a).

$$N\, m_n + Z m_p > m_a \quad (1.2)$$

This difference in mass is transformed into Binding Energy (Eb) which is responsible of holding together the nucleus:

$$E_B = \left(N\, m_n + Z m_p - m_a\right)c^2 \qquad (1.3)$$

A convenient quantity is Eb/A which is a measure of the average energy binding for each nucleon of the nucleus. Calculating this parameter for all the elements results in the curve of Fig. 1.2, where the most stables elements, such as Fe and Br, are on the top of it. All the nuclear reactions that converges on this stable region are exoenergetic, viceversa moving from this region from lighter or heavier nuclei implies an energy adsorption. It follows that combing light elements together (nuclear fusion) or splitting heavy ones apart imply a release of energy (nuclear fission).

The amount of energy released in nuclear reactions is much higher than in ordinary chemical reactions, for instance between the fission of uranium and the burning of gasoline there is a factor 10^6 MJ/kg of difference. It can be easily shown that starting from the same amount of reagents the fusion reactions release a major amount of energy than fission ones. Besides this energetic advantage the fusion of hydrogen isotopes produces non-radioactive waste, with great benefit in the handling of them and the reactions occur only at extreme conditions (comparable to those existing in the core of the stars), failing which the process ends safely; this last represents a huge advantage for a nuclear plant.

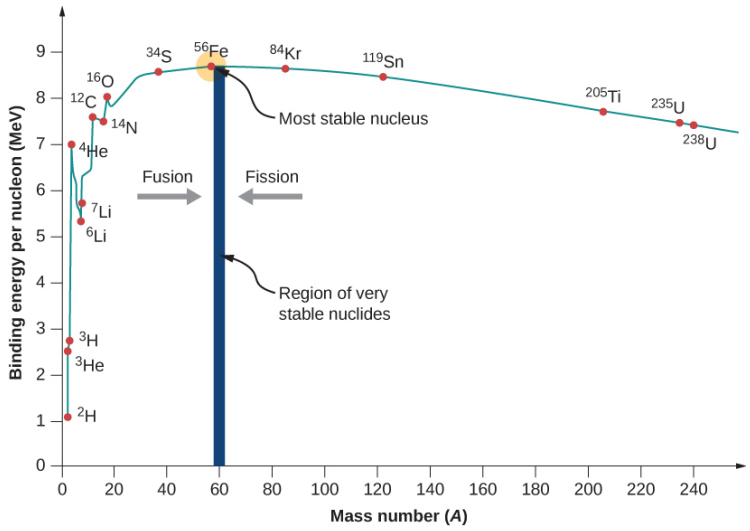

Fig. 1.2 Binding energy per nucleon.

Among the possible fusion reactions of hydrogen isotopes the most promising one is the D-T (deuterium-tritium) reaction, which is the central focus of worldwide research:

$$D_1^2 + T_2^3 \rightarrow He_2^4 + n + 17.6\, MeV \qquad (1.4)$$

because it is the easiest to initiate (which means that a lower amount of energy must be provided for the reaction to take place) with respect to the D-D or D-He reactions. In order to have continuous operation there must be a continuous supply of tritium; unfortunately there is no natural tritium on earth (it is as radioactive isotope of H with half-life of about 12 years) being this one the main drawback of D-T reaction. The investigated solution is to breed tritium in the blanket surrounding the region of D-T fusion reactions, exploiting the high energy neutrons escaping from the plasma which react with the lithium present in the blanket; these interactions give rise to T and alpha particles:

$$Li_3^6 + n \rightarrow \alpha + T + 4.8\, MeV \qquad (1.5)$$

$$Li_3^7 + n \rightarrow \alpha + T + n - 2.5\ MeV \qquad (1.6)$$

Even though there is much larger fraction of Li_3^7 the reaction involving Li_3^6 is much easier to initiate and as a result it dominates in the breeding of tritium.

1.3 Principles of Fusion Reactions

For two light atoms to undergo a nuclear reaction, their nuclei must be very close to each other, typically about the nuclear diameter (approximately 10^{-15} m). At this point starts to prevail the strong nuclear attractive force on the coulomb repulsion force: once the so-called Coulomb barrier is exceeded the attractive forces become dominant and fusion can occur. In Fig. 1.3 is shown the behaviour of potential energy between two nuclei over the distance among them. According to classical theory the Coulomb barrier can be expressed as $U_0 = \frac{Z_1 Z_2 e^2}{4\pi\varepsilon r}$ and for a D-T reaction it results $U_0 \approx 288$ keV.

Note that hydrogen isotopes heated at these temperatures (288 keV correspond to $3{,}36 * 10^9$ K) can only exist in the form of plasma, which constitutes the fourth state of matter. The plasma is a ionized gas where the electrons are separated from nuclei, thus there is a charge separation even if the gas is globally neutral. We recall the two main parameters characterizing a thermonuclear plasma:

- Density (n): can vary from 10^6 to 10^{34} m^{-3}
- Temperature (T): can vary from 0.1 to 10^6 K

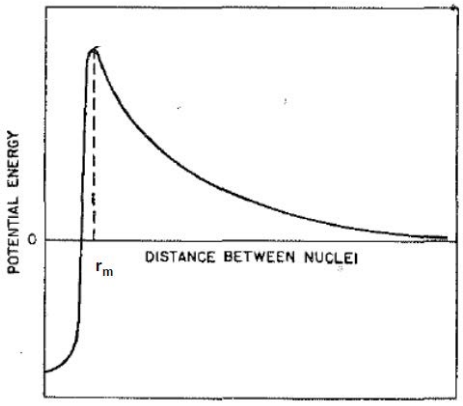

Fig. 1.3 Potential energy and coulomb barrier

It seems that only particles which are heated up to a temperature of 288 keV or higher can undergo fusion reactions according to classical theory. This model is too simplified and it does not take into account three other important phenomena influencing the probability of fusion reactions:

- Cross Section
  It represents in some quantitative form the probability that a pair of particles undergo a nuclear reaction. Graphically it can be seen as the projection of the spherical nuclear attractive field on the plane perpendicular to the moving particles, as shown in Fig. 1.2; if the moving particles passes through σ then the attractive field is sufficient strong that a fusion reaction takes place, otherwise not.
- Tunnel Effect
  Even below the Coulomb energy nuclear reactions can take place under certain conditions of relative velocity between the two colliding nuclei.
- Finite Probability of Interaction
  It seems that the higher the temperature of the plasma is, the higher is the probability of fusion reactions. From quantum mechanics it is known that if the relative velocity of the particles is very

large, the time available for an interaction is very short, thus the probability of a fusion collision starts to decrease.

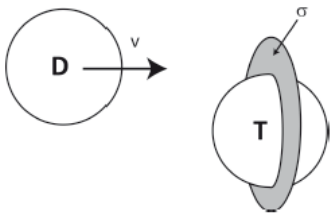

Fig. 1.4 Cross section representation

Considering now the integration of the cross-section area on the overall range of velocity, each velocity being expressed by a Maxwell distribution function, we obtain the effective fusion reaction rate, expressed in a compact form as:

$$R_{12} = < \sigma\, v > n_1 n_2 \qquad (1.7)$$

being *v* the relative velocity, n_1 and n_2 the ion density of the two species. It can be seen from Fig. 1.5 that R_{12} is maximized for a temperature of T≈70 keV for a D-T reaction, whereas D-D and D-T reaction rates are maximized at higher temperature and with lower probabilities as well. This explains why the fusion research experimentation is focused on the D-T reaction. Note that 70 keV correspond to a temperature of about $8.16*10^8$ K, which is higher than in the core of the sun.

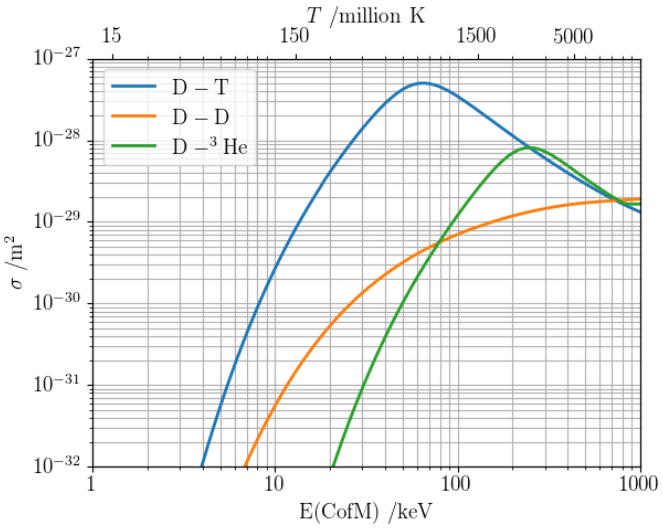

Fig. 1.5 Values of < σv> for D-T, D-D and D-He₃

1.4 Plasma confinement

In the current concept of fusion power plant, deuterium and tritium undergo fusion reactions reacting as in at a temperature in the order of 20 keV. At this temperature D and T exist in the form of plasma, which is a mixture of charged particles (electrons and ions) with great electrical conductivity properties. To maintain a temperature as high as 20 keV it is both necessary a system of additional heating and a secure confinement system of the plasma. The first is required to inject power into the plasma region, the latter to limit power dissipations with the external environment, and of course to preserve the containment structure from serious damage as well as guarantee a continuative operation. The two main research programs regarding plasma confinement are inertial and magnetic confinement.

In the inertial confinement method, the fusion reactions are initiated by heating and compressing a fuel target, typically a micro-sphere (pellet) containing the D-T mixture. The pellet is heated up at temperature of 10^8 K by an external power source, constituted by either high energy laser light or beam particles (electrons or ions). Heated and compressed, the external layer explodes outward producing a compressing counter-force on the D-T fuel, which propagate by waves that add up on the centre. Here the D-T particles reach temperature and density as high as to ignite fusion reactions. Then the energy released by these last ones ignite the remaining of the fuel. Once the initial compression force is extinguished, the micro-sphere is free to expand due to high internal pressure and then cools down, stopping in short time the nuclear reactions. The inertial confinement reactor is therefore inherently pulsed, and the main issue is related to the substitution of the pellet in short time, to repeat the cycle sometimes per second.

The magnetic confinement approach derives from the electrical property of plasma itself, which has great electrical conductivity due to presence of free charges and low density number and is therefore subjected to the Lorentz Force.

The first and natural idea of magnetic plasma confinement is to produce a uniform and straightforward magnetic field (B), like that inside an ideal solenoid. The particles describe a gyro motion along the B-lines which is the overlapping of a longitudinal and circular motion, respectively parallel to the B-lines and perpendicular to them. The motion, depicted in Fig. 1.6, is described by the Larmor radius (r_L) and the gyrotron pulsation (ω).

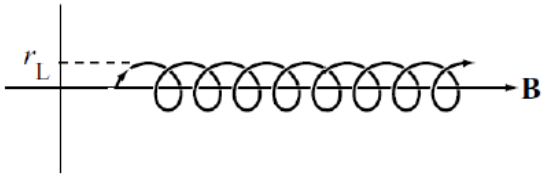

Fig. 1.6 Gyro motion

$$r_L = \frac{mV_\perp}{qB} \quad \omega = \frac{qB}{m} \text{ (1.8)}$$

Since r_L is in the order of millimetres for ions and micrometres for electrons the motion is well confined perpendicularly to the magnetic field, but it is not confined along the B-lines; it is therefore sufficient to close the magnetic lines to obtain the overall confinement and the simplest magnetic geometry to do is toroidal.

Unfortunately, if there is a component of electric field (E) perpendicular to B, the confinement is loss along the direction perpendicular to both the fields. The resulting motion can be seen as the overlapping of the previous gyro motion with a drift motion, which inevitably bring the charged particles out of the confinement zone, as can be seen in Fig. 1.7. Another drift arises from the presence of ∇B (gradient of B field) in the considered spatial region. As derived in [3] the drift velocity can be expressed as following, where F is the coulomb force and ∇ the spatial gradient:

$$\boldsymbol{V} = \frac{1}{q}\frac{\boldsymbol{F}\times\boldsymbol{B}}{|\boldsymbol{B}|^2} + \frac{1}{2}\frac{v_\perp^2}{w}\frac{\boldsymbol{B}\times\nabla\boldsymbol{B}}{|\boldsymbol{B}|^2} \quad (1.9)$$

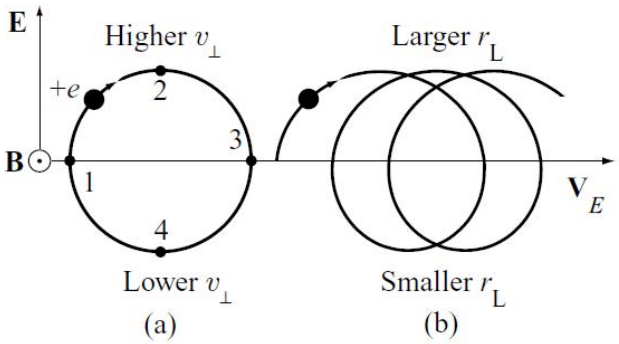

Fig. 1.7 a) only gyromotion (no electric field) b) gyromotion and drift

The last step to obtain a magnetic configuration able to resolve these drift motions is adding poloidal magnetic lines to the toroidal ones, generating the known *tokamak* configuration.

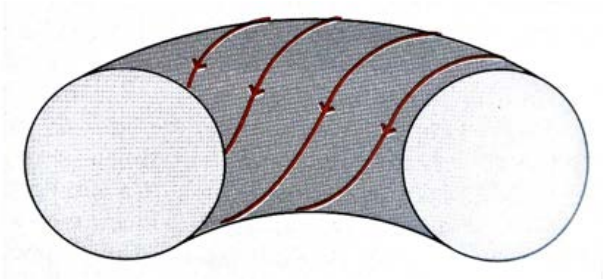

Fig. 1.8 Schematic view of tokamak magnetic configuration (in red the B-lines)

1.5 The fusion power plant

Within a fusion reactor the neutrons produced by the nuclear reactions are collected in the blanket, which covers the internal surface of the vacuum vessel, constituting the *first-wall* exposed to the thermonuclear plasma. The blanket is thus a very delicate part of a fusion plant and must be carefully designed in order to preserve its main function of heat removal, plasma physical containment and neutron shielding. To accomplish these requirements, it must: be able to quickly remove heat (high thermal conductivity) without increasing too much its temperature (high thermal capacity) and fusing (high fusion temperature); have good electro-mechanical performances; avoid embrittlement due to intense neutronic load and in the mean time limit the plasma-wall interaction. The thermal heat deposited by high-energy neutrons to the blanket is then transferred to a proper fluid, which undergoes a thermodynamic cycle, finally producing electricity as in conventional electric power plant. In a D-T based fusion power plant the blanket must contain Lithium (in liquid or solid form) in order to auto-produce, in loco, the tritium necessary to sustain the reactions, as described by eq. 1.4. A blanket containing lithium is called “breeding blanket” and it avoids any external tritium supply, becoming Lithium and Deuterium the actual nuclear fuels. The only exhaust is Helium which is a non-radioactive, well manageable and safe element. A schematic view of a fusion power plant with breeding blanket is represented in Fig. 1.9.

In the magnetic confinement fusion concept, the helium nuclei produced by the reactions are electrically charged and could in principle remain confined by the magnetic lines, transferring their energy to D and T and thus contribute in heating the plasma (alpha-power).

The *first-wall* also comprises the so-called divertor, a mechanical structure together with a pumping system, which has the function of removing the helium ashes together with other impurities exiting from the

confinement zone. A plasma magnetic configuration which bring the lost particles into the divertor is called *diverted*. Similar severe requirements as those described for the blanket are involved in the divertor design.

As previously outlined the operation of a fusion power plant is inherently safe since fusion reactions occur only under precise conditions and any alteration of them causes the plasma to cool down within some seconds and the reactions stop. Even if a loss of control would occur the power from nuclear reactions becomes zero and there is no way for the reaction to self-sustain. This one is a big advantage with respect to the conventional fission plants where a loss of control would in principle imply the fission of all nuclear fuel, which imply an enormous amount of energy releasing that causes the fusion of the core.

Moreover, the fusion fuels are available, if a breeding blanket is foreseen, safe and requested in little quantities compared to that of tradition fossil fuels. Finally, no pollution or greenhouse gases are emitted in the atmosphere by fusion plants; the major output-product is helium, an inert and non-toxic gas.

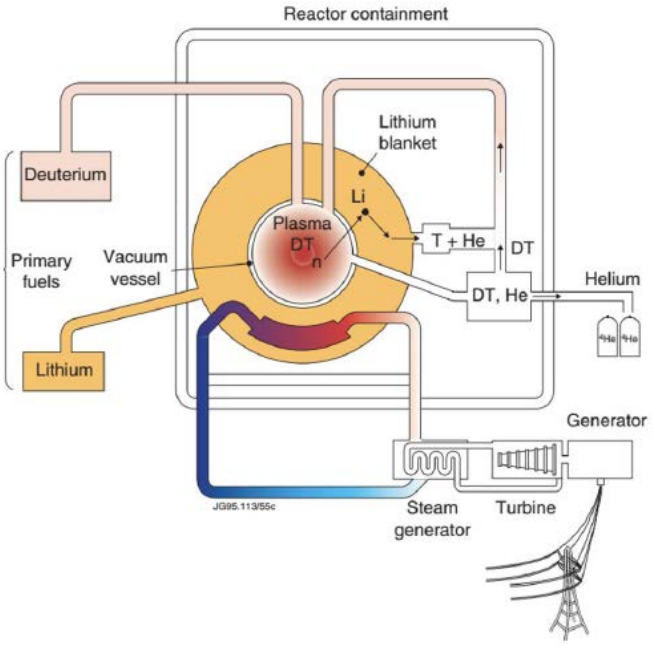

Fig. 1.9 Scheme of principle of a fusion power plant

2 The tokamak

2.1 Magnetic circuits

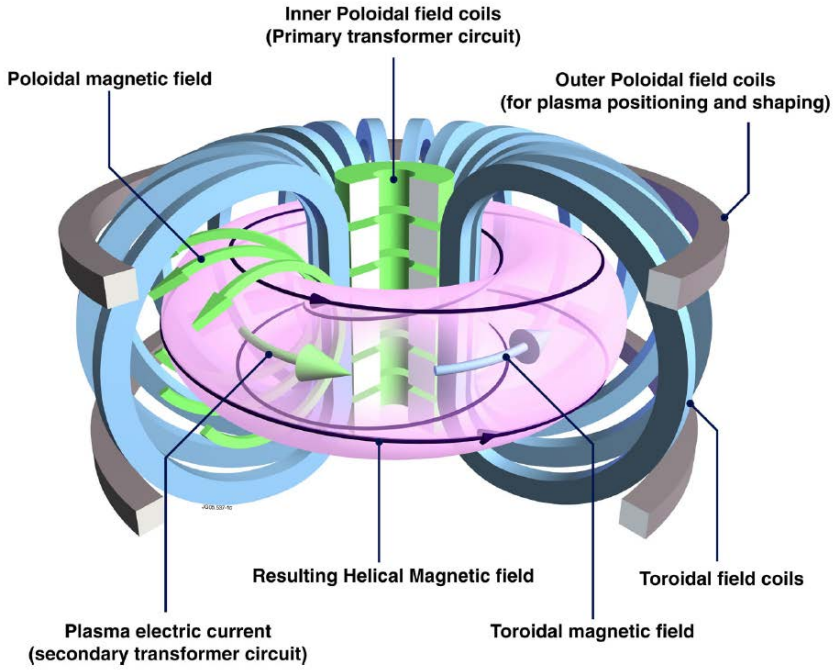

Fig. 2.1. Schematic magnetic configuration of a tokamak.

The tokamak magnetic configuration comprise toroidal and poloidal magnetic force lines, as shown in Fig. 2.1., which result in helical magnetic field lines.

Mainly three set of coils are required to produce this magnetic configuration and keep the plasma in equilibrium. The toroidal field coils produce the toroidal field lines which confine plasma particles along the toroidal direction; the central solenoid (inner poloidal field coils) produce the poloidal magnetic flux derivative over time which induce the gas breakdown and the plasma current; the outer poloidal field coils produce the vertical field required to counteract the outward plasma ring expansion.

The plasma current, induced by the central solenoid, generates circular and closed poloidal field lines which adds to the toroidal field lines; the superposition of the fields result in the tokamak magnetic configuration. Since plasma current is sustained by the flux swing of the central solenoid the plasma-pulse duration depends on the poloidal magnetic flux available: after a full swing no more current can be magnetically induced in the plasma and thus it starts to decay due to ohmic losses. The plasma pulse duration can be extended by Heating and Current Drive (H&CD) systems, which are fundamental also to maintain plasma at high temperature. Moreover, the plasma current, which is in order of MA (mega-ampere) provides the Ohmic heating of the plasma; unfortunately, plasma resistivity decrease with temperature, making less-effective the plasma self-heating. The ohmic effect, together with the alpha power, are not sufficient to reach fusion relevant temperatures, therefore external additional H&CD systems are needed.

2.2 Heating and Current Drive (H&CD) systems

A zero-dimensional power balance for a fusion reactor can be written as:

$$P_{aux} + P_{\alpha} + P_{ohm} = P_{loss} \tag{2.1}$$

Where P_{aux} represent the external heating sources, P_{α} the alpha power (about 1/5 of total fusion power), P_{ohm} the ohmic heating due to plasma resistivity and P_{loss} the power lost (for transport, bremsstrahlung, radiation etc.). In the present experiments P_{α} is near 0, since almost no fusion reactions occur; in future reactors the goal is ignition i.e. the plasma self-sustainment ($P_{aux} \cong 0$) thanks to high P_{α} contribution. The ion temperature must be about ≈10÷14 keV for ignition to take place and alpha power becomes dominant at T>5÷7 keV. This level of temperature is unreachable with only ohmich heating, therefore additional heating systems are required also in future fusion reactors.

Currently two additional heating systems are exploited: coupling of resonant radio-frequency (RF) electromagnetic (EM) waves and injection of high energy neutral particles (Neutral Beam Injection). These methods provide several MW of additional heating to the plasma and can be also used to sustain plasma in other ways, like for plasma current driving (CD), temperature and current profile shaping, plasma control and diagnostics.

EM waves couple with plasma by resonance phenomena at specific frequencies, depending on the plasma species mass and charge, see eq. 1.8. Therefore, for ions and electrons different systems are used: Ion Cyclotron Resonance Heating (ICRH) in the range of 30÷50 MHz and Electron Cyclotron Resonance Heating (ECRH) in the range of 100÷200 GHz. An intermedium frequency range, of few GHz, is used for Lower Hybrid Current Drive, which is a very efficient tool for CD. ITER baseline design foresees the use of ICRH and ECRH, both delivering 20 MW of power.

NBI system consists in injecting high energy neutral atoms, which can penetrate through the confining magnetic field, into the plasma. Outside of the tokamak, the Deuterium (or Hydrogen) is ionized in a dedicated ion source chamber and then accelerated up to the required energy level by several acceleration grids. Then the ion beam is neutralized passing through a neutralizer; in the present experiments, this device is a gas chamber, where the charge is removed by impacting with a back-ground gas of the same species of the beam. The remaining ions in the beam are deflected by electrostatic or magnetic fields and collected by the residual ion dump device. After that, the fast-neutral particles are injected into the vacuum vessel, following straight lines until, thanks to Coulomb collisions, their energy is transferred to the plasma (slowing down process). ITER will be equipped by a 33 MW NBI system made up of 2 injectors. In section 3 Neutral Beam Injection systems will be more closely addressed.

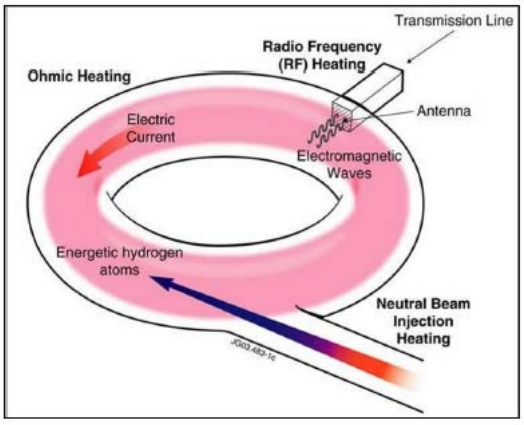

Fig. 2.2. Ohmic heating and additional H&CD systems

2.3 ITER

ITER is the world's largest and most advanced fusion experiment and its main purpose is to be the first magnetic confinement device to produce a net surplus of fusion energy. It is designed to generate 500 MW fusion power, equivalent to the thermal output of a conventional medium size power plant, for typical plasma pulse of 400 to 600 s [4]. For a planned injected power of about 50 MW (from additional H&CD systems) this corresponds to a fusion gain Q=10 in the plasma. ITER is not intended to release any electric power from fusion reactions to the grid but it will collect some key technologies for a DEMO fusion power plant. The ITER's first plasma is scheduled for December 2025 and Deuterium-Tritium operation is expected to begin by 2035. ITER is being built in southern France (Cadarache) in the framework of collaboration between seven country members: European Union, India, Japan, Korea, Russia and the United States.

The realisation of fusion energy depends completely on ITER's success, which is based on the fulfilment of the following specific targets:

1. Increase the output power and the confinement time (500 MW for hundreds of s);
2. Demonstrate and validate the essential technologies for the reactor, like superconductive magnets, the High-Voltage power supply, the NBI components and so on;
3. Achieve a D-T plasma in which the fusion energy is large enough to exceed the plasma heating that is injected from external sources (burning plasma);
4. Test tritium production capability inside the machine, through the *breeding blanket* solution
5. Demonstrate the environmental safety of a fusion device.

To achieve a fusion power as high as 500 MW the plasma volume must reach about 800 m^3, resulting in a plasma major radius of 6.2 m and a minor radius of 2 m. A schematic view of the ITER cross section is reported in Fig. 2.3 where the poloidal and toroidal magnets are visible, together with the vacuum vessel, the breeding blanket and the divertor. The toroidal and poloidal magnets are superconductive and they have to be maintained at cryogenic temperatures (4.5 K). For this reason, the reactor is enclosed inside a cryostat under vacuum, providing thermal insulation.

The main parameters, for inductive operation scenario I [5], are summarized in Table 2.1. Also non-inductive scenarios are foreseen, acting the H&CD systems as the only source for plasma sustainment; in this case the pulse duration can be extended up to 1 hour.

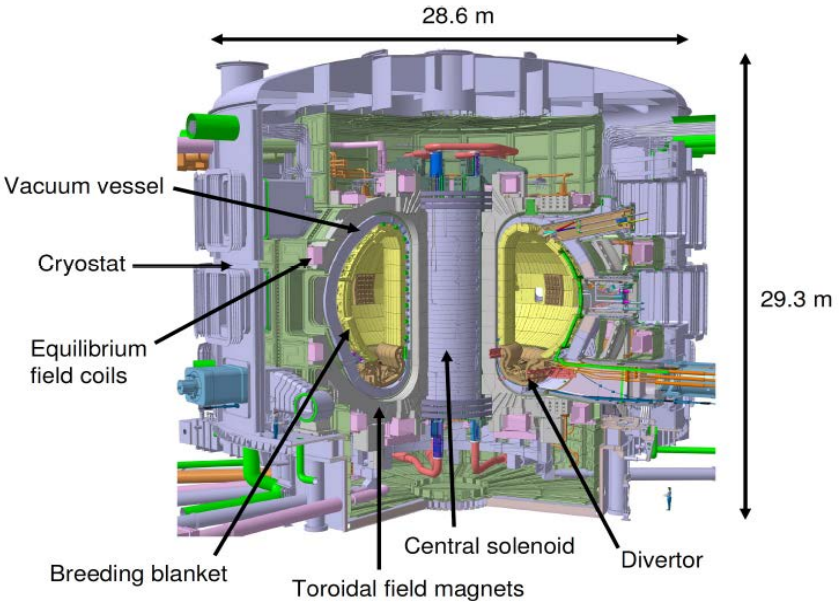

Fig. 2.3 Schematic layout of the ITER Tokamak [6].

Parameter	Inductive operation I
Total Fusion Power	500 MW
Additional power	50 MW
Confinement time	3.4 s
Toroidal field	5.3 T
Power Gain Factor (Q)	10
Cryostat height	26 m
Cryostat diameter	29 m
Plasma Volume	837 m^3
Plasma major radius	6.2 m
Plasma minor radius	2 m
Nominal plasma current	15 MA
Burn time	400 s

Table 2.1. Main ITER parameters for inductive operation scenario I

2.4 DEMO

Demo is the intermediate step between ITER and a commercial power plant and will be largely built on the ITER experience. The major requirement of DEMO will be to inject between 300 to 500 MW of net electricity into the European energy electrical grid [7]. Beyond that DEMO aims to:

- Breed its own tritium, which is part of the fusion fuel;
- Demonstrate materials suitable for handling the high neutronic influx produced during fusion reactions;
- Demonstrate safety and environmental sustainability;
- Prove the industrial and technological feasibility to allow a first commercial plant to be constructed;

To accomplish these targets, DEMO is currently designed to achieve long plasma pulses (about 2 h), minimizing the time between two next pulses. To auto-produce its own tritium, breeding blanket containing lithium shall cover most of the inner surface of the vacuum vessel. In order to compensate for non-interactions between neutrons and lithium, the blanket shall contain a neutron multiplier, beryllium. The conceptual designs all sketch out a machine that is larger than ITER.

To heat the plasma, extend the pulse time and provide various control functions three H&CD systems are developed for DEMO, namely: Electron Cyclotron (EC) System, Neutral Beam Injection (NBI) System and Ion Cyclotron Range of Frequency (ICRF) System.

Efficiency is a fundamental aspect for DEMO, since it has to demonstrate for the first time the capability to inject a significant amount of power in the European electrical grid. The cost of the electrical power produced by fusion reactions will be strongly affected by the efficiency of the overall plant, which in turn depends on the efficiency of the various sub-systems. The H&CD systems play an important role in this regard since they require significant input power, giving a large contribution in the amount of *recirculating power* (i.e. the part of fusion output power that must be used to supply the auxiliaries). Moreover, the efficiencies of H&CD systems are quite low: for ITER the expected efficiencies are about 25% for NBI and 35% for the EC system [8], making them very impacting on the overall efficiency and cost.

The present baseline under development is DEMO1, a pulsed machine. As possible alternative, a steady-state machine DEMO2 is under study with higher and more demanding physics and engineering assumptions.

3 Neutral Beam Injection

3.1 Principle and main components

The objective of the system is to provide a stable and possibly uniform fast particle beam (usually beamlets) of Hydrogen or Deuterium for the duration of the plasma discharge at a selected energy and power, injected in a direction determined by the system geometry.

It is possible to define three NBI parameters from the physical point of view: energy (E_{NBI}), power (P_{NBI}) and injection geometry. The beam energy accounts for the adsorption length for ionization in the plasma, that is the more energetic is the beam, the more it penetrates inside the plasma volume. The beam power is related to the beam density: at the same level of E_{NBI} the more neutrals are accelerated, the more power is delivered to the plasma. The beam injection geometry is the direction of the beam with respect of the plasma ring: if it is tangential then it contributes to the plasma current-drive.

The present concept of NBI foresees four main components: ion source, acceleration grids, neutralizer and residual ion dump. A scheme of concept is proposed in Fig. 3.1.

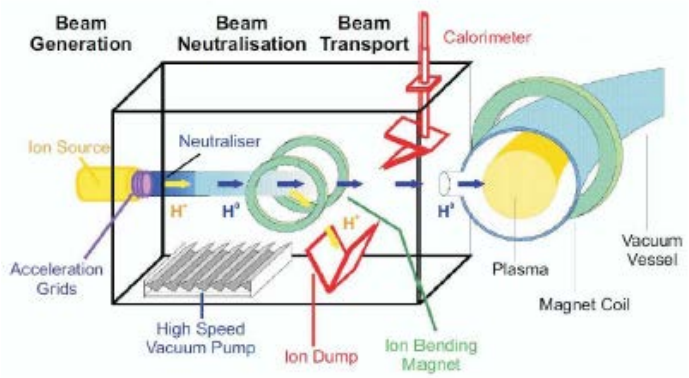

Fig. 3.1 NBI system conceptual scheme.

The ion source, providing the ions to be accelerated, can be realized with two different approaches. The first to be used is a magnetic bucket ion source containing the gas to be ionized by means of electrons emitted from filaments made of tungsten. The second one is a radio-frequency (RF) ion source where plasma of Hydrogen or Deuterium is produced by a set of external copper coils operating in the radio-frequency range. The first described method has the disadvantage of frequent maintenance and substitution of the tungsten filaments, which are subjected to deterioration due to high temperature, thus the second one (RF source) is preferable.

Then the ions are extracted from the ion source chamber with a proper electric field applied between a couple of grids: the plasma grid (PG, facing the plasma) and the extraction grid (EG). After passing through the EG the ions are accelerated by an electrostatic accelerator, comprised of a series of accelerating grids at different potentials. During all these acceleration stages the beam optics is optimized if, given a certain extraction system, the acceleration voltage and the extracted beam current follows the so-called perveance matching law:

$$I_{beam} = \frac{k}{\sqrt{m}} V^{3.2} \qquad 3.1$$

where k accounts for the extraction system geometry, m is the ions mass and $\frac{k}{\sqrt{m}}$ is the perveance coefficient.

Next the ion beam passes through a gas neutralizer in which loses its electric charge by the interaction with a background gas; unfortunately the neutralization efficiency is not so high, especially for positive and high

energy ions. For this reason, the residual ions present in the beam must be damped by the Residual Ion Dump (RID). Finally, the beam passes through the wall aperture (port) through a duct and enters the plasma.

3.2 Efficiency

It is possible to express the overall current drive efficiency, from the electric plug to the current driven in the tokamak plasma, by considering three contributions [9]

$$\eta_{CD} = \eta_{CONV}\eta_{COUP}\epsilon_{CD} \tag{3.2}$$

The first one, η_{CONV}, is the electrical conversion efficiency i.e. the ratio of the power launched by the H&CD systems to the overall electric power required to operate the system. The second, η_{COUP}, is the coupling efficiency, i.e. the ratio between the power effectively released (coupled) to the plasma and the launched heating power. The last, ϵ_{CD}, is the "physics" current drive efficiency, which measure the plasma current driven by unit of power coupled to the plasma. As already outlined in Section 2.4, there is a need to optimize the H&CD efficiency, thus all these three factors must be taken into account; in Table 3.1 the present efficiency status of the available H&CD techniques are summarised [9].

H&CD system	η_{CONV}	η_{COUP}	ϵ_{CD}
NBI	Low (range 20-30%)	High (close to 100%)	High
ECRH	Low-medium (20-30%)	High (close to 100%)	Medium
ICRH	Medium (40-50%)	Low in H-mode	Medium to high

Table 3.1 Efficiencies of the main H&CD systems available.

As can be noted the conversion efficiency is quite low for the NB systems, and the main opportunity to improve this value is increasing the neutralization efficiency. Most present NB systems are based on acceleration of positive ions, whose neutralization efficiency decreases rapidly with beam energy; since higher energy beams are required to penetrate larger plasmas, typically 500 keV to 1 MeV, negative ion beam technologies are foreseen for ITER and DEMO. The negative ion beam neutralization efficiency is almost independent on the beam energy, as shown in Fig. 3.2 [10]. Note that the wall-plug efficiency η_{CONV} is also influenced by the NBI power supply efficiency; the ITER NBI power supply will be addressed in Section 3.4.

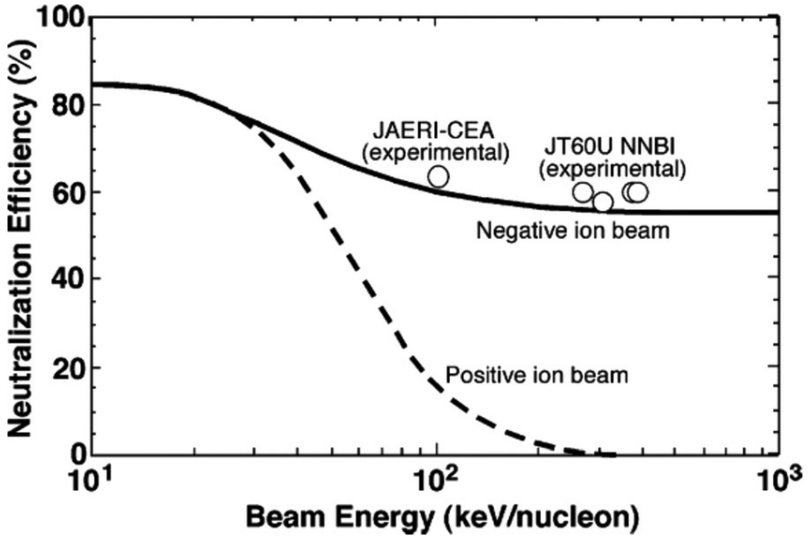

Fig. 3.2 Neutralization efficiency for negative and positive ion beam.

3.3 ITER NBI

The ITER Heating Neutral Beam Injectors (HNBs) are designed to deliver 16.7 MW of 1 MeV D^0 or 0.87 MeV H^0 to the ITER plasma for up to 3600 s. They will be the most powerful NB injectors ever, delivering higher NB energy to the tokamak plasma for a time longer than any previous system. The design is based on the acceleration and neutralization of negative ions, since their neutralization efficiency remain acceptable (≈56%) at the energy required for the ITER NB. Negative ions are in contrast more difficult to create and handle and the system design is more complicated compared to a positive NB. One of the major difficulties is the large production of negative ions, which shall be enhanced by covering the inner surface of the source and the plasma grid with Cs (Caesium), acting as a catalyser. However, Cs pose other issues for its reliable injection and the source maintenance.

In Fig. 3.3 a schematic view of the ITER HNB is represented [11]. To give an idea of the device's dimension the total length of beam line is about 15 m. The beam is connected to the very high voltage (1 MV dc) power supply by a SF_6 gas-insulated Transmission Line (TL). A high voltage bushing separates the high pressure of the transmission line from the high vacuum in the beam vessel. The main components previously described, ion source, accelerating grids, neutralizer and RID are visible in figure. The ions generation inside the expansion chamber is activated by means of 8 cylindrical RF drivers and enhanced by Cs injection from 3 caesium ovens.

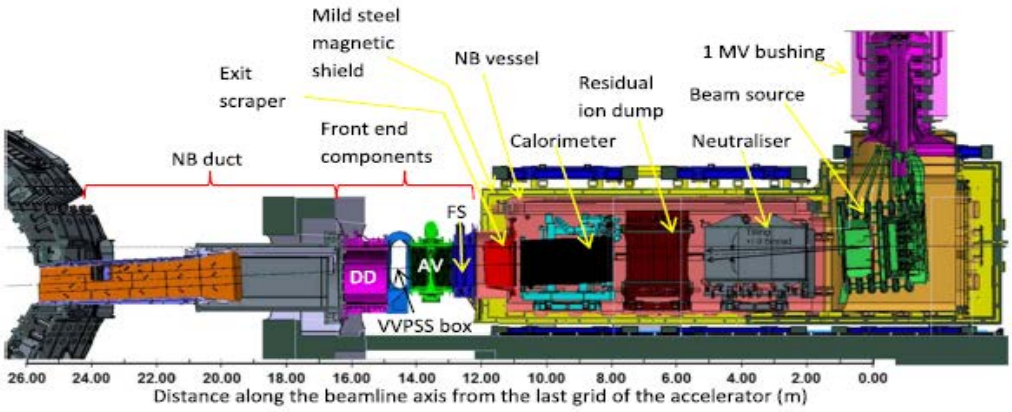

Fig. 3.3. Computer generated cut-away view of an ITER HNB.

The NBI power flow [12], from the input electrical power to the launched power into the plasma, is visible in Fig. 3.4; here, the terms of loss influencing the conversion efficiency are represented. As can be seen the plug-in power of about 60 MW is initially partially dissipated in the Power Supply (PS) system and TL. Inside the beam source some part of the power is lost in the accelerator stadium, where the main losses are due to acceleration of stray particles and stripping losses (electron detachment from the negative ion). In the beam line some power is lost in the neutralizer, but the principal term of loss is due to the RID stage (17-18 MW). This is the main system term of loss and is due to the low neutralization efficiency: many ions remain in the beam after the neutralization process thus their energy is lost, because they are deflected by the RID. The total exiting power launched into the plasma is about 16-20 MW.

A short description of the Electrostatic accelerator is given. The NBI electrostatic accelerator is based on a Multi Aperture Multi Gap (MAMuG) configuration, meaning that each accelerating grid has many aperture and there are several acceleration stages realized with a set of grids at different potentials. Five acceleration grids at increasing potential are used in the ITER HNBs, with the last grid (Grounded Grid, GG) referred to the NBI ground reference (the vacuum vessel). In D-operation the rated voltage across each couple of grids is 200

kV, reaching a total acceleration voltage of 1 MV; the ion source is thus at -1 MV potential with respect to the NBI vessel. A simplified view of the MAMuG electrostatic accelerator is shown in Fig. 3.5. In the past another approach has been used, namely the Single Aperture Single Gap (SINGAP). This kind of electrostatic accelerator envisages one single voltage step from 0 up to the rated total acceleration voltage; this makes the approach simpler to realize but implies higher losses due to stripping and stray particles acceleration. For this reason, the MAMuG configuration is preferable in order to preserve an acceptable level of efficiency, although some considerable issues remain to be faced. Indeed, voltage holding is recognized as an issue in multi-aperture accelerators; due to the short distance among accelerating grids, breakdowns in the accelerator are expected to occur frequently and the related power supply must be able to withstand them. Studies are in progress to combine the advantages of MAMuG and SINGAP configurations for DEMO. Moreover, the magnetic field foreseen to deflect the stray electrons before being accelerated can decrease the voltage holding capability [13].

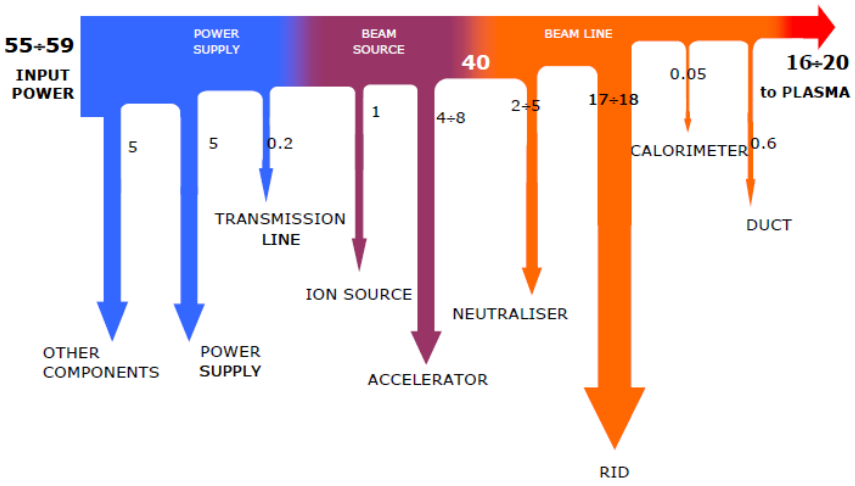

Fig. 3.4 NBI schematic power flow along the beam line

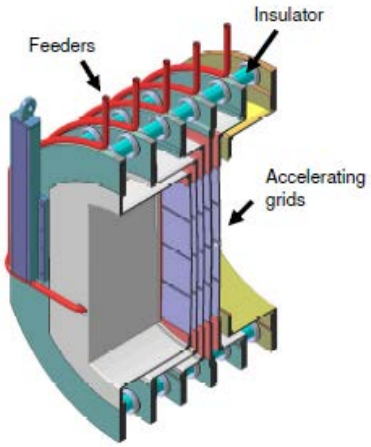

Fig. 3.5. MAMuG electrostatic accelerator.

3.4 PRIMA: the Neutral Beam Test Facility (NBTF) in Padova

The prefixed operating conditions for the ITER NBI (see Table 3.2) have never been reached jointly before and it was recognized the necessity of a dedicated international R&D programme aimed at constructing, testing and optimizing the full-scale prototype of the ITER NBI.

The Neutral Beam Test Facility (NBTF) is ITER NBTF is hosted at Consorzio RFX in Padova, Italy (Fig. 3.6) and it is carried out in the framework of collaboration between Consorzio RFX, European, Japanese and Indian Domestic Agencies, the ITER Organization and several European laboratories. It includes two experiments: MITICA, the full-scale prototype of the ITER HNB injector and SPIDER, the full-size radio frequency (RF) negative-ion source.

The mission of SPIDER (Source for Production of Ions of Deuterium Extracted from RF plasma) is to optimize the negative ion source performance for the ITER HNBs and validate the source design. SPIDER specific requirements can be found in [14]. At this purpose it has a wide set of diagnostics tools, necessary to measure the various parameters of the plasma and beam optics.

The MITICA (Megavolt ITER Injector and Concept Advancement) experiment, represents a large step forward in terms of power and energy output compared with the actual NBI experiments. It will represent a testbed to achieve the full performances required for ITER NBI. MITICA will be equipped with additional diagnostic tools with respect to the ITER HNB and it shall be operated at full power, discharging all the beam energy into the calorimeter. The R&D programme of SPIDER will address the main issues specifically related to the negative ion source, while MITICA will be mainly focused on the 1 MeV beam acceleration. A sketch view of the MITICA injector is shown in Fig. 3.7.

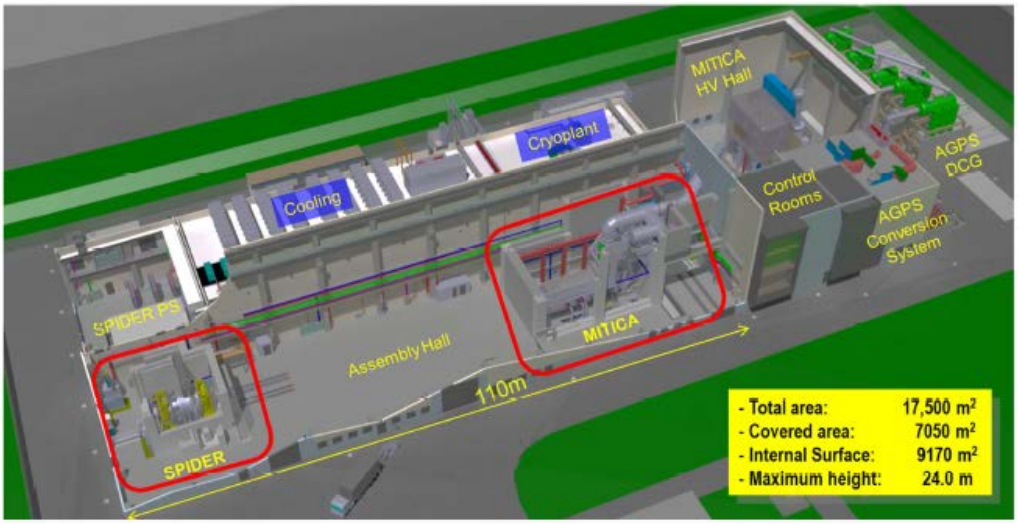

Fig. 3.6 3D CAD view of the PRIMA facility [14]

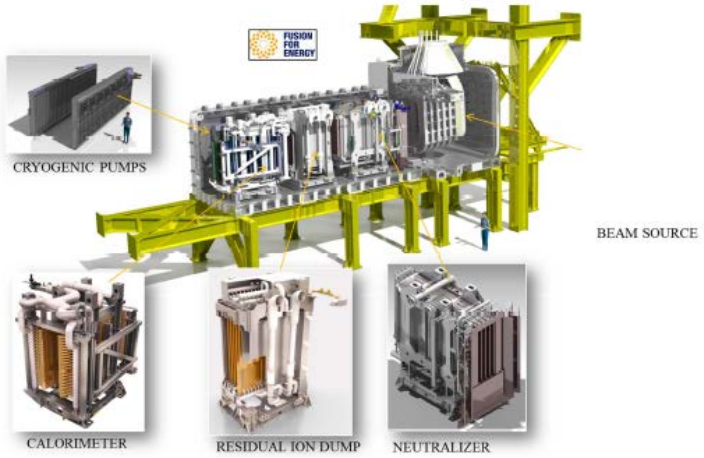

Fig. 3.7 View of the MITICA injector with in-vessel components [14].

3.5 DEMO NBI

A conceptual design of the DEMO NBI is currently being developed by Consorzio RFX in collaboration with other European research laboratories [15]. The proposed design includes 2 ion source modules with 4 racetrack RF drivers in total, 7 grids and 5 acceleration stages, each grid being composed of 8 segments, with the following advantages: better optics due to the reduction of the thermal deformations, easier manufacturing. However, some of the design solutions envisaged for DEMO NBI (like the plasma-neutralization process) are still on R&D phase and their effective realization is still to be demonstrated; thus the design considered is referred to a wished "Advanced DEMO NBI". In Table 2.1 a comparison between the ITER and DEMO NBI is reported.

	ITER	**Advanced DEMO**
Species	H^-/D^-	D^-
Beam energy (keV)	1000	1000
Beam current (A)	40	TBD
Beamlet divergence (mrad)	<7	<7
Beam on time (s)	3600	7200
Neutralization efficiency	Not specified, ~0.55	>0.7
Extracted e^-/D^- fraction	<1	<1

Table 3.2 Main requirements for ITER and DEMO NBI. The neutralization efficiency is not a requirement in ITER [16] [15].

4 Overview of the power supply for ITER NBI

4.1 Review of power supply systems for NBIs

The neutral beam is created and accelerated by means of mainly two power supply systems, namely AGPS and ISEPS. The first one provide the High Voltage (HV) to the acceleration grids and the other, referred to the HV potential, supplies the ion source and its auxiliaries. A scheme of principle of a negative ion-based NB injector [17] is shown in Fig.4.1.

In the first Positive Ion-based NB Injectors (PINIs) the ion source and the beamline components were placed in the Tokamak hall. The power supply feeding the grids was composed by an input stage with an outdoor HV transformer-rectifier followed by a filter capacitor and an ignitron crowbar at the DC side, located in an isolated HV deck inside the NB building. The output was connected to a modulator section comprised of a power tetrode which either regulates the power of the NB and switches off in case of an electrical breakdown (BD). The ion source power supply was installed in a SF_6 insulated box (since it is referred to the accelerating voltage) located near the beam source to reduce the length of lines carrying high currents. This kind of power supply system with some modifications relies on DC switches for the current interruption in case of BD.

The PINI systems are characterized by acceleration voltage in the 100 kV range; in the next years the higher acceleration voltages required (500 kV and beyond) to heat larger tokamak plasma shifted the interest on negative ion-based systems, for their higher neutralization efficiency. The use of DC switches for BD protection was no more feasible for this range of voltage and a new approach based on switching inverters (at ground potentials), step-up transformers and diode rectifiers was adopted, made possible by the progress in power semiconductor area. This scheme relies on the inverter fast switching for both modulation and fault interruption, which is provided at the low voltage side; this kind of approach is currently adopted in the MITICA NBI power supply.

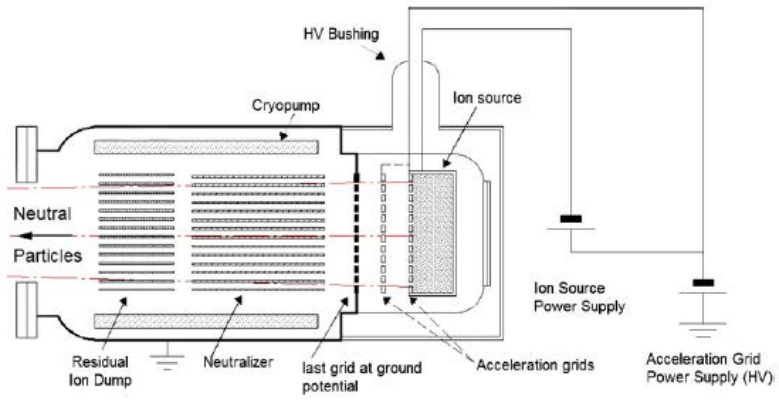

Fig. 4.1. Scheme of principle of a negative ion-based NBI: it can be seen that the Ion Source power supply is raised to the (negative) potential of the AGPS.

4.2 The ITER power supply system

The ITER HNB power supplies can be divided into three main systems [14]:

- AGPS, devoted to supply the acceleration grids up to -1 MV, through the high voltage Transmission Line (TL) and bushing;
- ISEPS, comprising the ion source devices (RF driver, caesium oven, plasma grid and others) and the extraction grid which are all electrically referred to the ion source, which is at -1 MV to ground;
- GRPS (Ground Related Power Supply), including the RIDPS (Residual Ion Dump PS) feeding the electric panel of the Electrostatic Residual Ion Dump (ERID), and the CCPS (Correction Coil PS) feeding the coils aiming at reducing the stray magnetic field in the beam line.

The complexity of the ITER PS system relies not only in the unprecedent requirements in terms of voltage and power but also in several design choices such as the location of the PS components with respect to the injectors and the choice of which to be referred to the ground. The final design foresees to move all the electrical and electronic equipment far from the neutronic area (i.e. to the beam line) and to place the ISEPS on a high voltage deck named HVD1, air insulated for -1MV to ground and acting as a Faraday cage, supplied with only one insulating transformer. This configuration of the ISEPS [17] has the major benefits of making full accessible the ion source power supplies, once the system is deenergized, and to resolve the critical issue of realizing a -1 MV and 1 MHz insulating transformers, for the RF generators.

In Fig. 4.3 a global view of the ITER/MITICA PS systems is reported. The HV components, in blue in the figure, comprising the TL, insulation transformer, HVD1 and step-up transformers with diode rectifiers are provided by the Japanese Domestic Agency (JADA), whereas all the other components by the European Domestic Agency (Fusion For Energy, F4E). The AGPS and ISEPS (contained this last in the HVD1) are connected by a special SF_6 gas-insulated HV Transmission Line, more 100 m long. The external size of HVD1, hosting the ISEPS, are of 12 m × 8 m × 10 m (L × W × H) and it is raised of 6.5 m by post insulators. The connection between the ISEPS outputs and the TL is realized by a High Voltage Bushing Assembly (HVBA), installed under the HVD1. The overall electrical scheme of the power supply for the MITICA NHB is reported in Fig. 4.3; the corresponding for ITER is identical, except for the grid network connections. In the following section a more detailed description of the AGPS will be given, which is the main focus of the thesis.

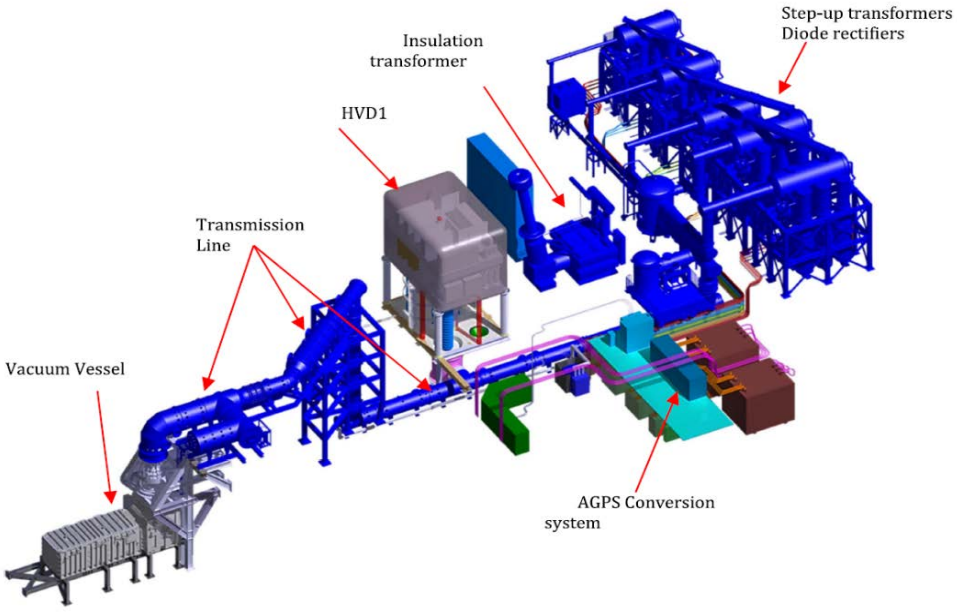

Fig. 4.2 3D view of the MITICA power supply system.

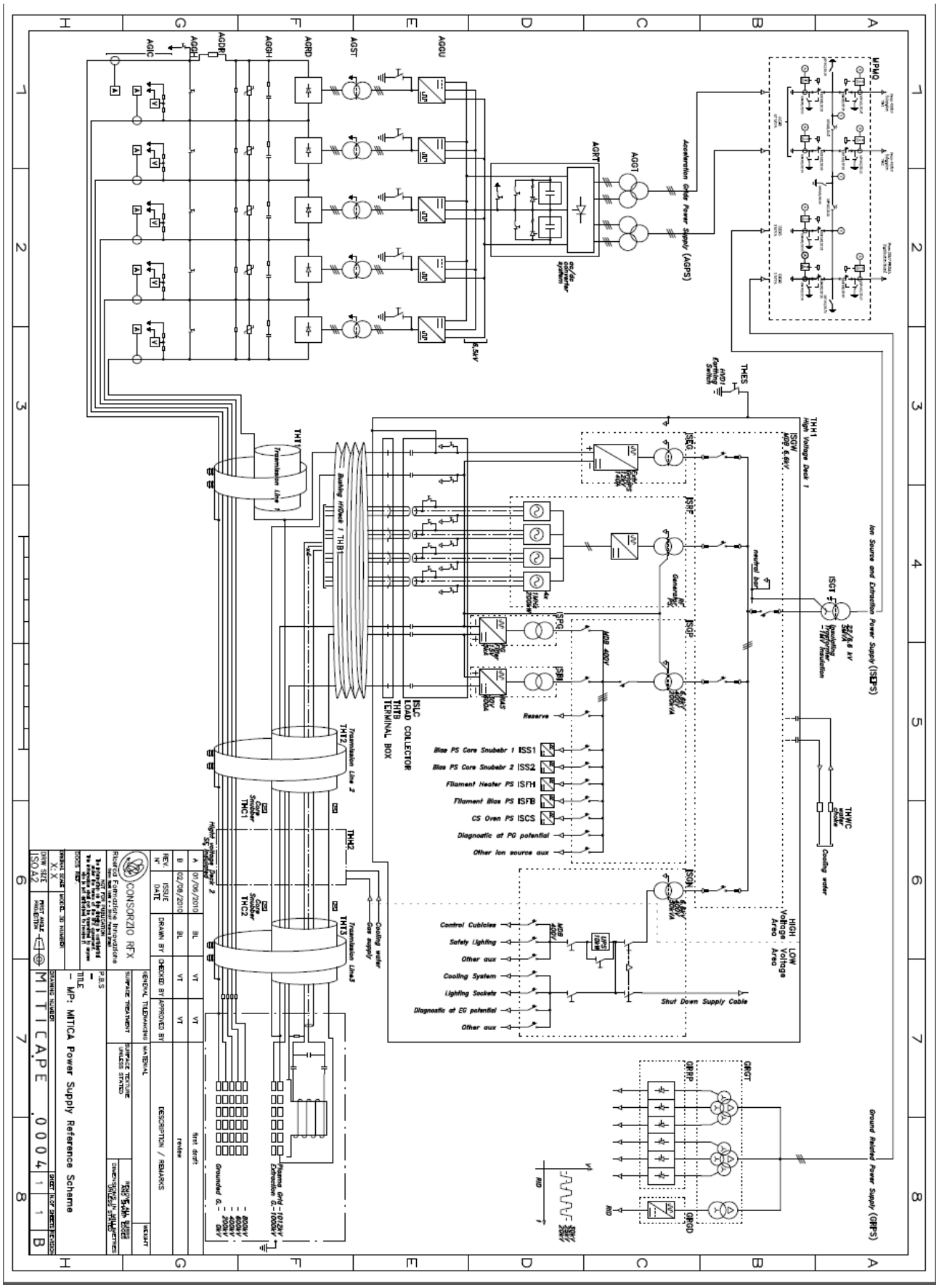

Fig. 4.3. Reference electrical scheme of the MITICA power supplies [6]

4.3 AGPS

In ITER, the AGPS is fed by the 66 kV ITER medium voltage (MV) grid. A dedicated 66 kV circuit breaker is envisaged, able to interrupt the full current in severe fault case. Moreover, a disconnector and an earthing switch are foreseen to completely discharge the AGPS components when it is not in use. In MITICA, instead, the AGPS is fed at 22 kV by two withdrawable circuit breakers [6].

The AGPS can be divided in two sections, a power Conversion Stage (AGPS-CS, to be procured by F4E) and a DC-Generator system (AGPS-DCG, to be procured by JADA):

- The aim of the AGPS-CS is to adapt the medium voltage supplied by the ITER and MITICA distribution grid to supply the AGPS-DCG, and to regulate the acceleration voltage at the output of the AGPS-DCG. Therefore, it is an AC to AC conversion system capable of regulating the ac voltage at the output, using as feedback the dc output voltage of the AGPS.
- The AGPS-DCG is the load of the AGPS-CS. It includes five AC/DC HV units connected in series at the output side. Each unit is designed to provide a DC output voltage of -200 kV. The outputs of these unit are connected to a DC filter.

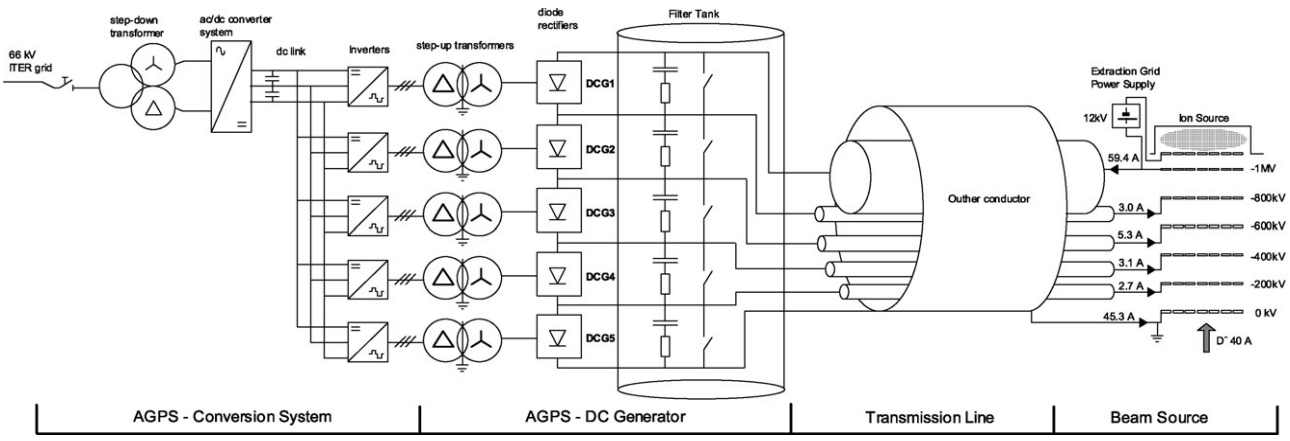

Fig. 4.4. Reference scheme of the AGPS, with the nominal DC output currents for D^- operation.

The reference scheme of the AGPS is shown in Fig. 4.3, where are visible the components belonging to the AGPS-CS and AGPS-DCG. It consists of a step-down transformer feeding an ac/dc conversion system (based on two 12 pulse thyristor bridges in series), which in turn feed a common dual DC link. Five Neutral Point Clamped (NPC) three-phase inverters based on solid state switches (IGCTs) are fed by the dual DC link and supply a step-up transformer each. The step-up transformer feeds a diode rectifier; the diode rectifiers are connected in series at the output side to obtain the nominal acceleration voltage (- 1 MV for deuterium operation). Of course, the high voltage side of the AGPS must be insulated from the low voltage side; this is accomplished with the step-up transformers, rated to be insulated from the ground at voltages decreasing from -200 kV to -1 MV. The AGPS scheme is completed by a DC filters, placed immediately downstream the diode rectifier, mainly to limit the voltage ripple and the overvoltage at beam off (loss of load). Diode rectifiers and filters are placed inside tanks and insulated with SF_6 gas. Finally, the DC filters outputs are connected to the acceleration grids by means of the HV TL insulated with SF_6 gas, comprising intermediate potential conductors to supply the intermediate grids.

In this scheme, the DCG output voltage is controlled by the varying the AC voltage applied to step-up transformers; to do this the modulation index of the AGPS-CS inverters is controlled in feedback.

This configuration, comprising intermediate potential grids which also collect part of the beam current, refers to the MAMuG configuration. ISEPS and AGPS control respectively the beam current and grid voltages so as Eq.3.1 is satisfied, in order to assure the focusing of the beam (perveance matching conditions).

4.3.1 Main output electrical requirements

On the basis of the voltages needed for ion acceleration listed in Table 3.2 for the ITER NBI, and of the estimation of the current distribution among the different grids, the nominal voltages and currents required at the output of each AGPS-DCG stage are obtained [18]. In Table 4.1 are reported the values for Deuterium and Hydrogen operation.

The difference between the currents of two consecutives stages represents the beam current intercepted by the grid common to the two DCG outputs.

In addition to current and voltage, it is specified that the AGPS-CS shall deliver up to 54.7MW of active power.

	D-operation		H-operation	
Stage	Voltage [kV]	Current [A]	Voltage [kV]	Current [A]
DCG1	200	62	174	66
DCG2	200	59	174	64
DCG3	200	54	174	59
DCG4	200	50	174	56
DCG5	200	48	174	54

Table 4.1 Nominal voltages and currents required at the output of the AGPS-DCG stages

4.3.2 Main regulation and dynamic requirements

The regulation of the output voltage must comply with dynamic and precision requirements [19] summarized in Table 4.2.

Parameter	**Value**
Voltage regulation range	20-100% of the nominal value
Current range[1]	0-100% of the nominal current
Voltage resolution range	1 kV
Output voltage accuracy for 1 h operation[2]	±2% with respect to the full voltage
Maximum voltage fluctuations[3]	±2.5% at flat top
Maximum voltage ripple[4]	±5%
Maximum rise time of the DCG voltage[5]	80 ms
Maximum settling time[6]	50 ms
Max. undershoot at beam on[7]	15%

Table 4.2 Requirements for the AGPS output voltages

1. In normal operation the AGPS current values will be determined by the beam current. The beam current, controlled by ISEPS, will be set as required by the “perveance matching law”.

2. Defined as the maximum per unit error of the average DCG output voltage with respect to the rated output voltage, without considering the ripple and temporary voltage fluctuations. It takes into account i.e. for the precision of the DCG voltage transducers on the overall range of variation of the system temperature.

3. Defined as the maximum per unit fluctuation of the instantaneous DCG output voltage with respect to the average DCG output voltage, without considering the ripple. It is generally due to transient phenomena.

4. Defined as the maximum per unit oscillation of the instantaneous output voltage with respect to the average output voltage in steady state condition, due only to the switching action of the AGPS conversion system. This value shall be guaranteed for the overall voltage regulation range, both in Hydrogen and Deuterium operation in nominal conditions.

A low voltage ripple assure a good focusing of the beam.

5. To reach 90% of the full DCG output voltage. The rise time is specified in two conditions:

- with the RF power on the ion source regulated to obtain the perveance matching;
- without load;

6. Defined as the time between the 90% of the full DCG output voltage and when the DCG output voltage is within the accuracy range.

7. Defined as the DCG voltage undershoot (without considering the ripple) with respect to the full voltage, for a ramp-up of the beam current in 20 ms from 10% to 100% of the optimum required for perveance matching.

In the following sections dynamic and precision requirements regarding normal operating conditions and anomalous operating conditions are addressed.

4.3.3 Normal operating sequence

The AGPS must produce the required acceleration voltage for the HNBI, following a voltage reference sent by the control system. The RF power delivered to the ion source drivers, the extraction voltage and the acceleration voltage shall be controlled simultaneously, to optimize the beam optics.

The typical operating sequence of the AGPS is the following [18]: at beam initiation the AGPS-CS is switched-on to supply the AGPS-DCG; then the required acceleration voltage is produced by controlling the DCG-AGPS output voltage in feedback.

Simultaneously the ion source RF drivers are controlled to produce the required extracted ion current, according to two scenarios:

• start-up in “perveance matching” (see Eq. 3.1): when the AGPS DC output voltage ramps up, the ion source starts to generate the ion beam to produce an accelerated current that corresponds to 80-90% of the optimum value. When the acceleration voltage approaches the set-point, the ion beam current is further increased to reach 100% of the optimum value.

• start-up at maximum voltage: the AGPS shall ramp-up to the full requested voltage without load, and then the beam current will increase up to the 100% of the optimum value.

At the end of the HNBI pulse, the AGPS-CS dc/ac conversion system is switched off. The sequence of activities above described are schematically depicted in Fig. 4.5.

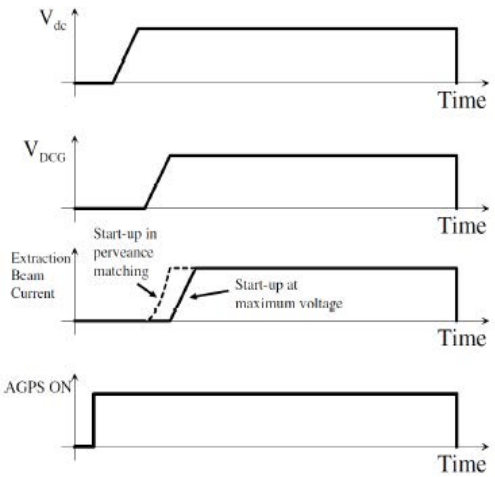

Fig. 4.5. Sequence of operation and main output waveforms of AGPS. For the beam current in dashed line the perveance-matching start-up and in continuous line the start-up at maximum voltage [15].

4.3.4 Breakdown

The inherent operation of the HNBI is close to the voltage withstand capability and frequent unpredictable breakdowns (BDs) between the acceleration grids are expected. These BDs have not to be considered as faults and they must be continuously managed by the AGPS without permanently stopping the HNBI operation. From the point of view of the AGPS, these BD appear as short-circuits of the load, resulting in over-currents at the output of the AGPS-CS inverters. Therefore, BD shall be properly detected, in order to timely switch off the dc/ac inverter switches and consequently limit the extra energy delivered to the grids and thus avoid damage. After a certain time, in the order of ms, the cause of the BD is assumed to be cleared and the AGPS-CS can restart. The reapplication of the voltage will be required not sooner than 20 ms after the BD occurrence; the AGPS-CS is designed to be ready to restart within this time. Moreover, the voltage ramp-up to the set-point must comply with the dynamic and precision requirements already described in Section 4.3.2. Requirements to AGPS concerning BD are summarized in Table 4.3.

Parameter	**Value**
Maximum detection time[1]	50 μs
Maximum switch off time[2]	100 μs
Time to be ready to restart after a BD	20 ms
Maximum number of grid BD for a single pulse	200 total
	50 consecutive

Table 4.3. Operative requirements for grid

1. Detection time is defined as the time between the BD and the triggering of the AGPS BD sequence.

2. The switch-off time is defined as the time between the triggering of the AGPS BD sequence and the time when all the AGPS-CS dc/ac inverter active switches are turned off.

The energy discharged to the grids in case of BD shall be minimized to avoid damages to the grids. The major contribution comes from the DC capacitor filter, the overall inductance seen by the inverters and the stray capacitances of the HV components to ground. A minor contribution is given also by AGPS-CS, due to the switch-off delay.

4.3.5 Beam-off

A beam-off (BO) consists in a sudden and unintentional interruption of the beam current, occurring without the simultaneous and coordinated switch-off of the AGPS-CS. From the AGPS point of view a BO is equivalent to a loss of load, resulting in overvoltage at the output of the AGPS-DCGs due to the release of energy from the upstream inductances (short-circuit inductance of the transformers and output inductance of the inverters). A BO shall be properly detected and the AGPS control must be able to quickly switch-off to limit the arising overvoltage at the output, which could be dangerous for the HV AGPS electrical components. The BO event is treated as a fault condition and the maximum switch-off time shall be less than 100 μs and the maximum overvoltage is 20% of the nominal value.

4.3.6 Main electrical interface parameters

As already mentioned in Section 4.3 the AGPS-CS belongs to the EU procurement, whereas the AGPS-DCG pertains to the JA procurement. To guarantee the correct working of the overall system and at the same time optimize the overall AGPS design a set of electrical interface parameters between the two procurements has been formalized. The most important interface parameters [19] are the inverter switching frequency, the overall inductance seen by the inverters (comprising short-circuit inductance of the step-up transformer and inverter output inductance), the DC-link voltage and the shape of the inverters output. In Table 4.4 a list of the main electrical interface parameters [6] is reported.

The DC filter is introduced with the main goal of limiting the over-voltage at the beam-off, even if it also contributes in output voltage ripple reduction. The DC filter is introduced with the main goal of limiting the

over-voltage at the beam-off, even if it also contributes in output voltage ripple reduction. The overvoltage at the beam-off depends essentially on the value of the capacitances and upstream inductances and on the switch-off delay time.

The capacitance value must be selected to limit the overvoltage below the 20% of the nominal output voltage and at the same time it must not be too high, otherwise in case of BD an excessive amount of energy is transferred to the acceleration grids. The filter is completed by series resistances, to limit the peak current to the grids in case of BD.

Parameter	Value
DC/AC inverter topology	3-phase Neutral Point Clamped
DC-link voltage:	
-nominal value	6.5 kV
-maximum variation in stationary regimes	±5%
-maximum variations in transient conditions (beam on and beam off)	±9%
Output voltage waveform from each inverter	3-level square wave with variable duty cycle
Inverter frequency	150 Hz
Equivalent inverter inductance for each phase (output decoupling + stray inductance)	110 μH
Maximum output DC current component from inverters	1% of the rated output current of the inverter
Step-up transformer connections	Delta/star
Step-up transformer short-circuit inductance (measured at the secondary side)	0.194 H
Step-up transformer ratio (primary/secondary)	1/18.2

Table 4.4 Main electrical interface parameters between AGPS-CS and AGPS-DCG

4.4 Considerations regarding the actual AGPS design

On the basis of the AGPS current design above described it is possible to individuate some critical points that call for exploring and evaluating alternative solutions which could mitigate them. The main critical points are the following:

1. **Double conversion stage**.
2. The electrical energy passes first trough an AC/DC conversion step, then to a DC/AC one and finally to the last AC/DC conversion with the diode bridges. This means higher conversion losses with respect to a single-stage solution.
3. **Reduced controllability of DC voltage output and energy discharged during BDs.**
   The output DC voltage is regulated by means of the modulation index of the 3-level NPC inverters. Between the inverters and the grids there are several devices (see Fig. 4.4) that introduce voltage drops and delay in the dynamic response. These effects are compensated by means of a closed-loop control of the voltage (measured at the DC filter); however, with a direct regulation of the DC output voltage the control might be faster and more accurate. Moreover, the fast interruption of the current in case of BD is relied on the inverter fast switch-off, all the storage elements downstream the inverters discharge their energy into the short-circuit without any active control. The contributions to the energy discharge are the DC filter capacitance, the overall inductance downstream the inverters and stray capacitances and inductances. Since the breakdown must not damage the AGPS system, passive devices (such as resistors and core snubbers) are conveniently placed in the transmission line to partially dissipate the energy and limit the current peak.
4. **High DC link energy**.
   The DC link capacitors at the output of the first AC/DC conversion stage (thyristor based) are distributed among the inverters to reduce the stray inductance at the input. The total capacitance is

rated to keep the DC link voltage at an acceptable level during load transients, especially when the load is inserted or increased; therefore, its value depends on the dynamics of the rectifier upstream. Since the line-commutated thyristor rectifiers have comparatively slow response, the total DC link capacitance is considerable (about 50 mF [6]). If one of the IGCTs of the inverter leg fails, i.e. it loses the voltage blocking capability, a short-circuit of half DC link can take place, because it is shared between all the inverter DC side. The energy stored in half DC link is discharged through the faulty leg and if a proper protection is not foreseen (fuses), the fault propagation can lead to module explosion.

5. **SF_6 insulated parts.**
   The high-voltage diode rectifiers and the DC filter are placed inside tanks SF_6 gas-insulated. This gas has much higher dielectric strength than air or dry nitrogen, but it has a very high Global Warming Potential and it is potentially dangerous for workers. This complicates the management and maintenance of the plant.

Considering all these aspects the utilization of Modular Multilevel Converters for future NBI AGPS could be a promising solution which is worth to evaluate. The key-feature of this topology is the modularity structure which could simplify the design and increase the continuity of operation. In addition, it could mitigate some of the issues previously described:

- one single conversion stage is realized thus the efficiency is expected to be higher;
- the DC output voltage is directly controlled;
- the ripple is expected to be low and thus the DC filter could be reduced in size (reduced energy discharged to the grid during BD);
- the dynamic response of the MMC topology is expected to be faster, therefore the distributed DC link could be underrated with respect to the MITICA AGPS. This means lower energy discharged during internal faults.
- No SF_6 insulated parts, since the MMC topology is air insulated (but this implies also higher clearance to be taken, thus higher building volumes).

5 Modular Multilevel Converters (MMCs)

5.1 Introduction

Until the 1970s the AC/DC electrical power conversion was dominated by the Current Source Converters (CSCs), which are operated by natural commutations. Also, converters for HVDC application made use of CSCs, first with mercury arc valves and then with thyristors. The advent of power semiconductor (PS) with turn-off capability has introduced several benefits including the independent operation from the AC grid, the increased controllability and improved harmonic performances. The Voltage Source Converter (VSC) era was opened and its expansion covered several fields, like power conversion for Renewable Energy Sources (RES), variable speed operation of AC motors and grid power transmission. For this last, particularly advantageous is the capability to impose any voltage on the AC side, thus controlling both active and reactive power independently. From the beginning the prevailing VSC topology was the 2-level converter, which is also actually preferred for low voltage applications. However, when the voltage rating is beyond a couple of kV there are no available power semiconductors and the 2-level topology is not suitable. To overcome this issue new valves composed of several series power semiconductors were introduced, in order to withstand increasing voltages; this kind of approach has revealed critic, especially in fault conditions, and it was not further pursued. The transition to Multilevel converter topology, instead, has made the power conversion at higher voltages possible without the series connection of power semiconductors and has increased the harmonic performances with lower switching frequencies, making the solution cost-effective. Another known topology is the Flying Capacitor Converter (FCC) [20] which in principle could be extended to any number of voltage levels (and thus reach high voltage ratings without PS series connection) but does not match the industrial implementation requirements in terms of scalability, modularity and low complexity design.

For operation at high voltage a more feasible solution is using *cascaded topologies*, that implements a series connection of submodules instead of power semiconductors. A submodule (SM) is essentially constituted by a DC capacitor and semiconductor valves. The major breakthrough which facilitates the cascaded topology expansion was the introduction of the Modular Multilevel Converter (MMC) by Prof. Marquardt in 2002 [21] [22]; a truly modular approach permitting to reach the HV transmission ratings becomes possible without the direct series connection of PSs and unfeasible manufacturing issues.

In the following sections an overview of the common topologies of SMs is given, then the basic working principle is explained, with a focus on the steady state-operation. After that, fundamental aspects about MMC dynamics and control are addressed together with the main modulation schemes and voltage balancing strategies.

5.2 Submodules and strings

In this section two basic alternatives for the converter SubModule (SM) are discussed: Half Bridge (HB) and Full Bridge (FB), respectively shown in Fig. 5.1 a) and b). The output voltage (*V*) depends uniquely on the state of the Power Semiconductor (PS) switches; the capacitor voltage (*Vc*) can be:

- inserted: *n=1* and *V=Vc*
- bypassed: *n=0* and *V=0*
- counter-inserted*: n=-1* and *V=-Vc* (only full-bridge SM)
- blocked: all the submodule switches are off; the capacitor may charge through the diodes but it cannot discharge.

Note that *n* denotes the state of the submodule. The main difference between the two topologies is about the possibility to apply the negative capacitor voltage, which pertains only to the FB SM. This fact imply a strong distinction in term of limit of operation of the two topologies as it will be shown. The series connection of N submodules constitutes a sub-module string, which gives rise to an output voltage formed by:

- N+1 levels, if the HB topology is adopted
- 2N+1 levels, if the FB topology is adopted

The output voltages of a SM string are represented in Fig. 5.2 a) and b), respectively for HB and FB submodules, where the maximum voltage level is realized when all the SM capacitors are inserted, i.e.:

$$V_{max} = NV_c = V_c^{\Sigma} \tag{5.1}$$

Until now, it has been assumed that the capacitor voltage remain constant, thus the output voltages are stepped-square wave and the SB can be considered as a controllable voltage source by simply varying the duty cycles of its switches. Actually, the capacitor voltage remains close to its nominal value in normal operating conditions and the assumption is acceptable. The necessary condition to obtain a constant capacitor voltage is that the net energy transferred to the capacitor must be zero in each fundamental period, i.e. the mean power is zero. In formulas:

$$\Delta E = \int_t^{t+T} vi \, d\tau = 0 \tag{5.2}$$

Where ΔE is the energy variation computed in a fundamental cycle (T), v and i represent the voltage and current at the capacitor terminals. The same relationship can be expressed in the frequency domain as:

$$V_d I_d + \frac{1}{2}\sum_{k=1}^{\infty} V_k I_k cos(\varphi_k) = 0 \tag{5.3}$$

where V_d and I_d are the DC components of voltage and currents, V_k and I_k the magnitudes of the voltage and current harmonics and φ_k the phase shift between them. To maintain this balance and to avoid any imbalance between the SMs generally different form of closed-loop control are implemented, which will be addressed in the following sections; in the next paragraphs the capacitor voltages will be considered constant to its nominal value *Vc*.

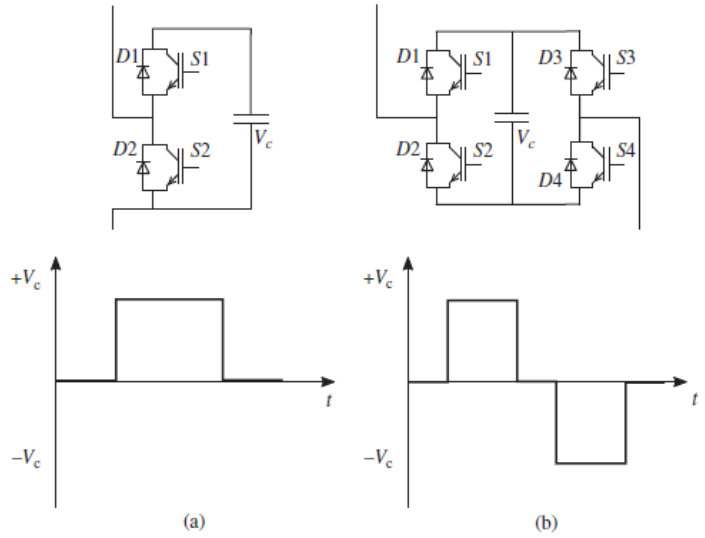

Fig. 5.1 a) Half Bridge (HB) SM b) Full Bridge (FB) SM [36]

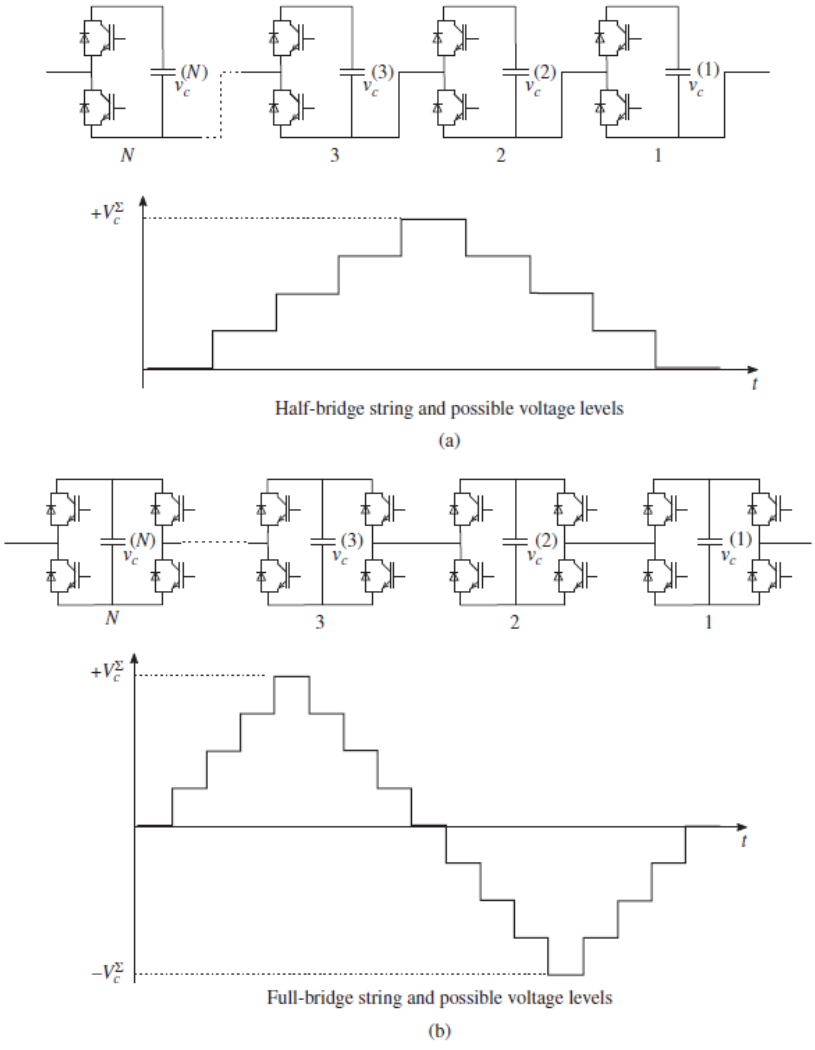

Fig. 5.2 Submodule strings and their possible output voltage: a) HB string b) FB string [36]

5.3 Topology and Basic Function

In Fig. 5.3. is represented the schematic of a 3-phase MMC for AC/DC conversion with the Half-Bridge (HB) submodule (SM) as a fundamental block. The structure can be described in the following way; each phase leg is composed by two phase arms (upper and lower); each phase arm is composed of a submodule string and a phase reactor (Larm); each SM string is made up of a series connection of N submodules. The AC terminals are derived at the middle point of each phase leg and the DC terminals at the upper and lower extremity of the phase legs. It is worth noting that in conventional AC/DC converters the presence of reactors in the phase legs is to be avoided, in order to preserve the semiconductor devices from serious damage. In MMC actually the current commutation occurs within the SM without stopping the current flow flowing in the phase leg, thus the voltage stress due to the commutation process is significatively reduced. The arm inductances, however, are introduced to limit arm-current harmonics and fault currents. The peculiar characteristic of the MMC is the capability to provide a DC voltage at the DC terminals and an AC voltage at the AC terminals independently, provided that the DC and AC voltages fall within the operational limits. The operation principle that permits such a behaviour is to control the upper and lower voltages (respectively V_u and V_l) so that their sum remain constant and equal to the DC voltage reference (V_d^*) and their difference is varying accordingly to synthetize the AC voltage reference (v_s^*). In formulae:

$$V_l + V_u = V_d^* \qquad \frac{V_l - V_u}{2} = v_s^* \tag{5.4}$$

The objective of the control are thus two, the DC and AC voltage references, and the variables of control are the arm voltages, which can be instantaneously manipulated by the proper insertion of the SM capacitors in the arm voltage. In Fig. 5.4 a scheme of this principle is shown, with reference to a single phase leg. It can be seen that the sum of the lower and upper voltage is always kept at the required DC voltage (V_d), whereas the difference is varying according to Eq. 5.4 to obtain a sinusoidal output voltage (v_s). In this sense the MMC act as a controllable voltage source both on the AC and DC side. This a remarkable difference with respect to conventional converters, which act as a current source behind a capacitor as seen from the DC side. Consequently, the AC and DC current will depend on the controlled AC and DC output voltage.

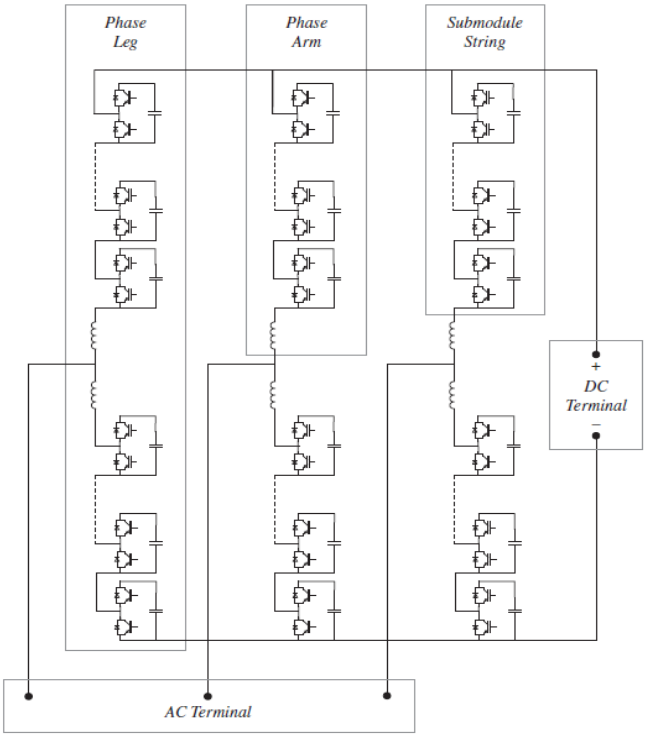

Fig. 5.3 Basic structure of a 3-phase MMC with HB submodules [36].

As already said in section 5.1 there is a strong difference in terms of operational limits between HB and FB converter topology. The first one can provide only a unipolar DC voltage and an AC voltage whose magnitude fluctuation cannot exceed the DC one; the latter can provide a bipolar DC voltage and the possibility to operate also an AC/AC conversion (no DC component). The situation is graphically explained in Fig. 5.5.

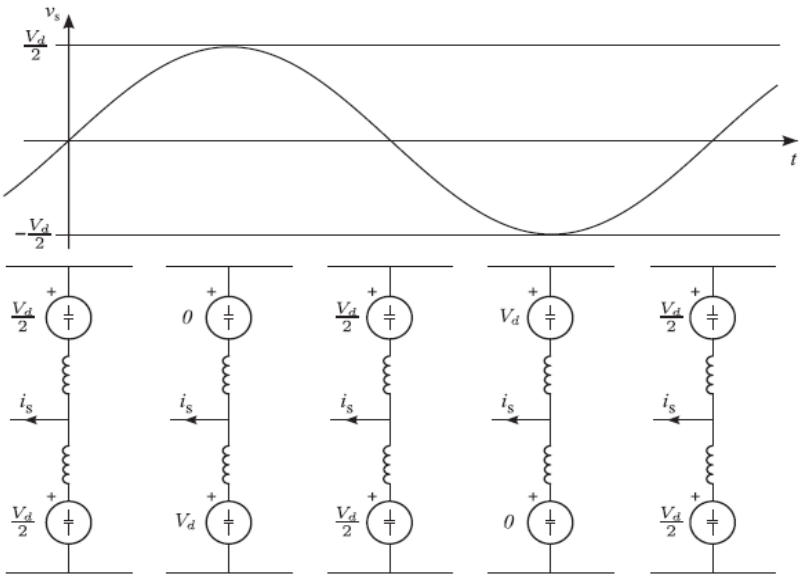

Fig. 5.4. Operating principle scheme. The upper and lower arm are ideally represented as voltage source varying continuously; this is way the inner AC voltage is continuously varying [36].

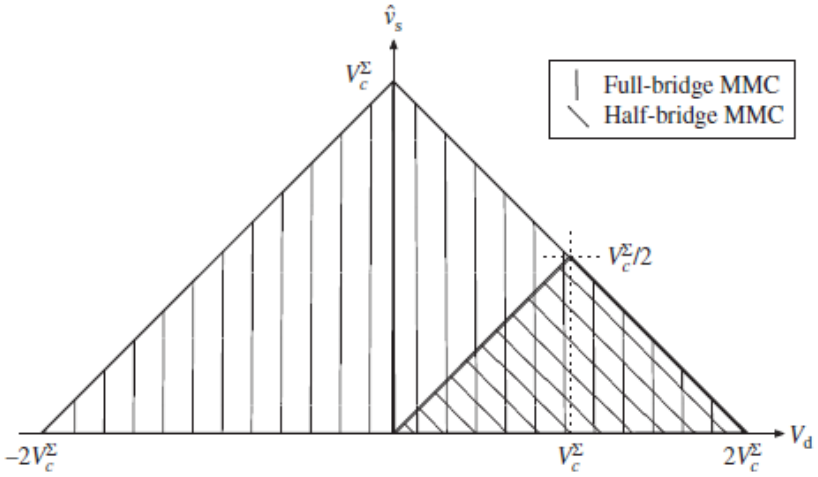

Fig. 5.5 Operating regions in terms of alternating and direct voltage of HB and FB MMCs. It has been assumed the same total submodule string capacitor voltage [36].

5.4 Main Circuit Relations

In Fig. 5.6 it is reported the per-phase schematic of an MMC with HB submodules and a general number of phases M. Assuming that the DC voltage is constant, by the application of the KVL it is possible to express the AC grid voltage in two ways, respectively:

$$\frac{V_d}{2} - V_u - Ri_u - L\frac{di_u}{dt} = v_a \qquad -\frac{V_d}{2} + V_l + Ri_l + L\frac{di_l}{dt} = v_a \tag{5.5}$$

Where i_u and i_l are respectively the upper and lower arm current, L and R the arm inductance and resistance and v_a the AC side voltage. The conventions adopted for the voltages and currents are reported in Fig. 5.6. The upper and lower arm current can be expressed as a linear combination of two components, the differential (i_s) and circulating (i_c) current, which will be useful for the analysis. The differential current is simply the current flowing at the AC side of the converter, which can be obtained applying the KCL at the AC terminal node. The circulating current, instead, corresponds to the mean value between the lower and upper arm. The main part composing the circulating current is the DC current component (I_d) which equally divides in the three phases; however, it comprises also any currents circulating between the phase legs and it is due to instantaneous imbalances of the arm voltages. In formulae:

$$i_s = i_u - i_l \qquad i_c = \frac{i_u + i_l}{2} \tag{5.6}$$

Now, adding and subtracting the two relations of Eq. 5.5, and considering the definition of i_s and i_c, yields to:

$$\frac{L}{2}\frac{di_s}{dt} = \frac{v_l - v_u}{2} - v_a - \frac{R}{2}i_s \qquad L\frac{dic}{dt} = \frac{V_d}{2} - \frac{v_l + v_u}{2} - Ri_c \tag{5.7}$$

These last two equations permit to understand how to control the dynamics of the differential and circulating currents by varying the arm voltages V_l and V_u.

From the first relation of Eq. 5.7 it can be noted that the quantity proportional to the difference between the lower and upper arm voltage drives the AC current; instead, from the second relation, the quantity proportional to the sum of the two arm voltages opposes to the flow of the circulating current. These two quantities correspond to the output (v_s) and internal (v_c) voltages, i.e.:

$$v_s = \frac{v_l - v_u}{2} \qquad v_c = \frac{v_l + v_u}{2} \tag{5.8}$$

Where v_s is the voltage generated at the AC side, behind the arm inductances, and v_c is the mean voltage between lower and upper arm (i.e. half the DC voltage, see Eq. 5.4). Substituting these two expressions in Eq. 5.7 finally yields:

$$\frac{L}{2}\frac{di_s}{dt} = v_s - v_a - \frac{R}{2}i_s \qquad L\frac{dic}{dt} = \frac{V_d}{2} - v_c - Ri_c \tag{5.9}$$

Eq. 5.9 will be the basis for the control laws analysed in section 5.7.

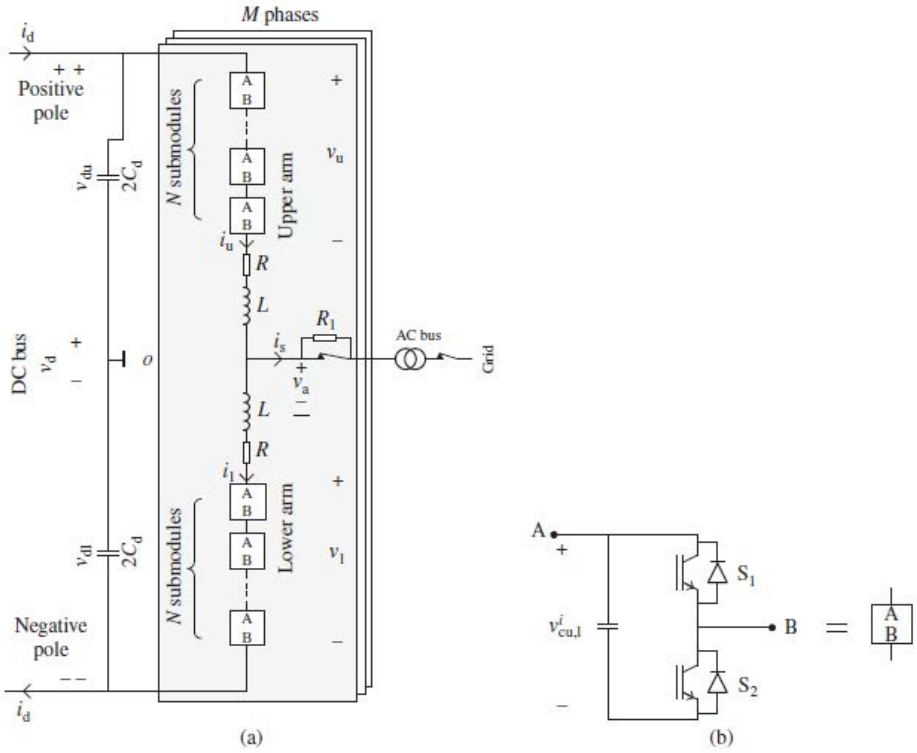

Figure 5.6 Schematic sketch of the circuit diagram of a MMC. b) HB submodule [36]

The AC/DC power conversion will be now studied in stationary conditions, and the implications for the internal energy fluctuations will be outlined. The converter should impose a constant DC voltage (V_d) as explained in section 5.3; a closed control loop is necessary to accomplish this requirement and generally V_d is approximately constant. Then it is assumed that a constant current flow in the DC link, i.e. I_d=constant, which is also roughly verified if V_d is controlled to a constant value. Then, assuming symmetric the AC grid network, a symmetric set of currents will flow in the converter legs. A power balance (see Eq. 5.2) for a 3-phase converter can be thus written as:

$$\frac{3}{2}\hat{v}_s\hat{\imath}_s \cos\varphi = V_d I_d \qquad 5.10$$

And now by defining the AC modulation index in the same way that for a 2-level converter, i.e.:

$$m_a = \frac{\hat{v}_s}{2V_d} \qquad 5.11$$

It is possible to find a reformulation of the power balance which relates the AC and DC current at steady state:

$$3m_a\hat{\imath}_s\cos\varphi = 4I_d \qquad 5.12$$

The next step is to derive the submodule string voltage and current, which can be easily obtained by Eq. 5.5 and 5.7 with some manipulations:

$$V_u = \frac{V_d}{2} - \hat{v_s}\cos(w_1 t)\,;\;\; V_l = \frac{V_d}{2} + \hat{v_s}\cos(w_1 t)\,;\;\; i_u = \frac{I_d}{3} + \frac{1}{2}\hat{\imath_s}\cos(w_1 t);\;\; i_l = \frac{I_d}{3} - \frac{1}{2}\hat{\imath_s}\cos(w_1 t)\,; \qquad 5.13$$

Once obtained the voltage and current of the lower and upper string by simply multiplying them and applying Eq. 5.10, i.e. the power balance, the instantaneous expressions of the power flowing in each string are finally obtained [23]:

$$p_u = \frac{1}{8} V_d \hat{\imath_s} [2\,cos(w_1 t) - m_a^2\,cos(w_1 t)\,cos\varphi - m_a cos(2w_1 t - \varphi)] \quad 5.14$$

$$p_l = -\frac{1}{8} V_d \hat{\imath_s} [2\,cos(w_1 t) - m_a^2\,cos(w_1 t)\,cos\varphi + m_a cos(2w_1 t - \varphi)] \quad 5.15$$

These relations offer some interesting considerations, regarding the different terms of instantaneous power exchanged with the arms. In particular it can be observed that:

- No constant term of power are exchanged at the arm level, meaning that the converter power balance is reflected at the arm level.
- The second harmonic term proportional to the modulation index, which cancels out in the DC link capacitor voltage of a 3-phase converter, here contributes to the voltage ripple, since the converter capacity is distributed among the submodules.
- There is a fundamental frequency oscillation term which has opposite sign in the lower and upper arm, meaning that this term moves forth and back between the arms.

These terms of oscillation need to be adsorbed by the submodule capacitors, consisting in voltage ripple. However, there are not only those low-frequency terms of voltage fluctuations; there is also a fluctuation that is individual to each SM and due to the switching process of the SMs. The first fluctuation term is compensated by the control stage of the converter while the second by the modulation and energy balancing stage.

5.5 DC short-circuit handling

Different considerations regarding the DC short-circuit impact must be made for the HB and FB topology.

As can be seen in Fig. 5.5, for a HB topology when the DC link voltage becomes zero, necessarily also the AC inner voltages nullify because the converter is not able to synthetize a pure AC voltage. This is particularly critical because the converter loses control of the currents and the DC short-circuit is seen by the grid as a symmetrical fault; the grid contributes to feed the short-circuit through the converter which is acting as a rectifier of the short-circuit current (see Fig. 5.7). Notably the unipolar voltages that can be provided by the converter can only add currents to the short-circuit, consequently all the SMs must be bypassed. This situation persists until the AC or DC circuit breaker opens.

In the HVDC transmission field [24] DC shorts can occur and are not rare events especially in the overhead lines due to lightnings. It is of primary importance to disconnect the fault branch without interrupt the power transmission in all the associated stations of the HVDC network (by the opening of their respective AC circuit breakers). For the purpose of disconnecting the fault branch mainly three ways are possible:

1. Limiting the fault current by a proper design of the arm reactors and turning off all AC switches. This method is currently the standard for DC fault protection in HVDC network for its reliability but has the drawback of stopping the power transmission in the entire network.
2. Limiting the fault current by fast-tripping of DC circuit breakers. For physical reasons the interruption of a DC current of about few kA is not an easy task; the mechanical circuit breakers require a forced arc extinction and high energy adsorption. The utilization of electronic switches to interrupt the DC fault current would be beneficial in term of switching time but unfeasible from an economical point of view.
3. Limiting the fault current by the fast action of the MMC, electronically.

With regard to the third way, for what already said the HB topology is not able to suppress the fault current, whereas the FB topology is a proper candidate for this purpose. Indeed, it can quickly cut off arms current of any direction applying at the arm terminals an opposite polarity with respect to the current direction. This action can be done, in the simple manner, by turning off all the IGBTs of the arm; in this way the current flows in the freewheeling diodes and rapidly expires by recharging the submodule capacitors.

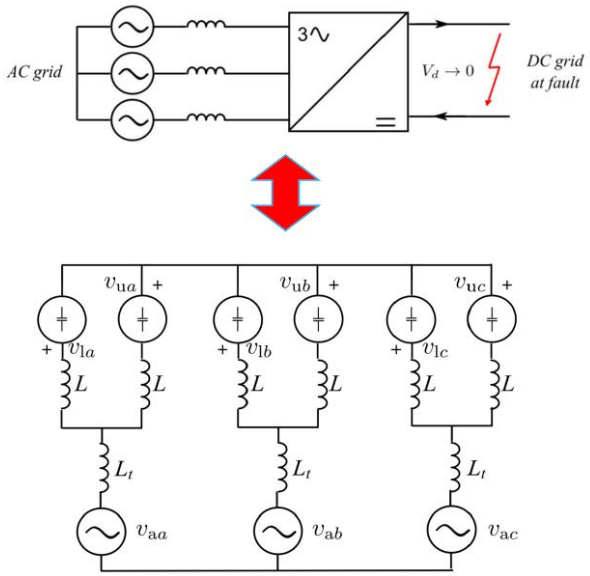

Fig. 5.7. Impact of DC short circuit on a HB based MMC: the DC short-circuit is seen as a symmetrical fault [36].

5.6 Control of MMC

5.6.1 Averaged Model and Ideal Insertion Indices

To preserve a charge balance between the upper and lower arms is required that the total capacitor voltage of the two arms is equal, i.e. $v_{cu}^{\Sigma} = v_{cl}^{\Sigma} = v_c^{\Sigma}$. A common criterion [25] is to select the mean total capacitor voltage equal to the DC pole to pole voltage, i.e.:

$$\overline{v_c^{\Sigma}} = V_d \tag{5.16}$$

The choice is made to preserve a constant circulating current even if the magnitude of AC voltage applied by the converter is maximum. Indeed, from the first of Eq. 5.8, it follows that for a HB MMC the maximum and minimum AC voltage is obtained respectively for:

$$V_l = V_c^{\Sigma};\ V_u = 0 \quad \text{and} \quad V_l = 0; V_u = V_c^{\Sigma} \tag{5.17}$$

To maintain the DC voltage (equal to the sum of the arm voltages, see Eq. 5.3) at the required level (V_d) also when the AC voltage magnitude is maximum, it must be satisfied Eq. 5.16. Then, from the second relation of Eq. 5.9 it follows that, in this way, $v_c \cong \frac{V_d}{2}$ and therefore i_c can be controlled to a constant value. Moreover, for the HB MMC this choice permits to maximize the magnitude of the AC voltage synthetized, given the magnitude of the DC voltage to impose, see Fig. 5.5. Note that even for the FB topology Eq. 5.16 is a typical

choice and that a constant circulating current is desirable to keep the RMS arm current and thus the converter losses at a minimum.

The total capacitor voltage should be equally distributed among the arm submodules, such that the mean SM capacitor voltage is:

$$\overline{V_c} = \frac{\overline{v_{cu,l}^{\Sigma}}}{N} \tag{5.18}$$

For the purpose of obtaining a dynamic model of relatively simplicity it is convenient to consider the average voltage applied by each arm as function of the mean insertion index, i.e.:

$$n_{u,l} = \frac{1}{N}\sum_{i=1}^{N} n_{u,l}^{i} \tag{5.19}$$

Where $n_{u,l}^{i}$ is the state of the i-th submodules and N the total number of submodule per arm. Thus, the average voltage applied by the arm can be expressed as a function of the mean insertion index and the total capacitor voltage, as:

$$v_{u,l} = n_{u,l} v_{u,l}^{\Sigma} \tag{5.20}$$

Substituting Eq. 5.17 in the previously derived dynamic model for the currents yield the following averaged model for the currents:

$$\frac{L}{2}\frac{di_s}{dt} = \frac{n_l v_{cl}^{\Sigma} - n_u v_{cu}^{\Sigma}}{2} - v_a - \frac{R}{2} i_s \quad L\frac{dic}{dt} = \frac{V_d}{2} - \frac{n_l v_{cl}^{\Sigma} + n_u v_{cu}^{\Sigma}}{2} - R i_c \tag{5.21}$$

The averaging principle can be easily extended to the capacitor voltages [25], obtaining the following relations which complete the averaged model:

$$\frac{C}{N}\frac{dv_{cu}^{\Sigma}}{dt} = n_u\left(\frac{i_s}{2} + i_c\right) \qquad \frac{C}{N}\frac{dv_{cl}^{\Sigma}}{dt} = n_l\left(-\frac{i_s}{2} + i_c\right) \tag{5.22}$$

Note that the number of state variables (inductor currents and capacitor voltages) per phase has now been reduced to four ($i_s, i_c, v_{cu}^{\Sigma}, v_{cl}^{\Sigma}$) instead of 2(N+1). Moreover, the more submodules are used, the more voltage levels can be obtained and consequently $n_{u,l}$ and $v_{u,l}$ can be considered as continuous variables; assuming that they continuously vary means to disregard the harmonic content of the output voltage, due to the switching process of the converter.

Supposing that the references for the output (v_s*) and internal voltage (v_c*) are defined, combining Eq. 5.8 with Eq. 5.20 gives the ideal insertion indices, i.e. the number of submodules that must be inserted at any time to follow the prescribed references:

$$n_u = \frac{v_c^* - v_s^*}{v_{cu}^{\Sigma}} \quad n_l = \frac{v_c^* + v_s^*}{v_{cl}^{\Sigma}} \tag{5.23}$$

In the following section it will be analysed how to generate the proper references for v_c^* and v_s^*, in order to respectively control the differential and circulating current by the insertion indices. Since the output currents are sinusoidal and the circulating current should be pure DC, then observing Eq. 5.6 and Eq. 5.18 it follows that v_s should be sinusoidal whereas v_c constant and approximatively equal to $v_d/2$ to obtain i_c to be pure DC.

As it will be addressed in Section 5.6.4.1 the ideal insertion indices, described by Eq.5.23, can be used as they stand or can be slightly modified to guarantee voltage balancing between the arms.

5.6.2 Differential Current Control (DCC)

The differential current is governed by the first relation in Eq. 5.6, here reported for convenience:

$$\frac{L}{2}\frac{di_s}{dt} = v_s - v_a - \frac{R}{2}i_s \tag{5.24}$$

Usually the current control for three-phase converters is performed in the *dqo* rotating reference frame, by the application of the *Park transformation.* The main reason to move in a reference frame rotating at the fundamental pulsation is to make sinusoidal varying signals to be pure DC and thus obtaining a zero steady state error with a simple Proportional Integrator (PI) controller. Moreover, in a *dq* frame aligned with the ac-bus voltage the d and q ac current components are respectively proportional to the input active and reactive power respectively. The *dqo* or Park transformation can be realized by the following relationship, which preserve the signals magnitude between the two systems:

$$\begin{Bmatrix} u_d \\ u_q \\ u_0 \end{Bmatrix} = \frac{2}{3}\begin{bmatrix} \cos(w_1 t) & \cos\left(w_1 t - \frac{2}{3}\pi\right) & \cos\left(w_1 t + \frac{2}{3}\pi\right) \\ -\sin(w_1 t) & -\sin\left(w_1 t - \frac{2}{3}\pi\right) & -\sin\left(w_1 t + \frac{2}{3}\pi\right) \\ 0.5 & 0.5 & 0.5 \end{bmatrix}\begin{Bmatrix} u_a \\ u_b \\ u_c \end{Bmatrix} \tag{5.25}$$

Where u_a, u_b, u_c are the three phase quantities, w_1 represents the *dq* frame rotating speed and u_d, u_q and u_0 respectively the direct, quadrature and zero sequence component. Applying the Park transformation of Eq. 5.25 to the phase relations for the differential current dynamics (Eq. 5.24) and assuming the system devoid of zero sequence component, yields to the following equations for the control of direct (i_d) and quadrature (i_q) currents:

$$L\frac{di_d}{dt} = v_d - v_{a,d} + \frac{w_1 L}{2}i_q - \frac{R}{2}i_d \tag{5.26}$$

$$L\frac{di_q}{dt} = v_q - v_{a,q} - \frac{w_1 L}{2}i_d - \frac{R}{2}i_q \tag{5.27}$$

In these last two equations it can be seen a cross coupling term between the d and q axes, which can be eliminated by an inner feedback loop, realizing the so called *dq* decoupling. The d and q voltage references must be sensitive respectively to the direct and quadrature current errors and can be generated from a PI controller with zero static tracking error of the current reference. The decoupling term and eventually the feedback of the voltage grid are added after the controller output. In formulae the voltage references are:

$$v_d^* = \left(k_P + \frac{k_I}{s}\right) * (i_d^* - i_d) + v_{a,d} - \frac{w_1 L}{2}i_q \tag{5.28}$$

$$v_q^* = \left(k_P + \frac{k_I}{s}\right) * (i_q^* - i_q) + v_{a,q} + \frac{w_1 L}{2}i_d \tag{5.29}$$

Where the proportional and integral gain have the dimensions of [V/A]. If the *dq* rotating frame is aligned with phase a of the grid voltage then $v_{a,q}$, i.e. the quadrature component of the grid voltage, is zero. In Fig. 5.8 are shown the direct and quadrature current control loops realized in Matlab-Simulink [26] which will be used for the numerical model explained in Section 7. The d and q voltage reference are then reported to the *abc* reference, obtaining the output voltage reference v_s^* for each phase.

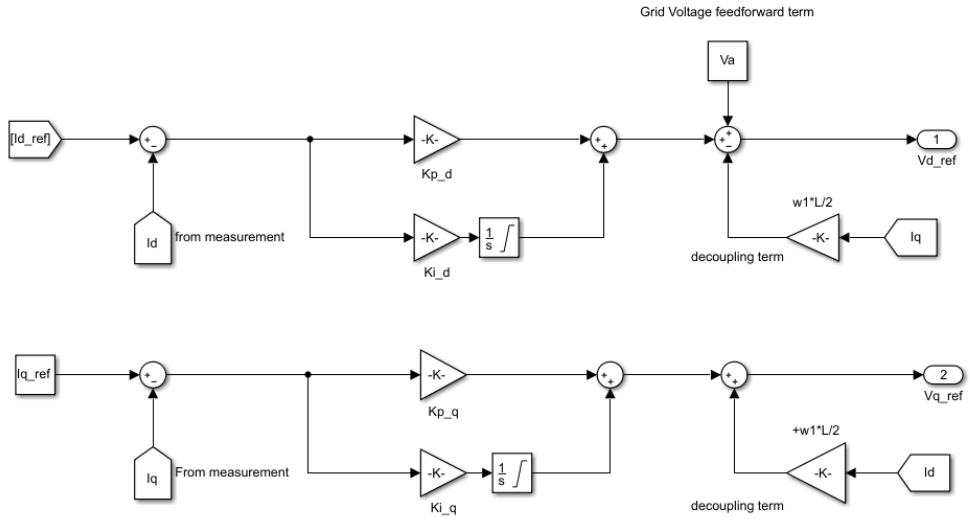

Fig. 5.8 Direct and quadrature current control loops realized in Simulink.

5.6.3 DC-Bus Voltage Control (DCVC)

To correctly regulate the DC-Bus Voltage a proper DC-bus dynamic model, considering not only the pole to pole DC capacitance (C_d) but also the submodule capacitors, has to be derived. In [27] the submodule capacitors have been included in the analysis yielding the following DC-Bus dynamic relation:

$$\left(C_d + \frac{2MC}{N}\right)\frac{dV_d}{dt} = I_d - \frac{P}{V_d} \tag{5.30}$$

Where M is the number of phases, V_d and I_d the DC voltage and current, P is the active power exchanged with the AC network and the unbraced expression represents the effective DC-bus capacitance (C_d') , taking into account the submodule capacitance (C) and the pole to pole capacitance (Cd):

$$C_d' = C_d + \frac{2MC}{N} \tag{5.31}$$

It is possible to define the DC-bus capacitance energy, i.e. the overall energy stored in the converter capacitors, as:

$$W_d = \frac{1}{2}C_d' V_d^2 \tag{5.32}$$

Considering the expression of the DC-Bus capacitance energy (Eq.5.31), and multiplying Eq. 5.30 by V_d yields:

$$\frac{dW_d}{dt} = V_d I_d - P \tag{5.33}$$

This equation represents the DC-bus energy dynamics: the DC-bus energy is maintained constant (i.e. the DC voltage is maintained constant) when the power at the DC side ($V_d I_d$) is equal to the power at the AC side (P) of the converter. Any imbalances between the two terms of power imply a DC-bus energy variation (a DC voltage variation). For instance, if during a load transient the power entering in the converter at the AC side is less than the power required by the load at the DC side, then the remaining power is supplied by the DC-bus; the energy stored in the capacitors of the converter supply the load in the transient, and thus the DC voltage diminishes.

The DC-bus Voltage Control must be sensitive to the DC-bus energy error (ΔW_d), i.e. to the difference between the DC-Bus energy reference (corresponding to the DC voltage reference V_d^*) and the actual DC-Bus energy (corresponding to the measured DC voltage V_d) and must act on the AC power reference (P^*) in order to compensate the energy error. For example, if the DC voltage is less than the DC voltage reference the DVC must increase the active power setpoint in order to adsorb more power from the grid. Considering a PI controller in formulae we have:

$$P^* = \left(k_p + \frac{k_i}{s}\right) * \Delta W_d = \frac{1}{2} C_d' \left(V_d^2 - V_d^{*2}\right) * \left(k_p + \frac{K_i}{s}\right) \qquad 5.34$$

Where the controller gains k_p and k_i have the dimension of s^{-1}.

It is worth noting that synchronizing the *dq* reference frame with phase a of the AC voltage grid implies a great simplification because active and reactive power can be independently controlled by the direct and quadrature current component. Thus, a simple rescaling of the active power reference $P^*$is fed at the direct current regulator (see section 5.6.2) as a reference to control the DC-Bus voltage. Instead the q-current reference can be freely set to regulate the reactive power exchange. The relationships between direct (i_d^*) and quadrature (i_q^*) current references and active (P^*) and reactive (Q^*) power setpoints are, for a magnitude-invariant Park transformation:

$$i_d^* = \frac{2P^*}{3V_a} \qquad i_q^* = \frac{2Q^*}{3V_a} \qquad 5.35$$

In Fig. 5.9 a DVC loop, which will be used in the numerical model presented in section 7, is shown.

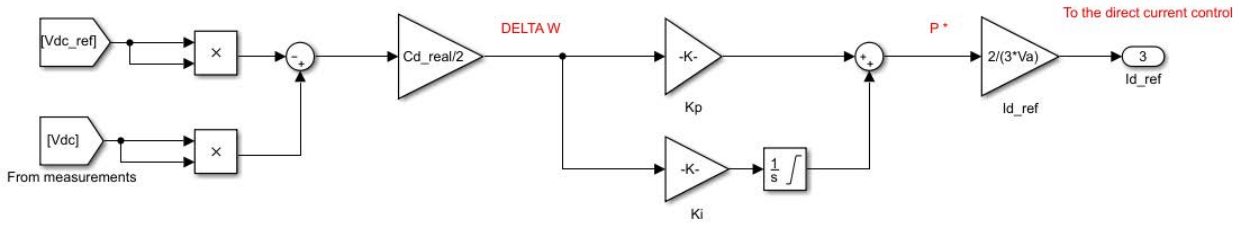

Fig. 5.9 DCVC loop realized in Matlab-Simulink.

5.6.4 Internal control (Arm balancing)

The remaining state variables to be controlled are $i_c, v_{cu}^{\Sigma}, v_{cl}^{\Sigma}$ which evolve accordingly to the second relation in Eq. 5.21 and to Eq. 5.22, here reported for convenience:

$$\frac{Ldi_c}{dt} = \frac{V_d}{2} - \frac{n_u v_{cu}^{\Sigma} + n_l v_{cl}^{\Sigma}}{2} - Ri_c \qquad 5.36$$

$$\frac{C}{N}\frac{dv_{cu}}{dt} = n_u(i_s + i_c) \qquad \frac{C}{N}\frac{dv_{cl}}{dt} = n_l\left(-\frac{is}{2} + i_c\right) \qquad 5.37$$

The control objectives are the followings:

- Maintain the circulating current i_c at a constant value, i.e. equal to 1/3 of the DC current. This task refer to the Circulating Current Control (CCC).
- Maintain the v_{cu}^{Σ} and v_{cl}^{Σ} constant and equal to their nominal mean value V_d (see Eq. 5.14). These tasks refer to the Arm-Voltage Control (AVC).

The input variables available for manipulations are two, that is the insertion indices n_u and n_l, whereas the state variables to be controlled are three. Besides only the circulating current is available for transferring the energy between the arms, indeed the AC current shall be controlled to track its reference independently of the converter internal dynamics [25].

To achieve the arm voltage balancing the ideal insertion indices (see Section 5.6.1) must be to some extent modified; there are several AVC strategies and here only two of them will be addressed. Chosen the AVC strategy the Circulating Current Control (CCC) shall be adapted to the first one.

5.6.4.1 Arm Voltage Control

As previously said two schemes available for the AVG will now be outlined, and the different implications of the schemes on the output and internal voltage will be considered. The modification of the ideal insertion indices for this purpose comprises only the denominator of Eq. 5.23. The presented schemes are:

- Direct Voltage Control (Direct Modulation)
  The ideal insertion indices of Eq. 5.20 are modified in the following way:

$$n_u = \frac{v_c^* - v_s^*}{V_d} \quad n_l = \frac{v_c^* + v_s^*}{V_d} \qquad 5.38$$

  In practice, the instantaneous sum capacitor voltages are substituted with their nominal mean value. It has been demonstrated [25] that this selection of the insertion indices gives an asymptotically stable system, besides it is simple and require low computational efforts. Negative aspect is the comparison of fluctuations at twice the fundamental frequency in the circulating currents and internal voltages. A detailed study of steady-state circulating current has been given in [28].

- Closed-loop voltage control
  The ideal insertion indices of Eq. 5.20 are used as they stand. The resulting system is marginally stable because the circulating currents are no more related to the sum capacitor voltages; two additional arm-energy controllers are needed to control the arm voltage and obtain an asymptotically stable system. The system complexity is not only increased for the addition of two closed-loop controls but also for the need to measure each individual capacitor voltage to form the sum capacitor voltage which must be feedback controlled. However, with this solution, no parasitic components appear on the output and internal voltages. The additional arm energy controllers described in [27] control the arm capacitor voltage via the total and imbalance arm energy, which respectively account for the

total energy stored in the two arms of the leg and for the difference between the upper and lower arm.

5.6.4.2 Circulating Current Control (CCC)

The Circulating Current Control (CCC) is inherently linked to the arm voltage control, indeed, the circulating current must be to some extent adapted to suit the AVC scheme that has been chosen. Generally, it is sufficient to maintain the circulating currents in the three phase legs at a constant value to avoid unbalances between the arm energy and thus between the arm voltages. This reference value (i_c^*) is therefore equal to 1/3 of the DC current, which is constant at steady state conditions. It is reported here for convenience the equation governing the dynamic of the circulating currents.

$$L\frac{dic}{dt} = \frac{V_d}{2} - v_c - Ri_c \qquad 5.39$$

Given that the voltage drop due to the arm resistance (R) is small, it can be observed that the internal voltage reference v_c^* shall be approximatively equal to $V_d/2$ in steady state conditions to obtain a constant circulating current. The DC voltage can be feedforwarded in order to improve the dynamic performances, together with the resistive voltage drop. Generally, it is sufficient a proportional control to increase the damping from (R/L) to (R+Ra)/L with the result of provide a near constant circulating current. The proportional gain is denoted with Ra because acts as a virtual resistance.

For an Arm Voltage Control (AVC) adopting the Direct Voltage Control (DVC) scheme the CCC must include a resonant part in order to suppress the second harmonic components that appear in the circulating currents due to the DVC scheme used.

A block diagram of the per-phase CCC is shown in Fig. 5.10; as it can be seen there is a resonant part tuned at $w_2 = 2\pi * (100) rad/s$, thus this CCC scheme is suited to suppress the harmonic components at twice the fundamental frequency due to the DVC scheme.

For an Arm Voltage Control (AVC) adopting the Closed-loop voltage control there is no need for a resonant controller, but the circulating current reference must take into account the state of the total and imbalance arm energy [27].

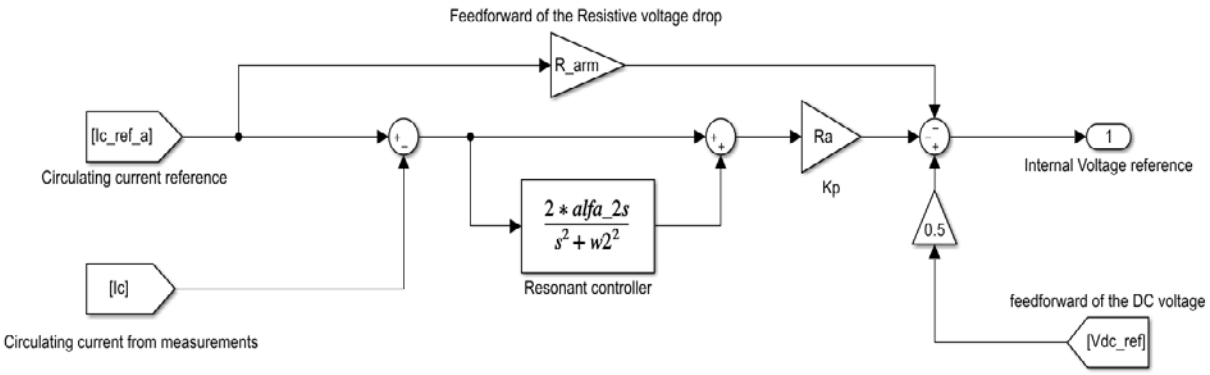

Fig. 5.10 Per phase Circulating Current Controller implemented in Matlab-Simulink.

5.7 Modulation and Submodule energy balancing

The Modulation and SubModule (SM) energy balancing stage receive as inputs the insertion indices n_u and n_l from the control stage of the MMC and must assign the right state to each SM by assuring two objectives:

1. The reference voltage for the submodule strings shall be, to a sufficient extent, approximated by the multilevel voltage waveforms. This task belongs to the Modulation stage.
2. The individual capacitor voltages shall not deviate far from the average due to the switching process; this task is solved by the SM Energy Balancing.

Both of these objectives are accomplished by inserting (n=1), bypassing (n=0) or counter-inserting (n=-1) the submodules at appropriate instants. There are mainly two approaches to address these requirements: decoupling the modulation stage from the submodule energy balancing or trying to directly assign the state of the cell assuring inherently balancing. In the next the PWM schemes for MMC will be briefly explained, highlighting those who assign the SM states guaranteeing an equal energy repartition. Then the principle of Nearest Level Control (NLC) which decouples the two functions will be given.

5.7.1 Multilevel carrier-based modulation

In 2-level PWM schemes the switching instants are determined by the comparison between a carrier wave (typically triangular) at high frequency with a reference at low frequency. Normally the carrier frequency, which determines the switching frequency of the Power Semiconductors (PSs), is chosen as a trade-off between harmonic performances and switching losses. In a MMC with hundreds of SMs the harmonic distortion could be not decisive in the selection of the carrier switching frequency but must be carefully chosen in order to assure an equal distribution of the PS losses and to carry out the task of energy balancing.

Generally, for N submodules there are N carriers, each assigned to one of the SM; each SM works exactly in the same way as a 2-level PWM scheme does. The output multilevel waveform is the sum of N two-level waveforms and the number of voltage levels depends on the way of arranging the SM carriers.

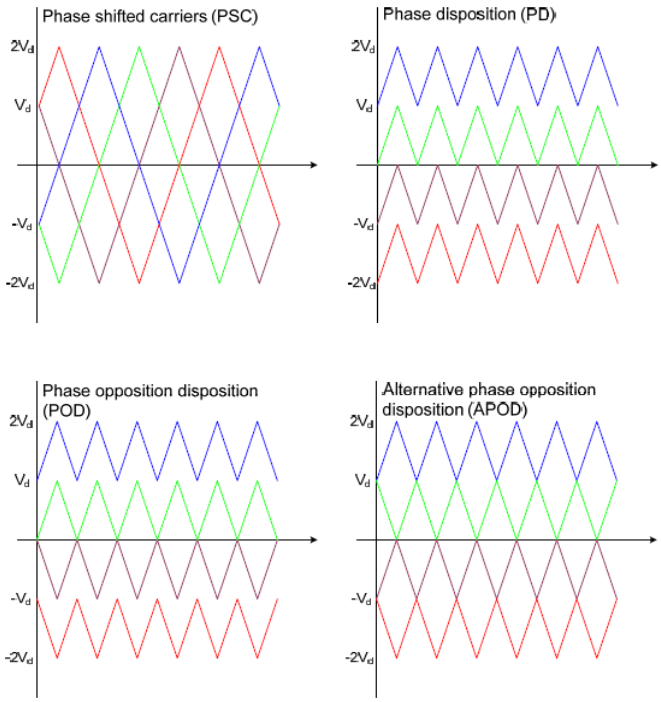

Fig. 5.11 Multilevel Carrier disposition: PSC in the top-left, PD in the top-right, POD in the bottom left and APOD in the bottom right. [36]

There are mainly two ways of arranging the SM carriers: Phase Shifted (PS) Carriers and Phase Disposition (PD) Carriers; the various disposition are graphically shown in Fig. 5.10 where POD and APOD are two variants of the PD carriers.

It is important to note that all the PD variants produce switching patterns that are not equally distributed and differ slightly among the SMs; this causes uneven switching losses and loadings of the SM capacitors. In addition, there is no way to achieve voltage balancing with this type of configuration.

The PS carrier configuration, instead, offers inherently an equal distribution of loading and power losses (the switching pattern are the same, only time shifted). Besides it has been analytically demonstrated [29] that with a non-integer ratio between the carrier frequency and the fundamental frequency is it possible to achieve balancing for capacitor voltages over time. Some considerations regarding the PS carriers will be addressed.

Given N submodules per arm, and a switching frequency of each submodule f_{sw} (equal to the carrier frequency), then the equivalent switching frequency of the output voltage is:

$$f_{eq} = 2Nf_{sw} \tag{5.40}$$

The angular displacement between the carriers of the same arm can be chosen as:

$$\Delta\vartheta_{i,i+1} = \frac{2\pi}{N} \tag{5.41}$$

The angular displacement between the carriers in lower and upper arms can be chosen in order to minimize the harmonic content either on the DC side or on the AC side [29], giving rise to two different modulation strategies:

- (N+1) Level Modulation
  In order to minimize the harmonic distortion in the DC voltage, the angular displacement between the upper and lower carrier waveforms must be:

  $$\beta = \pi \tag{5.42}$$

  It is called N+1-level modulation because N+1 is the number of voltage levels that can be obtained with this modulation strategy.
- (2N+1) Level Modulation
  To enhance the harmonic performances at the AC side the angular displacement between the upper and lower carrier waveforms must be:

  $$\beta = 0 \quad if \quad N\ odd \tag{5.43}$$

  $$\beta = \frac{\pi}{N} \quad if \quad N\ even \tag{5.44}$$

  With this modulation strategy the number of voltage levels of the AC voltage is (2N+1).

5.7.2 Nearest Level Control (NLC)

The NLC, also known as Staircase modulation, is well suited for MMC with hundreds of SMs per arm. Indeed the basic function is to sample the voltage reference at high frequency and then approximate it by the nearest voltage available. The more voltage levels are available and the more accurate the approach is; for this reason and for its simplicity it is can be also applied to MMC-HVDC. The simple algorithm implementing the strategy is:

$$round(x) = \begin{cases} floor(x) & if\ \ x < floor(x) + 0.5 \\ ceil(x) & if\ x \geq floor(x) + 0.5 \end{cases} \quad 5.45$$

This method, however, does not select which submodule to insert or bypass, but only how many must be inserted in each arm. For this reason, it is required a sorting algorithm which can be thought in order to provide voltage balancing at the SM level.

The basic idea for a simple voltage balancing strategy is the following:

1. Measure all the arm submodule capacitor voltages
2. Measure the arm current (i.e. positive current charges the capacitors)
3. Compare the SM voltages to find which are more charged and which less.
4. On the basis of the number of cells to be inserted (from the modulation stage) decide to insert the ones with lower voltages if the arm current is positive or the ones with higher voltages if the current is negative.

6 Preliminary design of MMC system for DEMO NBI AGPS

6.1 Introduction

For the benefits in terms of efficiency, controllability and modularity, and the possibility to raise very high voltage thanks to the series connection of hundreds of SubModule (SM) the MMC topology could be a good alternative to the actual Neutral Beam Injector (NBI) Acceleration Grid Power Supply (AGPS) system, described in Section 4. In order to evaluate the effective possibility of applying the MMC topology to the NBI AGPS, a preliminary design of the converter is carried out. The NBI specifications are those reported in Table 3.2 for the DEMO NBI current design; the beam current is not yet defined thus it is assumed the same as the ITER beam current. The main specifications are thus:

- Acceleration Voltage: 1 MeV
- Beam Current: 40 A

The choice of the main circuit parameters will be carried on in the following sections, trying to outline a MMC preliminary design aimed at fulfilling the main AGPS requirements described in Sections 4.3.1 and 4.3.2. The design currently being developed [15] for the DEMO NBI foresees 5 acceleration stages to reach a total voltage of 1 MV. In the following it is considered for the MMC preliminary design only a single stage of acceleration and, thanks to the modularity structure of the converter, the other stages may be designed in the same way. Thus, similarly to the AGPS-CS stages of MITICA and ITER NBIs, the requirements in terms of output voltage and current ratings for the MMC are:

- V_{DC}=200 kV
- I_{DC}=60 A

The choice of the main circuit parameters will be now addressed, considering the different operating conditions and requirements. The correct determination of the circuit parameters is not straightforward and the values that will be obtained must be verified by simulation (Section 7) and adjusted if necessary.

6.2 Choice of the Submodule Topology

The main SubModule (SM) topologies are the Half Bridge (HB) and Full-Bridge (FB) ones, described in Section 5.2, even if other topologies derived by these two are under study. The main difference between the two is that only FB MMC can provide a bipolar DC voltage, with the capability to handle DC faults without the tripping of AC or DC circuit breaker, as explained in Section 5.5. Considering that frequent breakdowns (BDs) are expected to occur between the accelerating grids, and that the system must be able to quickly suppress the fault current and restart in few milliseconds, the FB SM topology has been chosen as the fundamental block of the MMC. In Fig. 6.1 it is reported the schematic of a FB submodule.

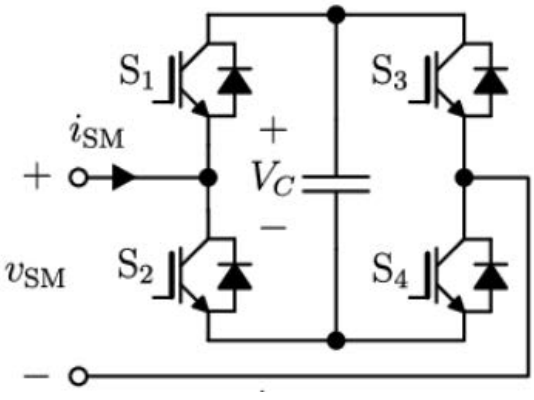

Figure 6.1. Full Bridge Submodule.

6.3 Choice of Power Semiconductor Devices

The starting point for the choice of Power Semiconductor (PS) device is the peak value of the arm current at rated operation. From Eq. 5.12 the maximum current (I_{rated}) to be handled by the PS device is:

$$I_{rated} = \frac{I_{DC,rated}}{3} + \frac{\hat{I}_{s,rated}}{2} \tag{6.1}$$

Where $I_{DC,rated}$ is the DC current at nominal operating conditions (i.e. 60 A) and $\hat{I}_{s,rated}$ is the peak value of the AC side current at rated operation. This last can be estimated by Eq. 5.10, here rearranged for convenience:

$$\hat{I}_s = \frac{4I_d}{3m_a cos\varphi} \tag{6.2}$$

The maximum AC current depends on the operative conditions, i.e. the power factor and the modulation index, and some considerations on them must be made. As already outlined in Section 5.6 the converter can control the active and reactive power flow, thus the power factor can be set to zero in any working conditions. The modulation index, instead, varies during the operation, although at any condition it must be high enough to provide an AC voltage greater than the AC voltage grid, in order to correctly impose the AC current reference. Given the rated AC voltage of the converter it has been assumed a margin of 12.5% on the AC voltage grid in order to have a certain margin in the AC current control also in other conditions. Therefore, the modulation index cannot fall below 0.875, otherwise the AC voltage grid becomes greater than the AC voltage imposed by the converter, and the current control is lost. Thus, a realistic evaluation of the peak AC current is 91.4 A and the maximum current to be handled by the device in rated operation is about 65 A. However, the relation of Eq. 6.2 considers an ideal power flow (see Eq. 5.8) where losses are not taken into account and the AC differential current will be higher than estimated. To make a comparison, the typical current handled by PSs in HVDC MMC applications are about some kA, much higher than these. Generally, in HVDC applications the PS devices are chose in order to minimize the conduction losses, since the switching frequency for each SM is very low, due to the high number of SMs. Besides, High Voltage (HV) devices are preferred to minimize the complexity of the system. For these reasons, an Integrated Gate Commutated Thyristor (IGCT) seems the best solution for HVDC applications because of its high voltage and current ratings and for the low ON-state voltage drop. For the AGPS of a NBI the current rating is totally different and an Insulated Gate Bipolar Transistor (IGBT) device is more adequate.

To take some margin with respect to the peak current estimated (about 65 A) and to minimize the number of submodules it has been selected a commercial IGBT module manufactured by ABB, which comprises the series of two IGBTs with their respective freewheeling diodes. Each IGBT is rated for 4.5 kV of maximum collector-emitter voltage and 150 A of rated DC current. The IGBT module series number is 5SNG 0150P450300 [30] and the main characteristics are reported in Table 6-1.

ABB Hi Pack IGBT Module 5SNG 0150P450300					
Parameter	Symbol	Conditions	min	max	unit
Collector-emmiter voltage	Vces			4500	V
DC collector current	Ic			150	A
Peak collector current	Icm			300	A
Junction operating temper.	Tvj_op		-50	125	°C
IGBT Thermal resistance junc.-case	Rth.jc.IGBT			0.062	K/W
DIODE Thermal resistance junc.-case	Rth.jc.DIODE			0.122	K/W
IGBT Thermal resistance case-heat sink	Rth.cs.IGBT			0.048	K/W
DIODE Thermal resistance case-heat sink	Rth.cs.DIODE			0.096	K/W

Table 6.1 IGBT module N. 5SNG 0150P45030 main properties.

6.4 Choice of the number of Submodules

This step could seem trivial, being known the nominal DC voltage of the converter and the voltage rating of the power semiconductor device, instead this choice involves at least two other design choices:

- The mean total capacitor voltage per arm, $\overline{v_{cu,l}^{\Sigma}}$;
- The mean submodule capacitor voltage, V_c

6.4.1 Mean total capacitor voltage per arm

As already discussed in Section 5.6.1 a typical choice is to select the mean capacitor voltage per arm equal to the DC pole to pole voltage, thus:

$$\overline{v_{cu,l}^{\Sigma}} = V_{DC} = 200\ kV \tag{6.3}$$

6.4.2 Mean submodule capacitor voltage

This choice must be made with particular attention to the reliability of the PS devices. A common way to express the reliability of a device is by the Failure In-Time (FIT) rate, which gives an estimation of how many failures are expected to occur in 10^9 operating hours. This parameter is strongly affected by the DC voltage applied to the PS device, and it can be only estimated on the basis of many years of experience and comparison between different devices; in Fig.6.2 it is reported the FIT rate dependence on the DC voltage for a 4.5 kV IGCT device [31]. A typical value of DC link voltage for a 4.5 kV device based from experience is 2.8 kV.

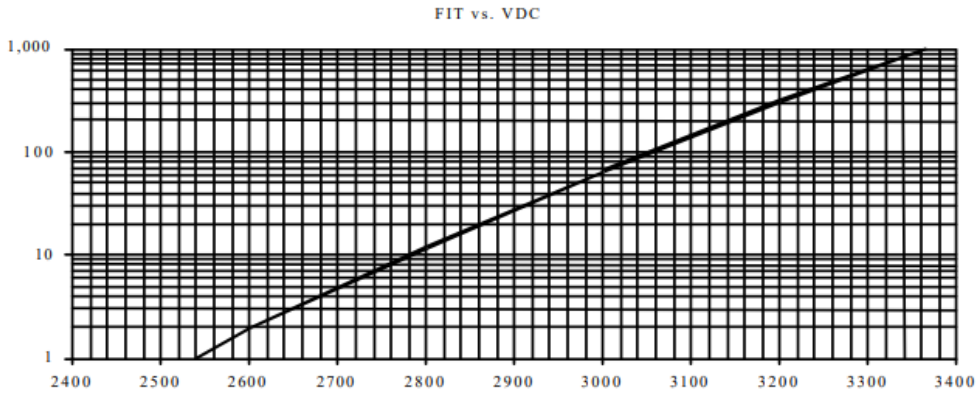

Fig. 6.2. FIT rate over DC voltage applied for an IGCT device.

However other factors should be taken into account, like the capacitor voltage ripple, the overvoltage due to the submodule stray inductance and the overvoltage due to loss of load (beam off in NBI applications). Considering some margin, due to the high number of IGBTs for a 200 kV application and the increasing probability of failure, it has been selected a mean capacitor voltage of:

$$V_c = 2\ kV \tag{6.4}$$

It is now possible to determine the required number of submodules per arm, resulting in:

$$N = \frac{\overline{v_{cu,l}^{\Sigma}}}{V_c} = 100 \tag{6.5}$$

Resulting in a total number of SMs, for the three converter legs, equal to:

$$N_{tot} = N \times 2 \times 3 = 600 \tag{6.6}$$

Where the factor 2 accounts for the two arms (lower and upper) and the factor 3 for the three phase legs.

6.5 Choice of the Submodule Capacitance

The choice of the Submodule capacity is delicate since a high submodule capacitance value has a drastic effect on the total cost of the MMC, whereas an insufficient value causes high voltage ripple and large voltage transients. There are mainly two criteria for the selection of the submodule capacitance:

- Limiting the capacitor voltage ripple;
- Limiting the voltage transient in case of rapid load variation.

For the AGPS of NBI are envisaged rapid load transients, e.g. due to the frequent occurrences of grid breakdowns and the consequent restart of the system. In particular the criterium adopted for the evaluation of the SM capacitance is to limit the voltage undershoot below the 15%, at the start-up at maximum voltage. This scenario, explained in Section 4.3.3., foresees a ramp-up of the current only when the voltage reaches the 100% of the rated value. Then it will be verified through simulations that the capacitor voltage fluctuations are acceptable and limited to about 10% of the mean capacitor voltage. A simple calculation can give a first tentative value for the SM capacitance; considering the DC voltage roughly constant to its nominal value in the beam current transient from zero up to its nominal value, the mean power to the load during the current ramp-up is about:

$$P_{mean} \cong \frac{1}{2} V_{DC} I_{DC} = 6\ MW \tag{6.7}$$

Then, assuming a transient duration of about 20 ms, the total energy which must be provided by the equivalent submodule capacity (see Eq. 5.31) is given by the product between the result of Eq. 6.7 with this time duration. It has been assumed that during this transient the AC grid gives no power contribution, since the dynamics of the power exchange with the AC network are limited by the grid frequency.

The equivalent capacitance of the converter, to limit the DC voltage undershoot at 10% of the rated value should be:

$$C_{eq} \cong \frac{2 * P_{mean} \Delta t}{V_{DC}^2 - (0.9 V_{DC})^2} = \frac{2 * 6[MW] * 20[ms]}{200^2[kV] - 180^2[kV]} \cong 31.5\ \mu F \tag{6.8}$$

Therefore, the SM capacitance can be calculated by Eq.5.31, neglecting the pole to pole capacitance, resulting in:

$$\mathrm{C_{SM}} = \frac{\mathrm{NC_{eq}}}{6} \cong 0.53\ \mathrm{mF} \tag{6.9}$$

For simplicity it has been taken 0.5 mF as a value for the SM capacitance in the simulations performed in Section 7. It will be verified through simulation if such a value could limit the voltage ripple to about 20% peak to peak and if the undershoots during load transition are acceptable.

6.6 Choice of Arm Inductances

The choice of the arm inductance is mainly linked to the fulfilment of two objectives:

- Limitation of the arm current at DC side short-circuits (i.e. grid breakdowns);
- Limitation of high-frequency components in the circulating currents.

For the first task the arm inductance value depends on the type of fault-handling strategy adopted. For example in the case of MMC based on HB submodule, with no short-circuit current suppression capability, the current circulates in the freewheeling diodes until the AC or DC circuit breaker open. During this time, about some tens of ms, the fault current can reach very high values with consequent damage of the devices.

In the case of a FB submodule equipped with IGBTs the short circuit current can be interrupted within a very short time, due to the rapid switch-off time of the electronic devices. Thus, the arm inductance must only limit the short-circuit current below the maximum interruptible current of the IGBTs. For the IGBT module selected in Section 6.3 the maximum peak current is of 300 A (see Table 6-1). Thus, considering a total IGBT switch-off time of 2.3 µs from the datasheet and assuming a detection time of 5 µs, the arm inductance must limit the rise of the arm current up to 300 A. Considering an arm current at the fault occurrence equal to peak value of 65 A previously calculated it follows that:

$$L_{arm} = \frac{0.5\, V_{DC}\, t_{delay}}{I_{max} - I_{arm}} = \frac{0.5 * 200\ [kV] * 7.3[\mu s]}{300 - 65\ [A]} \cong 3.1mH \qquad 6.10$$

For simplicity in the following it will be assumed L_{arm} equal to 3 mH.

6.7 Summary of the main circuit parameters

The results obtained from this preliminary design are reported in Table 6.2.

Parameter	Symbol	Value	Unit
IGBT rated voltage	V_{ces}	4.5	kV
IGBT rated current	I_{forw}	150	A
Total capacitor voltage per arm	$\overline{v_{cu,l}^{\Sigma}}$	200	kV
Mean capacitor voltage	V_c	2	kV
Number of SM per arm	N	100	
Total number of SM	N_{tot}	600	
Submodule capacitance	C	0.5	mF
Arm inductance	L_{arm}	3	mH

Table 6.2 Summary of the main circuit parameters of the MMC for NBI AGPS

7 Development of MMC numerical model for NBI application

7.1 Introduction and Simulation Parameters

In this section, a numerical model realized in MATLAB-Simulink [32] of the MMC for NBI AGPS is developed, in order to verify the feasibility of this kind of converter with the requirements of the application by numerical simulations. The main aim of these analyses is to verify the static and dynamic performances of an AGPS system based on MMC topology, and to compare the results with the requirements given in Section 4 and with the simulations performed on the MITICA AGPS [6].

The numerical model is a scale prototype of the MMC designed in Section 6, rated for:

- V_{DC}=8 kV
- I_{DC}=60 A

The voltage rating is reduced by a factor of 25, whereas the current rating is the same. The voltage rating of the developed model has been only limited by the computational cost and simulation time saving. The time-domain simulation of a MMC, indeed, has high computational cost, due to the high number of state variables which must be determined at each simulation step. The state variables, i.e. the current in the inductances and the voltage of the capacitors, for each phase leg are equal to:

$$n = 2N + 2 \tag{7.1}$$

Where the 2N term accounts for the number of submodule capacitors for phase leg and the term 2 accounts for the differential and circulating current flowing in the arm inductances. Since the number of submodule capacitors is proportional to the DC voltage rating (see Eq. 6.5) it follows that the system order (expressed by Eq.7.1) grows proportionally with the voltage rating.

The converter model parameters are the same of those listed in Table 6.2, except for the number of submodules, which is N=4 per arm and N_{tot}=24 in total.

The model is hierarchically organized in blocks and sub-blocks, as the modular structure of the converter allows. In the following each block will be described until the overall scheme will be shown. The control loops adopted have been essentially described in Section 5.6, for the Arm Voltage Balancing (AVG) it has been adopted the Direct Voltage Control (DVC) scheme. The adopted modulation technique is the PS carrier PWM with N+1-level, as described in Section 5.7.

Finally, the model will be used to perform numerical simulation in order to validate the parameters found in Section 6 and to verify the steady state and dynamics performances of the converter.

7.2 Simulink models

7.2.1 Model of the converter

The fundamental block of the converter is the submodule realized with a Full-Bridge topology, as decided in Section 6; in Fig. 7.1 is reported the shot of the Simulink model. The input-blocks (named INPUT 1 and INPUT 2) are the gate signals, generated at the modulation stage, which command the IGBT on-off switching. The block named “BD_Protection” is a Boolean signal, normally equal to one, which enters in the logical operator AND together with the gate signals. When a breakdown occur, the current exceeds the prefixed threshold and the protection is tripped: the status of the block “BD_protection” becomes 0 and all the IGBTs are switched off. The port named “Conn1” and “Conn2” are the connection ports that permit the connection between the SMs.

By connecting four of these SM in series it is formed the converter arm, shown in Fig. 7.2. Then, assembling together the upper and lower arm for each phase, it is formed the final MMC model, and in Fig. 7.3 a shot of the model is presented.

In Fig. 7.3 each of the “arm” block contains the series connection of 4 submodule as depicted in Fig. 7.2. Each of the submodule arm shown in Fig. 7.2 has the same structure as the single submodule in Fig. 7.1.

It can be seen from Fig. 7.3 that the grid is modelled by a three-phase ideal voltage source with a peak amplitude of 3.5 kV, which is less than the AC voltage applicable by the converter in the rated condition (4 kV) in order to have a certain margin in the AC current control.

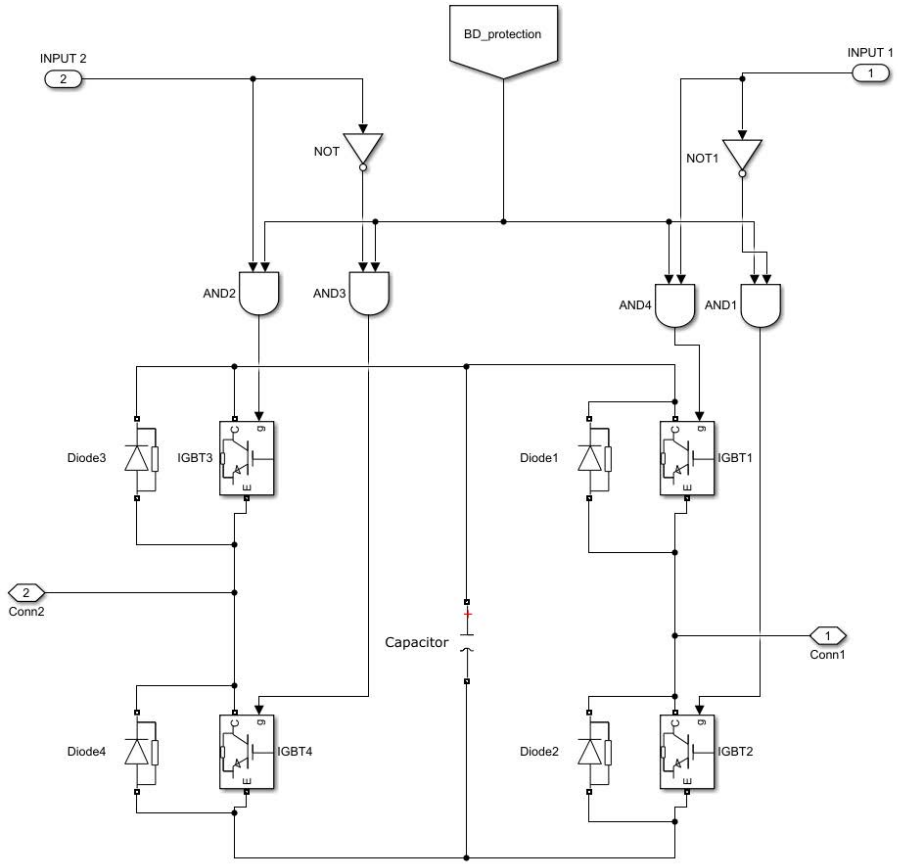

Fig. 7.1 Full Bridge Submodule Simulink model.

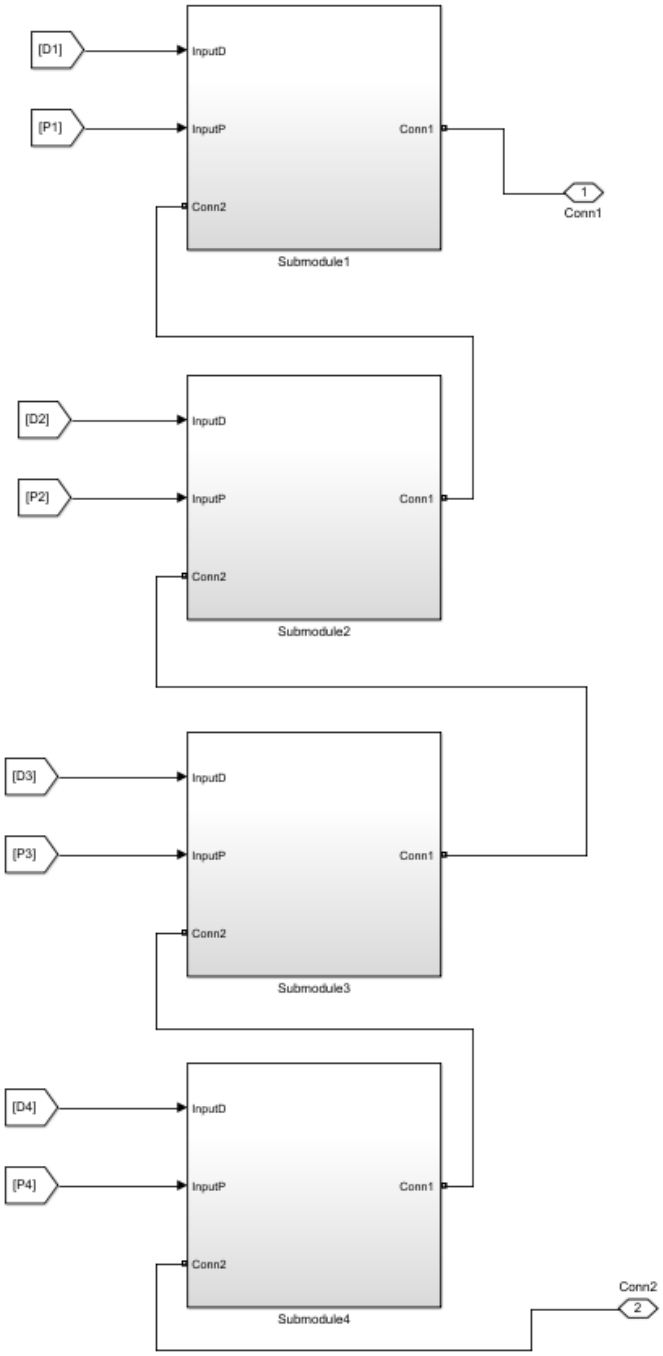

Fig. 7.2 Converter Arm Simulink model. The inputs of each blocks are the gating signals for the IGBT legs from the modulation stage.

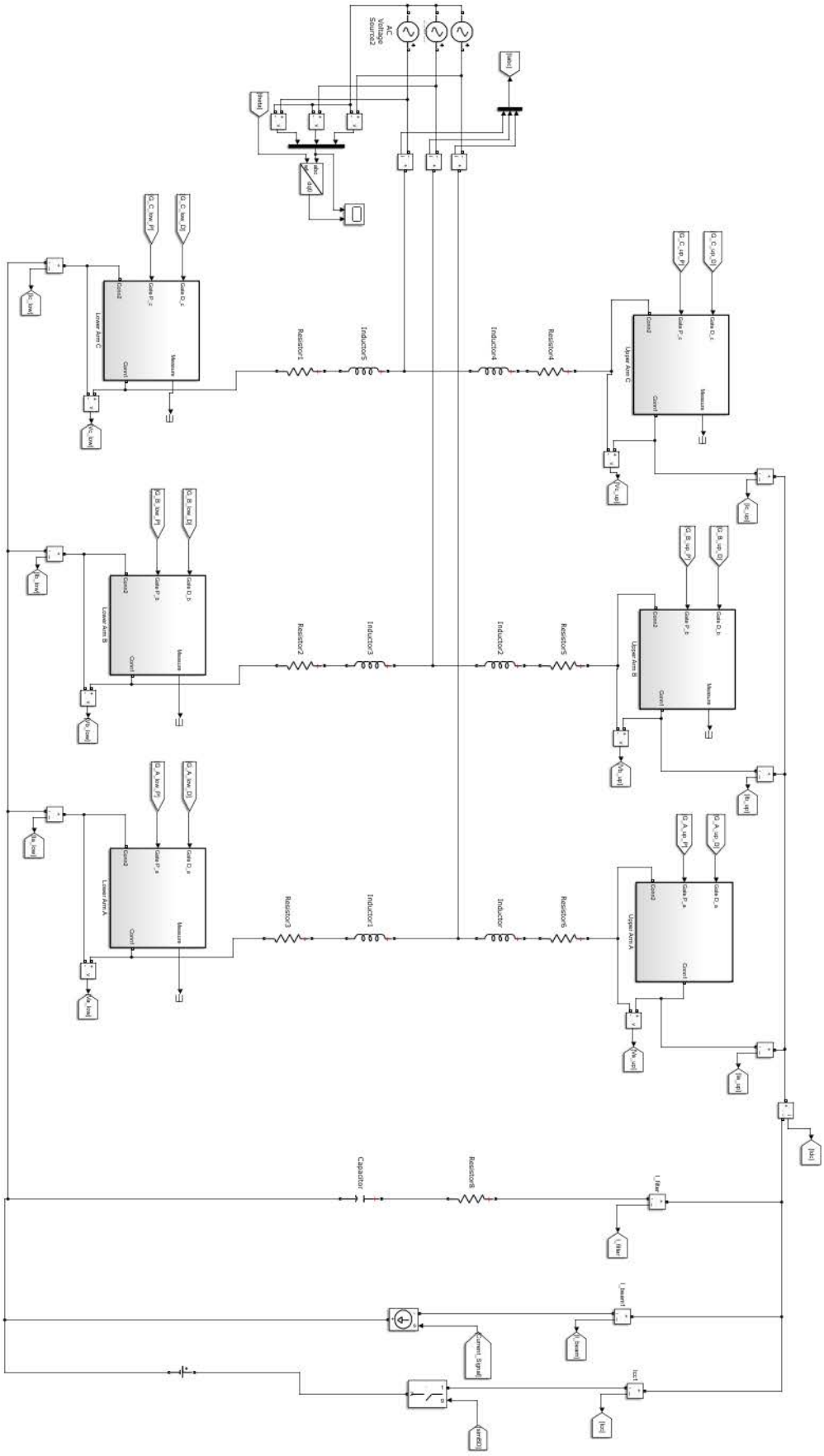

Fig. 7.3 Complete MMC Simulink Model.

7.2.2 Model of the load

The AGPS load is the NBI accelerator, and the current on each accelarating stage depends mainly on the power delivered by RF generators which produce the ions to be accelerated. The current is generally regulated in real time in order to achieve an accelerated beam current which should be function of the accelerating voltage, according to the perveance matching equation (Eq.3.1). Being the dynamics of the RF generators faster than those of AGPS, the load can be represented by ideal voltage controlled current generator as in Fig. 7.4, the current being a function of the instantaneous voltage in agreement with Eq. 3.1. The voltage is measured ant then passes through a Low Pass Filter (cut-off frequency 450 Hz) to dump the voltage ripple.

To simulate the grid BD the load can be short-circuited by an ideal switch, in series with a DC voltage generator (100 V) representing the arc voltage.

Moreover, the load is parallel connected to a DC filter composed by a capacitor (Cf) and a resistor (Rf) in series. The capacitor filter is needed to permit the inductance energy to discharge in case of beam-off (which corresponds to a loss of load for the MMC) and thus limiting the overvoltage below the 20% of the nominal value as reported in Section 4.3.5. The overvoltage at beam-off is mainly due to the currents in the inductances upstream the DC-bus but depends also on the converter switching-off time: the faster is the converter switching-off and the less is the energy discharged to the DC-bus from the AC side. The SM capacitors can instead be considered as ideal voltage source in the short transient of the beam-off, giving no contribution in the overvoltage limitation.

The resistor is added to limit the overcurrent from the DC filter to the grids in case of breakdown. The DC filter will be designed trough simulations.

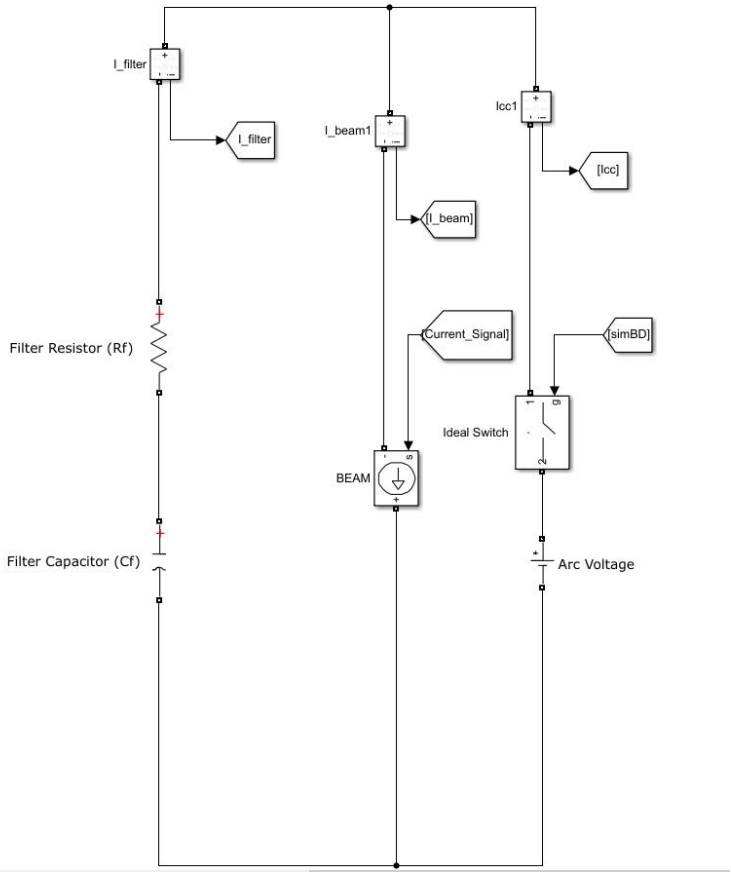

Fig. 7.4 Simulink model of the load.

7.3 Verification of steady state performances

7.3.1 Voltage ripple

The DC voltage and the beam current in steady state condition are reported in Fig. 7.5. As can be seen the DC voltage ripple with respect to the mean value is below the maximum voltage ripple (5% of the nominal value, i.e. 400 V for VDC=8 kV) required by the specifications (see Table 4.2).

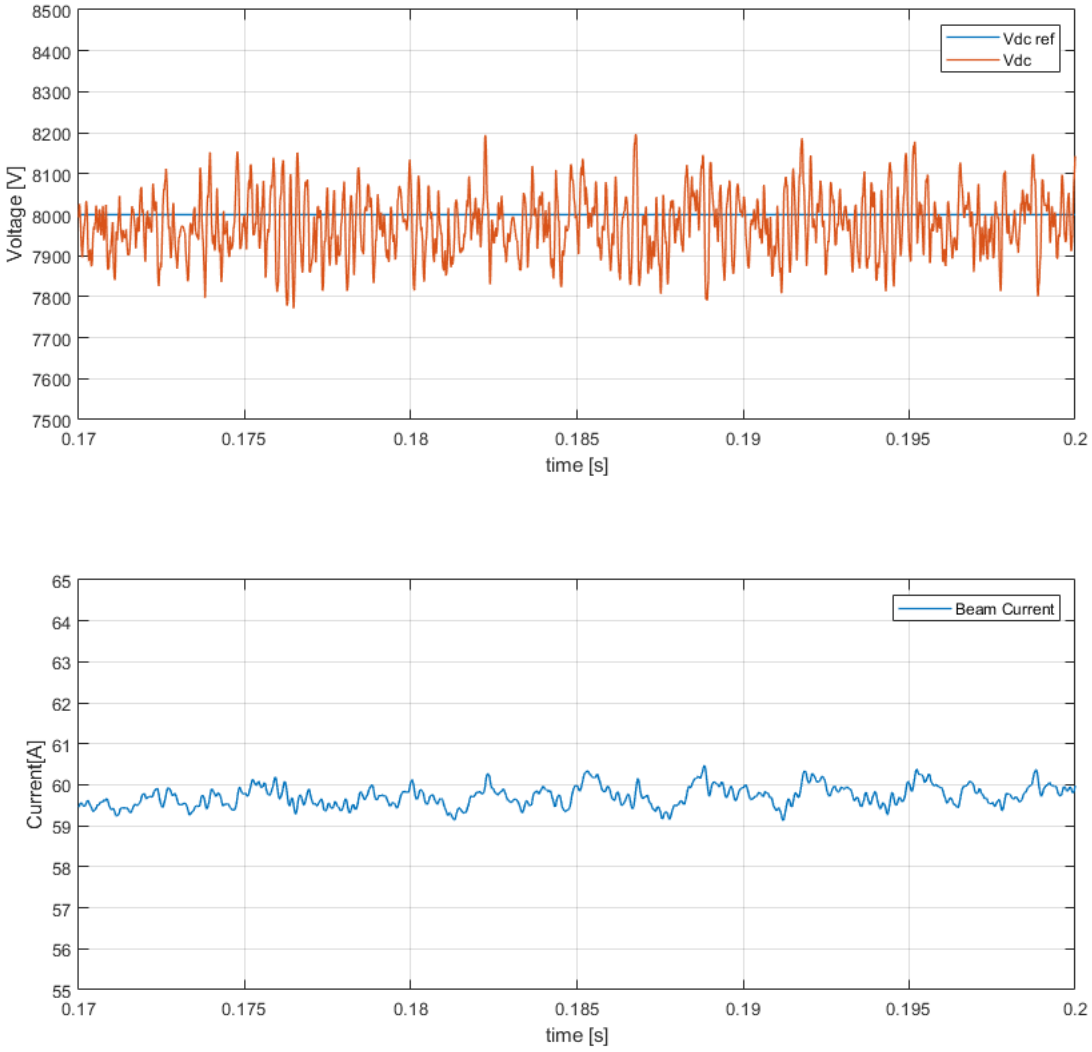

Fig. 7.5 Steady State output DC voltage and currents

7.3.2 Thermal analysis

At steady state conditions and at nominal DC voltage and current the semiconductor power losses have been calculated. The current waveforms in the power semiconductors at steady state conditions have been reported in Fig.7.6; it can be noted that the peak current is about 80 A which is well below the rated IGBT current (150 A) even if the estimation made in Section 6.3 is a bit underestimated.

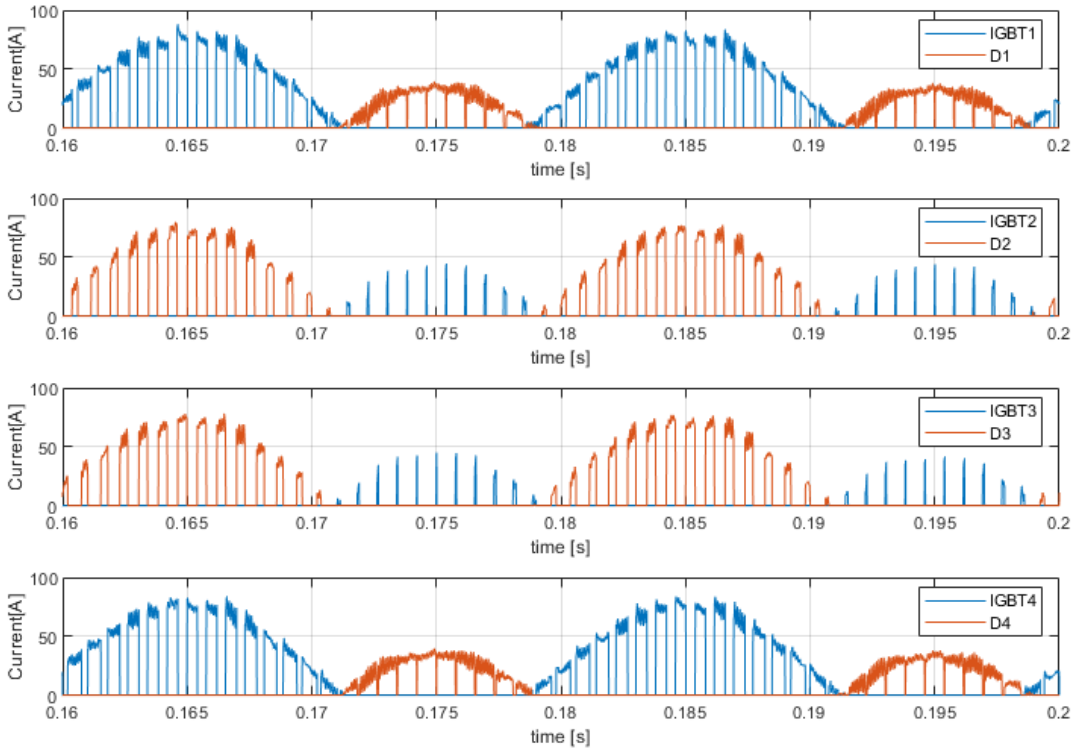

Fig. 7.6 Currents in the Power Semiconductor devices at steady state conditions and nominal operation.

The power dissipated in the IGBTs consists in two terms: conduction losses and switching losses. The first term can be approximately calculated by the product between the average semiconductor current with the correspondent forward voltage (available in the datasheet of the IGBT module). For the second term the manufacturer indicates in the datasheet a formula for the switching energies per pulse which considers both the ON and OFF energy dissipated. In formulae these two terms are:

$$P_{cond} \cong I_{avg} V_{forw.} \tag{7.2}$$

$$P_{sw} = f_{sw} E_{sw} = f_{sw}\left(8.5 * 10^{-6} * I_{avg}^2 + 5.6 * 10^{-3} * I_{avg} + 0.14\right) * \frac{V_c}{V_{cc}} \tag{7.3}$$

Where the unbraced relation is the formula given in the datasheet, f_{sw} is the switching frequency of each IGBT, V_{cc} is the external voltage applied in the OFF-state by the manufacturer and V_c is DC voltage effectively applied (mean capacitor voltage, 2 kV).

For the diode losses two terms must be taken into account: conduction losses and reverse recovery energy E_{RR} . The first term can be roughly calculated as before with Eq. 7.2, whereas the second one can be obtained by the datasheet as a function of the mean forward current, thus it is:

$$P_{RR} = f_{sw} E_{RR} \frac{Vcc}{Vc} \tag{7.4}$$

Note that having assumed the same equivalent switching frequency (10 kHz) between the real converter and the model, and with the arm inductance designed for the full-scale converter adopted in the model, the current ripple in the two systems should be the same, and the losses too.

To calculate the losses in the real system the switching frequency of each submodule (SM) must be reconsidered. Maintaining an equivalent switching frequency of 10 kHz the resulting SM switching frequency for the full converter is:

$$f_{SM_{real}} = \frac{f_{eq}}{2N_{tot}} = \frac{10000}{2 * 100} = 50\ Hz \tag{7.5}$$

Now, calculating the mean currents circulating in each power semiconductor device, it is possible to evaluate the semiconductor power losses for each submodule, by the application of Eq. 7.2, 7.3 and 7.4. The results of the calculations are reported in Table 7.1.

Parameter	Symbol	Unit	IGBT_1	IGBT_2	IGBT_3	IGBT_4	D_1	D_2	D_3	D_4
Average current	I_{avg}	A	16.00	0.40	0.40	16.00	6.00	10.50	10.50	6.00
Forward on-state voltage	V_{forw}	V	1.00	0.80	0.80	1.00	1.50	1.75	1.75	1.50
Conduction losses	P_{cond}	W	16.00	0.32	0.32	16.00	9.00	18.38	18.38	9.00
Switching and R.R. energy dissip.	E_{sw}/E_{RR}	J	0.17	0.10	0.10	0.17	0.08	0.10	0.10	0.08
Switching and R.R. power loss	P_{sw}/P_{RR}	W	8.28	5.08	5.08	8.28	2.68	3.57	3.57	2.68
Total power dissipated	P_{tot}	W	24.28	5.40	5.40	24.28	11.68	21.95	21.95	11.68

Table 7.1 Calculations of power losses in a submodule.

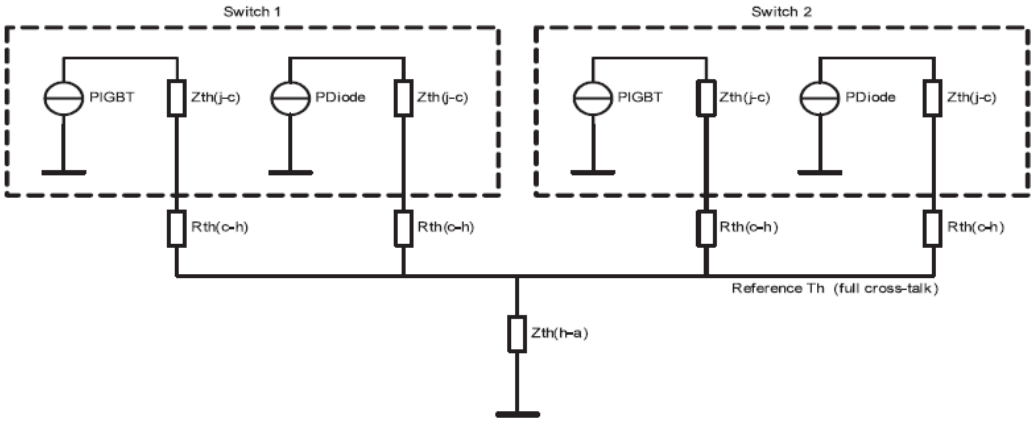

Fig. 7.7 IGBT module thermal model.

Then, to evaluate the junction overtemperatures, the thermal model of the IGBT module has to be considered, and it is reported for clarity in Fig. 7.7.

It can be seen from Fig. 7.7 that the heat sink (in the figure indicated with 'Reference Th') dissipates the overall thermal power produced by the IGBT module, to the external dissipator. The overtemperature of the heat sink with respect to the external dissipator is:

$$\Delta T = R_{th,h-a} * P_{tot_{module}} \tag{7.6}$$

Where $R_{th,h-a}$ [K/W] is the thermal resistance between heat sink and external dissipator and P_{tot_module} is the thermal power produced by a single IGBT module, i.e. the power dissipated from switch 1 (IGBT_1 and

D_1) and switch 2 (IGBT_2 and D_2). Note that the same amount of power is dissipated also by the other IGBT module of the submodule (see Table 7.1), thus the junction overtemperature will be calculated for only one of the two. Since the current in the semiconductor devices is low, natural convection has been considered as the only heat removal system, and thus an adequate heat sink must be chosen. It has been assumed $R_{th,h-a}$=1 [K/W] for an aluminium extrusion heat sink of 190×70×30 mm [33] which has about the same dimension of the IGBT module. The heatsink overtemperature is therefore:

$$\Delta T = R_{th,h-a} * \sum P_{tot_i} = 1 * 63.3 = 63.3\ °C \tag{7.7}$$

Now the junction overtemperature with respect to heat sink can be calculated as follows:

$$\Delta T_i = \left(R_{th,j-c} + R_{th,c-h}\right) * P_{tot_i} \tag{7.8}$$

Where $R_{th,j-c}$ and $R_{th,c-h}$ are respectively the thermal resistance [K/W] of junction to case and case to heatsink (reported in Table 6.1) and P_{tot_i} the total power dissipated by the device (last row of Table 7.1). Considering external air at a temperature of 40°C and adding the result of Eq.7.7 to each of the term resulting from Eq.7.8 the following junction overtemperature are obtained:

Symbol	unit	IGBT_1	IGBT_2	D_1	D_2
ΔT_{tot}	°C	65.97	63.90	65.85	68.09
T_{junc}	°C	105.97	103.90	105.85	108.09

Table 7.2 Overtemperatures with respect to external air at 40°C and junction temperatures of the IGBT module devices.

Considering a margin on the maximum junction overtemperature of 10%, i.e. 112.5 °C, natural convection could be a feasible heat removal source for this kind of application since all the estimated junction temperature reported in Table 7.2 are below 112.5 °C. This would result in a great simplification with respect to the actual design, where the cooling water is raised at the potential of the electric equipment.

Note that these results are strongly affected by the switching frequency of the submodules; for example, with a switching frequency of each SM equal to 100 Hz natural convection is not sufficient to provide the adequate cooling.

7.3.3 Capacitor Voltage Ripple

The choice of the submodule capacitance affects the capacitor voltage fluctuations, which must be limited to a certain extent, otherwise the oscillation on the DC voltage become excessive. In Fig. 7.8 the capacitor voltage waveforms are reported, where each of the three figures corresponds to a phase leg (denoted in the figure with A, B or C). The capacitor voltages pertaining to the upper arm are shifted of half fundamental period with respect to those of the lower arm, indeed the two arms work at the same way, only shifted of π electrical radians, resulting in a reduced ripple on the DC voltage. It can be further noted that the capacitor voltages are composed of a fundamental and a second order harmonic component, confirming the theoretical analysis given in Section 5.4. Finally, the peak to peak capacitor voltage ripple is a bit over 10% of the rated value, but however acceptable.

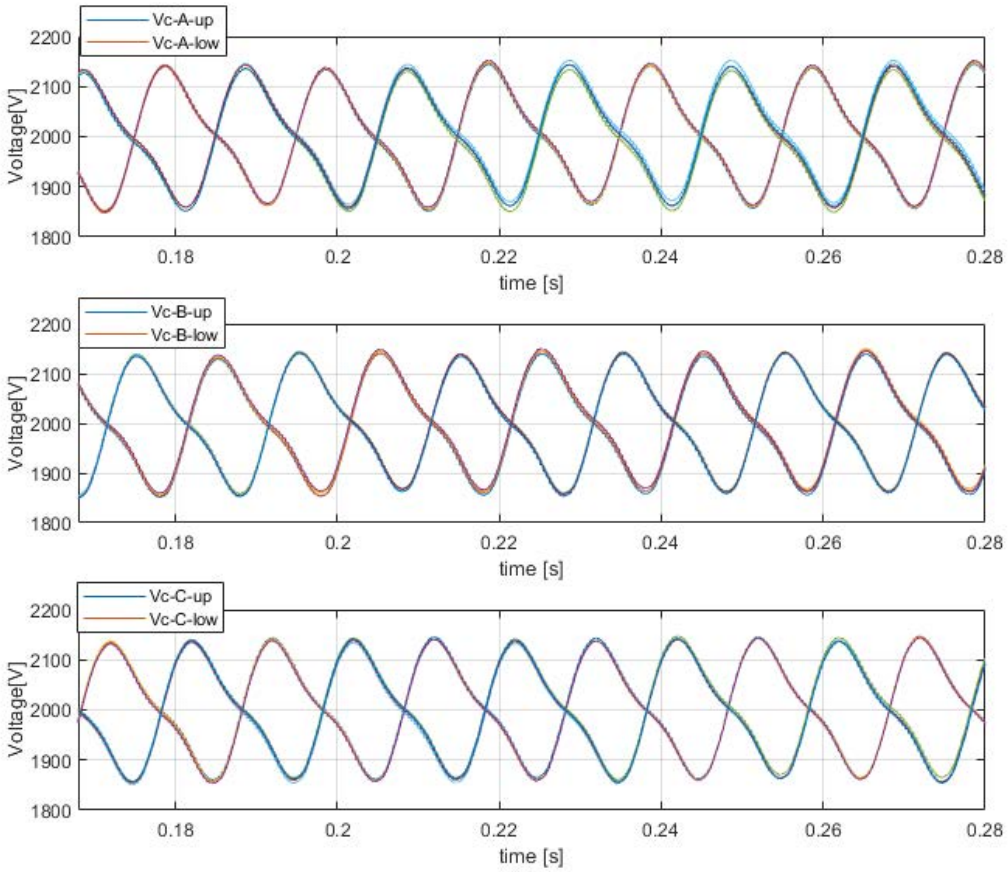

Fig. 7.8 Capacitor Voltages Ripple at steady state conditions and at the rated operational point.

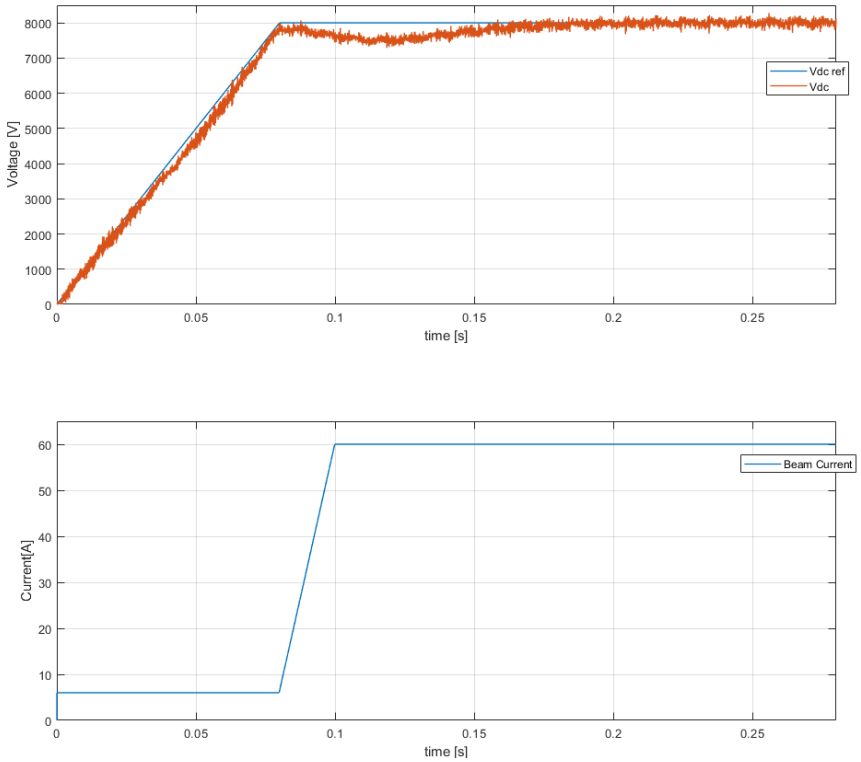

Fig. 7.9 Voltage ramp-up in 80 ms and then current ramp-up in 20 ms.

7.4 Verification of Dynamic performances

7.4.1 Voltage ramp-up without beam current

This scenario foresees a voltage ramp-up from zero to the nominal value, with the dynamic requirements reported in Table 4.2, and then a current ramp-up to the 100% of the optimum required for perveance matching. The current ramp-up starts from the 10% of the nominal value and reaches the 100% of the optimum value (i.e. 60 A) in 20 ms; this time has been chosen in order to limit the non-perveance time and restart quickly without however induce excessive oscillations in the DC voltage [18]. It can be seen from Fig. 7.9 that the current ramp-up starts at about 80 ms, i.e. when the voltage ramp-up reaches the nominal value (8 kV), as requested. The voltage at 80 ms reaches about 7.9 kV which is well over the 90% requested at the end of the voltage-ramp-up (see Table 4.2) and then the fluctuations are well below the 2.5% as requested.

The submodule capacitance value has been selected in Section 6.5 to limit the voltage undershoot at beam-on below the 10% of the rated value (i.e. 800 V for 8 kV of rated value); as can be seen in Fig. 7.9 the calculations are confirmed by the simulations and the submodule capacitance is adequate to contain the undershoot.

7.4.2 Start-up in perveance matching

This scenario foresees a voltage ramp-up in 80 ms and, at the same time, a current-ramp up in perveance matching conditions, i.e. the current is varied in agreement with Eq. 3.1. The result of the simulation has been reported in Fig.7.10: at t=300 ms the start-up sequence is initialized and at t=80 ms the DC voltage reaches about 7500 V and thus the rise time of 80 ms to the 90% of the full voltage is satisfied.

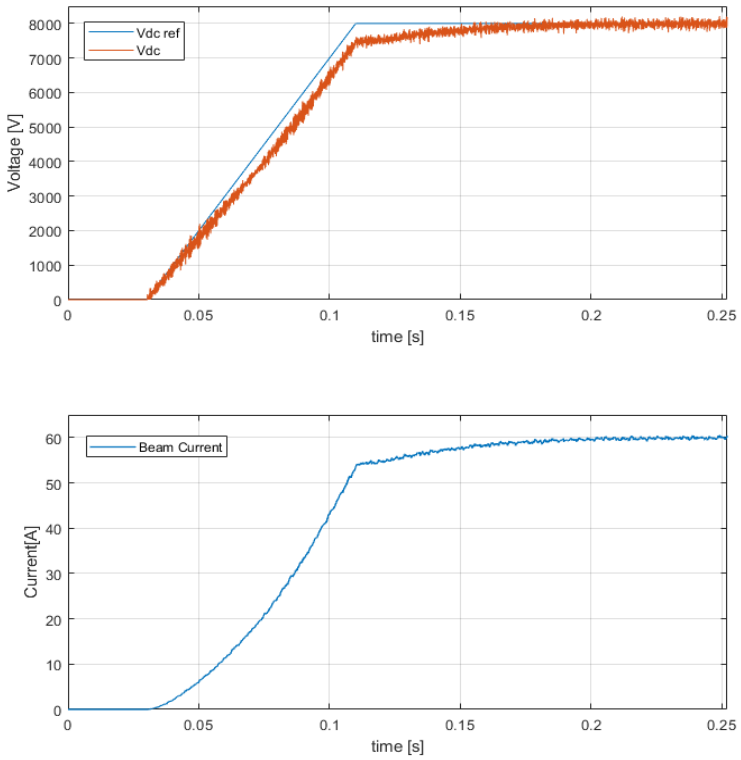

Fig. 7.10 Start-up in perveance-matching conditions.

7.4.3 Beam-off simulation

A beam-off is a sudden and abrupt interruption of the beam current and correspond to a loss of load for the AGPS. It is expected an overvoltage of the DC voltage mainly due to the energy stored in the inductive elements upstream of the load. The beam-off event shall be properly detected and then the AGPS shall switch off, in order to limit the overvoltage on the DC bus, which could be disruptive for the electrical equipment. In the model the protection is triggered (i.e. the status of the variable "BD_protection" becomes 0, see Fig. 7.1) when the DC voltage exceeds the 10% of the rated value; as discussed in Section 6.6 it has been assumed a total delay of 7.3us from when the threshold is exceeded and the switching off. In order to limit the overvoltage at beam-off below the 15% of the rated voltage (i.e. 1.2 kV for 8 kV rated) a proper capacitance value for the DC filter has to be selected.

The capacitance value has been tentatively found by simulations and results in:

$$C_f = 945\ nF \tag{7.9}$$

Which corresponds to an overvoltage of about 9 kV, as can be seen in Fig. 7.11, and accounts for some margin because of additional stray inductances not considered in the numerical model.

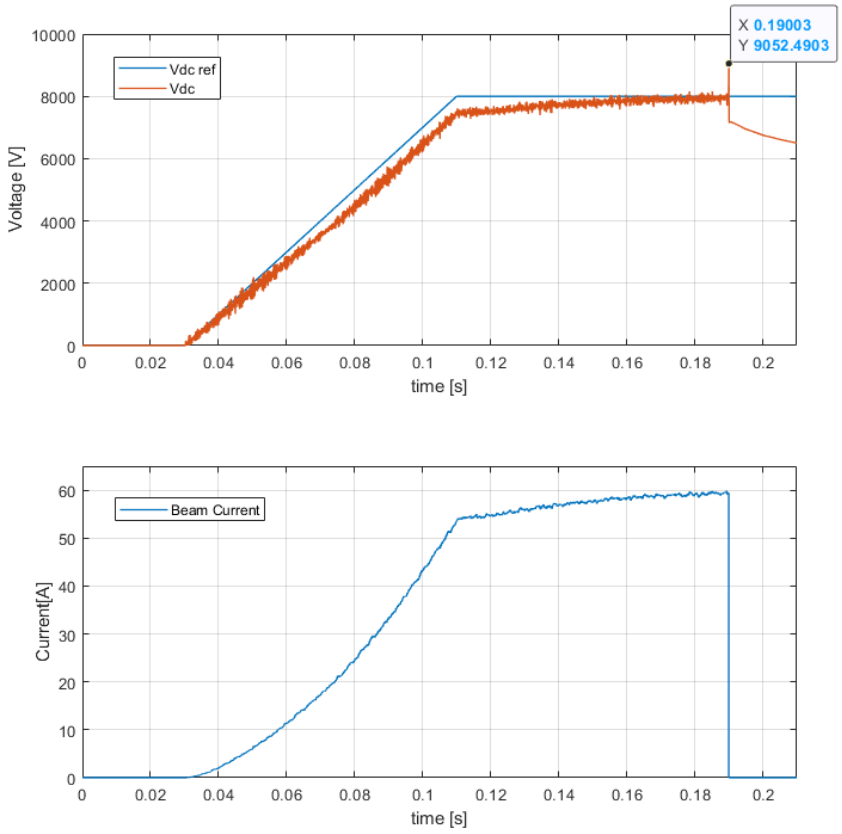

Fig. 7.11 Beam off simulation: at t=190 ms the beam current interrupts and a consequent overvoltage appear on the DC link.

7.4.4 Breakdown (BD) simulation

The grid breakdowns (BDs) are equivalent to short-circuits as seen from the AGPS and rather than exceptional events are expected to occur rather frequently. The AGPS shall be able to switch off the current within 100 μs and be able to restart in 20 ms. In the model the protection is based on the DC current measurement: when the current exceeds the rated value by 15% (i.e. >69 A) and after the considered delay time (7.3 us) all the gate signals becomes zero and thus the IGBTs open and the current extinguishes. The value of the DC filter resistor has been selected in order to limit the overcurrent from the DC filter to the grids in case of BD. The estimation of the resistance value can be made from the estimation of the AGPS peak current.

First, the current derivative at BD can be estimated in the following way:

$$\frac{di}{dt} = \frac{3\,V_{DC}}{2L_{\,arm}} = \frac{3 * 8\,kV}{2 * 3mH} = 4\left[\frac{A}{\mu s}\right] \tag{7.10}$$

Thus, the AGPS peak current is about:

$$I'_{pk} \cong I_{nom} + \frac{di}{dt} * t_{delay} = 60 + 4 * 7.3 = 89.2\,A \tag{7.11}$$

Then, considering a maximum admissible peak current on the grids in the event of BD of 3 kA [6] the necessary resistor of the output filter can be estimated as:

$$R_f = \frac{V_{DC}}{I_{pk,max} - I'_{pk}} = \frac{8000}{3000 - 89.2} \cong 2.74\,\Omega \tag{7.12}$$

This value of resistor has been adopted for the simulations.

The voltage and current at grid BD and the following restart of the system are reported in Fig. 7.12.

It can be seen that after a grid BD the voltage ramp-up restarts in 20 ms as required by the dynamic specifications listed in Table 4.3. The dynamic requirements of Table 4.2 are still satisfied.

From the simulation it results a peak current from AGPS of about 89 A, confirming the estimation made with Eq. 7.11., and an overcurrent from the DC filter of about 2.5 kA.

It is of interest to evaluate the total charge transferred to the arc during the BD event. The DC filter contribution can be estimated as:

$$Q_1 = C_f * V_{DC} = 945\,nF * 8kV = 7.56\,mC \tag{7.13}$$

Whereas the AGPS contribution can be estimated considering that after having reached the peak the current decreases with the same slope of Eq. 7.10 but with negative sign and thus it is nullified after the time:

$$t' = \frac{I'_{pk}}{\frac{di}{dt}} = 22.3\,\mu s \tag{7.14}$$

Finally, the AGPS contribution can be estimated as:

$$Q_2 = \frac{I_{DC,nom} + I'_{pk}}{2} * t_{delay} + \frac{I'_{pk}}{2} * t' = 1.5\,mC \tag{7.15}$$

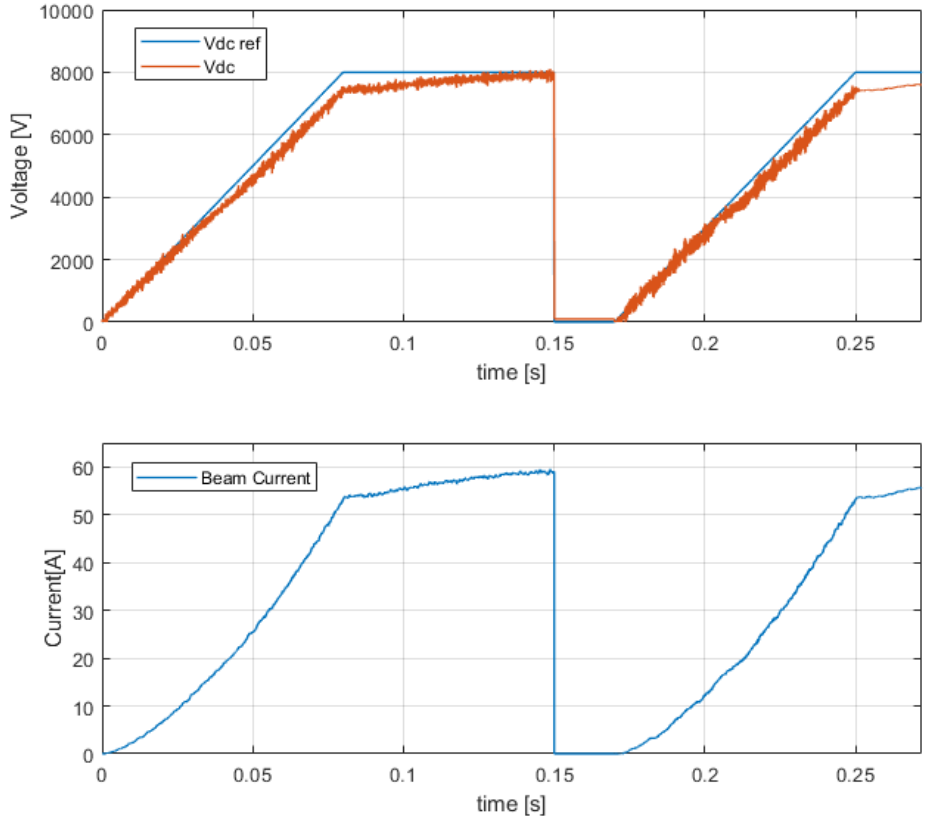

Fig. 7.12 Breakdown event at t=150 ms and following restart of the system.

7.5 Comparison between Model and full-scale MMC AGPS system

The DC filter designed for the 8 kV MMC through simulations must be scaled to the full voltage of 200 kV. The capacitor filter must limit the overvoltage of a system which can be considered made by the series of 25 stages of 8 kV. For each stage of 8 kV the adequate capacitance value, as demonstrated by simulations, is C=945 nF. Therefore, the total capacitor filter value at 200 kV is:

$$C_{f,200kV} = \frac{C_f}{25} = 37.8\ nF \tag{7.16}$$

Note that the total charge transferred by the DC filter to the arc at 200 kV remains the same of that calculated by Eq.7.13. (i.e. $Q_1'=Q_1$).

The AGPS contribution to the arc shall be rescaled for the full voltage of 200 kV. The current derivative at BD is given by Eq. 7.10 with V_{DC}=200 kV, resulting in:

$$\frac{di}{dt} \cong 100\frac{A}{\mu s} \tag{7.17}$$

And the estimated peak current, calculated with Eq. 7.11, results of:

$$I'_{pk,200\ kV} = I_{DC,nom} + \frac{di}{dt} * t_{delay} = 60 + 100 * 7.31 = 791\ A \tag{7.18}$$

Considering that after the peak the current from the AGPS system decays with the same slope but opposite sign, the current is nullified after:

$$t'' = \frac{I''_{pk}}{\frac{di}{dt}} = 7.91\mu s \tag{7.19}$$

And finally the charge contribution to the arc in the event of breakdown from the 200 kV MMC system is estimated by Eq.7.15 resulting in:

$$Q'_2 \cong 6.2\, mC \tag{7.20}$$

The estimation of the total charge transferred to the arc from the High Voltage DC filter and the MMC AGPS is thus:

$$Q_{tot}^{200kV} = Q'_1 + Q'_2 = 7.56 + 6.52 \cong 13.8\, mC \tag{7.21}$$

This rough estimation indicates that with an AGPS system based on MMC the total charge transferred to the arc in the event of BD is significantly lower than that of the actual design. Indeed, estimations made in [6] shows that, in the ITER and MITICA AGPS, the contribution from the HV DC filter is about 60 mC and the contribution from AGPS-CS of about 34.2 mC. The found result is not surprising since the MMC system, based on IGBT submodules, is quicker with respect to the actual design based on NPC inverters with IGCTs. This implies:

- a smaller capacitance filter to limit the overvoltage in the event of beam-off, i.e. 37.8 nF rather than 300 nF [6] and thus a smaller charge (energy) transferred to the grids in case of BD;
- a smaller contribution of the AGPS in the arc energy.

Having reduced both the contributions is obviously beneficial, since the arc energy is much reduced and thus the possible damage to the grids.

8 Conclusions

The Acceleration Grid Power Supply (AGPS) of the Neutral Beam Injectors (NBs) foreseen for the largest thermonuclear fusion reactors have been studied, with particular focus on the AGPS of MITICA, which is the full-scale prototype of the ITER NBI. The current design consists in two stages: the AGPS Conversion System (CS) and the AGPS Direct Current Generator (DCG). The AGPS CS comprises a rectification stage of the AC voltage grid and then an inversion stage operated by NPC inverters with a common DC link. The AGPS DCG comprises step-up transformers that raise the voltage at the required level and then the voltage is finally rectified by High Voltage (HV) diode rectifiers. The double conversion stage consists in higher power losses with respect to solutions with only one rectification stage and the DC output voltage is feedback regulated by means of the inverters modulation index, resulting in reduced controllability of the output voltage. Moreover, the HV filters placed downstream the diode rectifiers discharge a significant amount of energy into the grids in the event of Breakdown (BD), with possible damage of them. These critical points call for the evaluation of alternative solutions comprising advanced converter topologies.

The Modular Multilevel Converter technology has been selected as a possible candidate to the particular requirements of the NBI AGPS, thanks to its intrinsic modularity, efficiency and scalability in terms of voltage and power rating. The MMC topology has been deeply investigated, considering the various submodule configurations (i.e. Full and Half Bridge Submodule), the basic function, the control and modulation techniques and the DC side short-circuit management. The acquired knowledge has been used as a basis for a preliminary design of an AGPS system based on MMC topology.

The main circuit parameters of a 200 kV DC rated MMC, intended for AGPS application, have been determined by a preliminary design. Firstly, the Full-Bridge (FB) MMC topology has been selected because of its capability of interrupting DC short-circuits in short time and without the tripping of AC or DC circuit breakers. Then the main circuit parameters have been chosen, taking into account normal and anomalous operative conditions.

It has been developed a numerical model in Matlab-Simulink of an 8 kV DC rated FB-MMC in order to verify the compatibility of the topology with the specific requirements of the AGPS application. Several simulations have been performed, both in normal and anomalous condition (breakdown and beam off) and the steady state and dynamics requirements have been satisfied with margin. A thermal analysis of the power semiconductors has also been carried out, showing the possibility of natural convection as the heat-removal source, with great simplification with respect to the actual cooling system. Moreover, the model has been used to design the DC filter of the full-scale MMC 200 kV rated; calculations made on the total charge transferred by the capacitor filter to the grids in the event of breakdown show a great reduction with respect to the actual design. This is obviously beneficial since the arc energy is reduced, and the possible damage of the grids too.

All the analysis made show that the Modular Multilevel Converter topology can represent a promising configuration for the AGPS of future NBI. Further studies shall be made in order to evaluate the impact on the occupancy area of the MMC solution, which is air-insulated. At this regard the main circuit parameters determined in the preliminary design may serve as a starting point for the estimation of the required space. The cost-effectiveness of the solution should also be evaluated and compared to the actual configuration. At this regard other submodule topologies may be investigated aiming at the minimization of the semiconductor chip area and the power losses. Indeed, the additional switching states provided by the FB topology are not very useful in normal operation, because a reverse DC voltage is not required for AGPS application (and for HVDC application too). Thus, doubling the number of semiconductors and the semiconductor losses in normal operation represent a severe drawback with respect to the HB topology. For a MMC intended for AGPS application, however, the short-circuit cut-off capability is indispensable and possible alternative topologies must include this functionality.

9 Appendix

In this section are reported some graphs regarding variables of the converter control loops or other interesting waveforms.

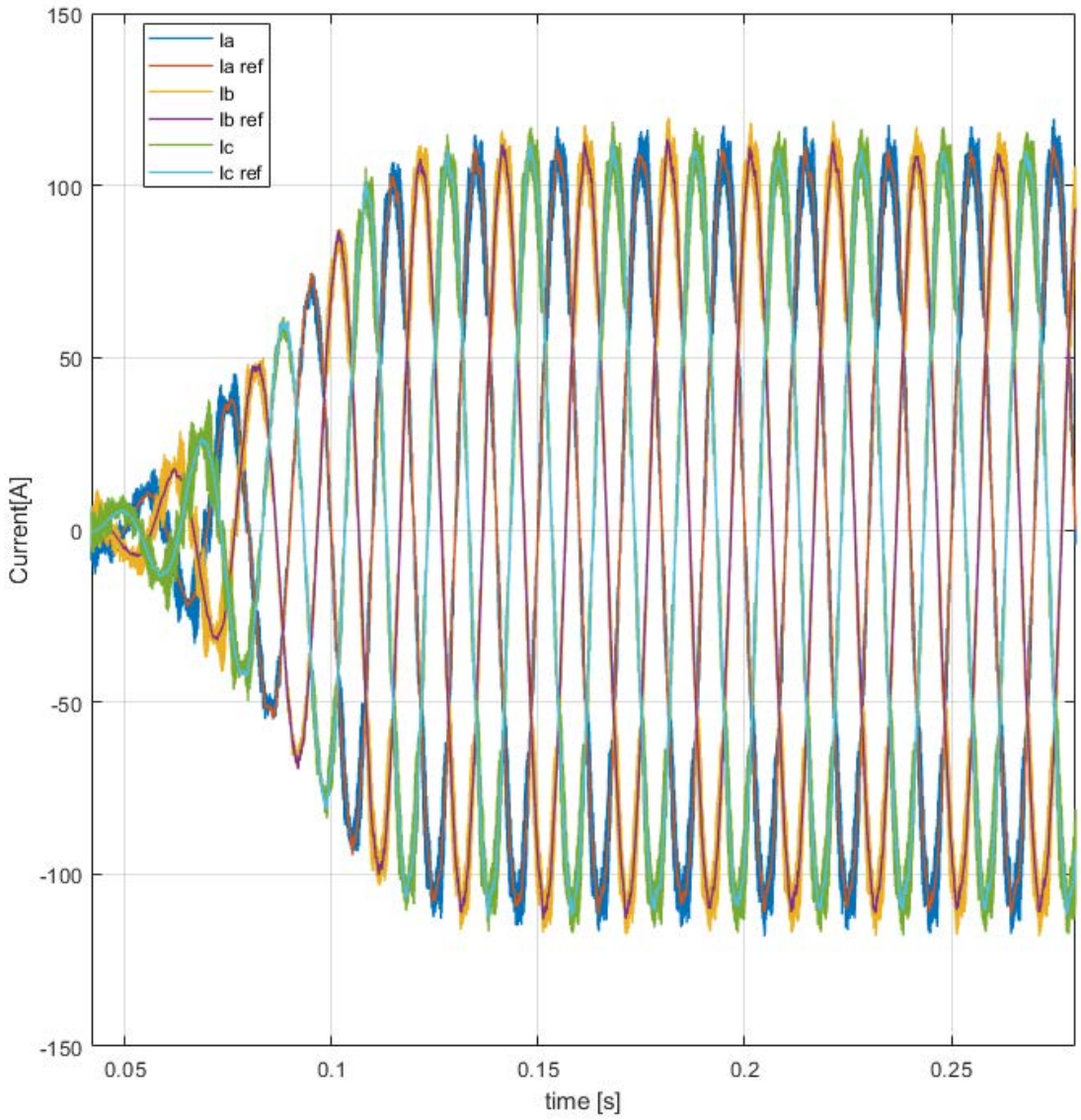

Fig. 9.1 Currents measurements and their references. It can be seen a perfect tracking of the references.

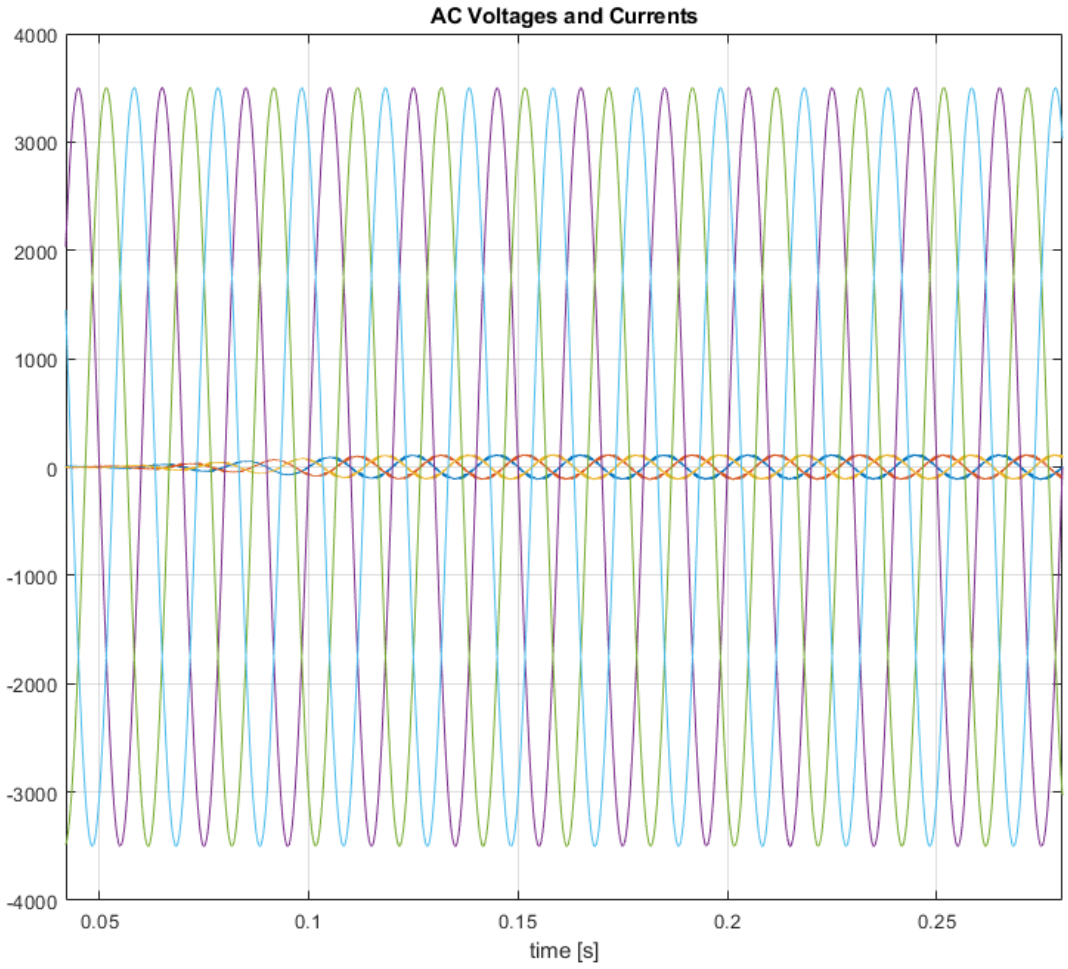

Fig. 9.2 AC grid voltages and AC currents. The waveforms are in phase, i.e. cos(φ)=1. The quadrature current reference is set to zero and thus only active power is exchanged between the grid and the MMC.

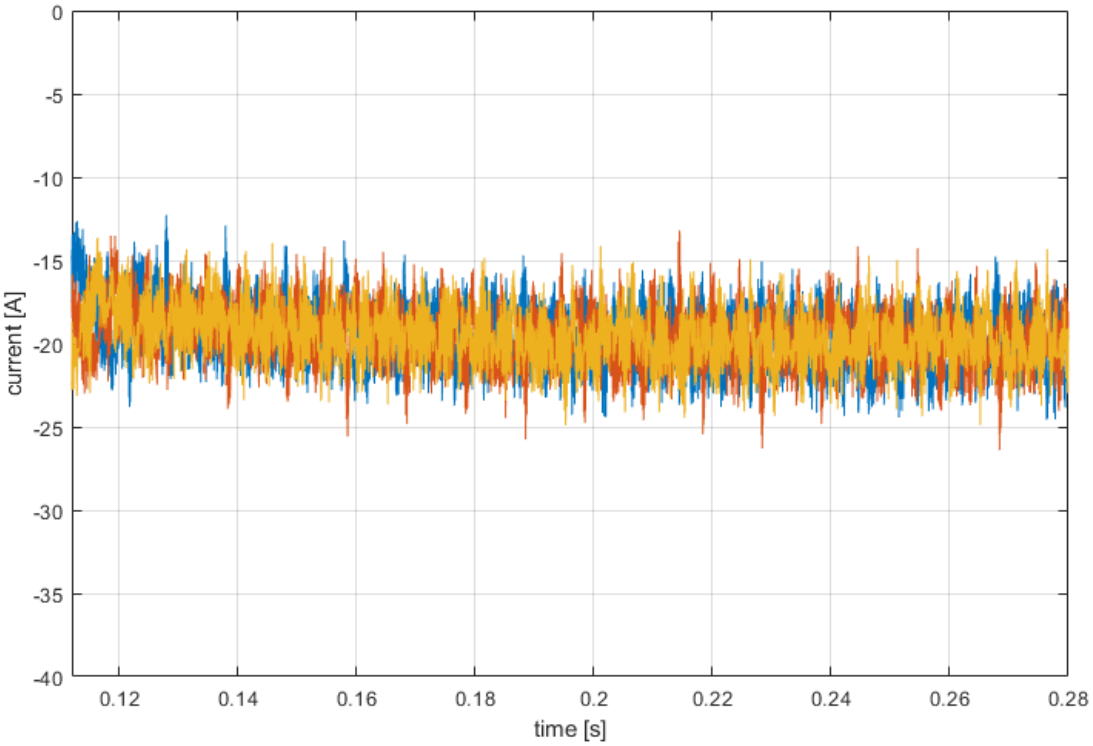

Fig. 9.3 Circulating currents with Circulating Current Control enabled. As can be seen the currents are maintained to a near constant value, i.e. Idc/3=20 A.

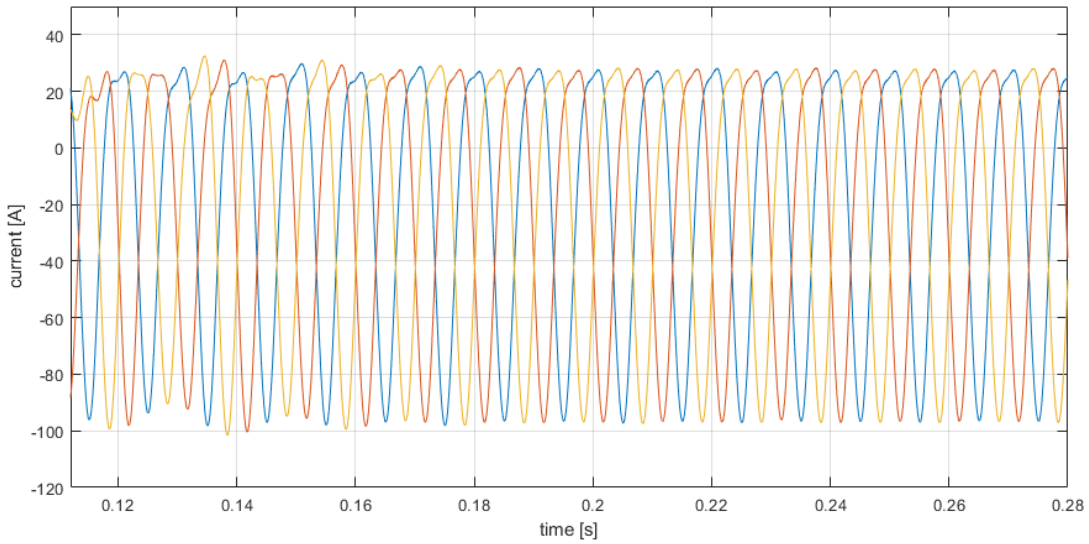

Fig. 9.4 Circulating currents with Circulating Current Control disabled. As can be seen undesirable large fluctuations of twice the fundamental frequency appear in the circulating currents.

10 References

[1] International Energy Oulook, 2017.

[2] C. Bustreo e a. et, «Economic assessment of different operational reactor cycle structures in a pulsed DEMO-like power plant,» *Fusion Engineering and Design,* vol. 124, pp. 1219-1222, 2017.

[3] J. Wesson, Tokamaks, Clarendon Press-Oxford, 2004.

[4] «https://www.iter.org/».

[5] J. How, «ITER Plant Integration Documentation, ITER_D_2234RH,» 2007.

[6] A. Ferro, «Study of the Power Supply System for the acceleration grids of the ITER Neutral Beam Injector,» Doctoral thesis, 2011.

[7] «EUROfusion,» [Online].

[8] T. Franke e a. et, «Heating & current drive efficiencies, TBR and RAMI considerations for DEMO,» vol. 123, pp. 495-499, 2017.

[9] J. Pamela e e. al., «Efficiency and availability driven R&D issues for DEMO,» *Fusion Engineering and science,* vol. 84, pp. 194-204, 2009.

[10] Hemsworth and Inoue, "Positive and Negative Ion Sources for Magnetic Fusion," *IEEE TRANSACTIONS ON PLASMA SCIENCE,* vol. 33, no. 6, pp. 1799-1813, 2005.

[11] R. Hemsworth and al., *New J. Phys.,* vol. 19, no. 025005, 2017.

[12] V. Antoni, Consorzio RFX, «The ITER Neutral Beam system: status of the project and review of the main technological issues,» Padova, IT.

[13] N. P. e. al., «Magnetic Field Effect on Voltage Holding in the MITICA Electrostatic Accelerator,» *IEEE TRANSACTIONS ON PLASMA SCIENCE,* vol. 42, n. 4, 2014.

[14] V. Toigo e al., «The PRIMA Test Facility: SPIDER and MITICA test-beds for ITER neutral beam injectors,» *New Journal of Physichs,* vol. 19, n. 085004, 2017.

[15] P. Agostinetti and al., "Report on NB Injector and System Concept," Final Report on Eurofusion Deliverable HCD-3.1-T003-D001, 8 Febbraio 2019.

[16] P. Sonato e a. et, «Conceptual design of the beam source for the DEMO Neutral Beam Injectors,» *New Journal of Physics,* vol. 18, n. 125002, 2016.

[17] E. Gaio and al., "The alternative design concept for the ion source power power supply of the ITER neutral beam injector," *Fusion Engineering and Design,* vol. 83, pp. 21-29, 2008.

[18] «F4E-RFX-PMS_A-WP-2013 Agreement on the Neutral Beam Test Facility Project-Work Programme 2013».

[19] L. Zanotto, «Assessment of performance of the acceleration grid power supply of the ITER Neutal Beam Injector,» *Fusion Science an Design,* vol. 84, pp. 2037-2041, 2009.

[20] T. Meynard and al., "Multi-level conversion: High voltage choppers and voltage-source inverters".

[21] R. Marquardt, «Modulares Stromrichterkonzept für Netzkupplungsanwendung bei hohen Spannungen,» *Proceedings of the ETG-Fachtagung, Bad Nauheim, Germany,* 2002.

[22] L. Lesnicar e R. Marquardt, «An innovative Modular Multilevel Converter Topology Suitable for a Wide power range,» in *IEEE Bologna PowerTech Conference*, Bologna, Italy, 2003.

[23] K. Ilves, «On Energy Storage Requirements in Modular Multilevel Converters,» *IEEE Trans Power Electronics,* vol. 29, n. 1, pp. 77-78, 2014.

[24] R. Marquardt, «Modular Multilevel Converter: An universal concept for HVDC-Networks and extended DC-Nus Applications,» in *The 2010 International Power Electronics Conference*.

[25] L. Harnefors and al., "Dynamics Analysis of Modular Multilevel Converter," *IEEE TRANSACTIONS ON INDUSTRIAL ELECTRONICS,* vol. 60, no. 7, pp. 2526-2537, 2013.

[26] «https://it.mathworks.com/products/matlab.html».

[27] A. Antonopoulos, «On dynamics and voltage control of the modular multilevel converter,» in *Proceedings of the 13th European Conference on Power Electronics and Applications*, 2009.

[28] K. Ilves and al., "Steady-State Analysis of Interaction Between Harmonic component of Arm and Line Quantities," *IEEE TRANSACTIONS ON POWER ELECTRONICS,* vol. 27, no. 1, pp. 57-68, 2012.

[29] K. Ilves and al., "Analysis and operation of modular multilevel converters with phase-shifted carrier PWM," *IEEE Transactions on Power Electronics,* vol. 30, no. 1, p. 268–283, 2015.

[30] ABB Switzerland Ltd, Semiconductors, «ABB,» [Online]. Available: https://library.e.abb.com/public/638cd20fb11b4ca48fae1715daf39387/5SNG%200150P450300_5SYA%201593-05%2002-2018.pdf.

[31] P. Steimer and al., "IGCT devices application and future opportunities," *Proceeding of the IEEE Power Engineering Society Summer Meeting,* vol. 2, pp. 1223-1228, 2000.

[32] "https://it.mathworks.com/products/simulink.html," [Online].

[33] MingfaTech, «https://www.mingfatech.com/tled-190-70-30-190-70-50-large-led-aluminum-extrusion-heat-sink,» [Online].

[34] «DEMO1 Reference Design,» marzo 2017.

[35] A. Nabae, «A new neutral-point-clamped PWM inverter,» *IEEE Transactions on Industry Applications,* Vol. %1 di %2IA-17, n. 5, pp. 518-523, 1981.

[36] K. Sharifabadi and al., "Wiley," 2016. [Online]. Available: https://www.wiley.com//legacy/wileychi/sharifabadi/overview.html?type=SupplementaryMaterial.